

THESIS

DEVELOPMENT OF A FINITE ELEMENT MODEL OF SUPRACONDYLAR FRACTURES
STABILIZED WITH VARIABLE STIFFNESS BONE PLATES

Submitted by

Conor J. Sutherland

Department of Mechanical Engineering

In partial fulfillment of requirements

For the Degree of Masters of Science

Colorado State University

Fort Collins, Colorado

Fall 2019

Master's Committee:

Advisor: Christian M. Puttlitz

Co-Advisor: Kirk C. McGillvray

Jeremiah Easley

Susan James

Copyright by Conor J. Sutherland 2019

All Rights Reserved

ABSTRACT

DEVELOPMENT OF A FINITE ELEMENT MODEL OF SUPRACONDYLAR FRACTURES STABILIZED WITH VARIABLE STIFFNESS BONE PLATES

Approximately 10% of orthopaedic fracture fixation cases lead to non-union, requiring surgical intervention. Inadequate fixation device stiffness, which causes unwanted fracture gap motion, is believed to be one of the largest factor in poor healing as it prevents ideal tissue proliferation in the callus. By altering the thickness of orthopaedic bone plates, it was theorized that the fracture gap micro-mechanics could be controlled and driven towards conditions that accommodate good healing. The first goal of the project was to create computational FEA models of an ovine femoral supracondylar fracture stabilized with a plate of varying thickness. The models were used to investigate the mechanical behavior of the plate and the callus under different physiological loading conditions. The second goal of this study was to validate the computational model with bench-top experiments using an *ex-vivo* ovine femoral fracture model. To achieve these goals, novel plates were designed and manufactured with different stiffnesses (100%, 85%, and 66% relative stiffness) to be used to treat a femoral supracondylar fracture model in ovine test subjects; both *in-vivo* and *ex-vivo*. The FE models were shown to accurately predict the stress/strain mechanics on both bone and plate surfaces. Micromechanics (strain and pressure) predictions in the fracture gap were reported and used to make tissue type proliferation predictions based on previously reported mechanics envelopes corresponding to bone remodeling. The results indicated that changing plate thickness successfully altered the construct stiffness and consequently, the predicted healing tissue type at the fracture site. The FE methods described could help improve

patient specific fracture care and reduce non-union rates clinically. However, further *in vivo* testing is required to validate the clinical significance of the methods described in this thesis.

Table of Contents

Abstract.....	ii
List of Figures.....	vii
1. Background.....	1
1.1 Supracondylar Fracture.....	1
1.2 Orthopaedic Hardware	3
1.3 Micromechanics of Fracture Gap.....	6
1.4 Hardware Strains and Fracture Non-unions.....	9
1.5 Finite Element Analysis.....	11
1.6 Problem Statement	12
2. Specific Aims.....	13
2.1 Objective.....	13
2.2 Specific Aim 1	13
2.3 Specific Aim 2	13
3. Model Creation and Validation Materials and Methods.....	14
3.1 Sheep as a Translational Animal.....	14
3.2 Supracondylar Fracture Model Design	14
3.3 Plate Design	16
3.4 Finite Element Model Generation.....	22
3.4.1 Femur Model Development	22
3.4.2 Material Properties.....	24
3.4.3 Femur Model Boundary Conditions	25

3.4.4	Plate Model Development.....	26
3.4.4.1	Plate Mesh Convergence Study	27
3.4.5	Plated Femur Model Assembly.....	28
3.4.6	Femur Model Boundary Conditions	29
3.4.7	Fracture Healing Modeling	30
3.5	FEM Principal Strain Vector Investigation.....	31
3.6	Specimen Acquisition and Preparation	33
3.7	Model Validation	35
3.7.1	Bone Surface Strain Validation	35
3.7.1.1	Experimental Setup for Strain Gage Testing on Bone.....	36
3.7.1.2	Bone Surface Strain Gage Experimental Protocol.....	37
3.7.2	Plated Study Validation	38
3.7.2.1	Plated Study Experimental Setup.....	38
3.7.2.2	Bench-Top Fracture Simulation.....	40
3.7.2.3	Plated Study Loading Protocol	42
4.	Model Predicted Callus Micro-Mechanics.....	43
5.	Results.....	45
5.1	Mesh Convergence on Plate Models.....	45
5.2	Strain Vector Analyses - Cylindrical Model and Single Element	47
5.3	FE Model Validation.....	49
5.3.1	Bone Surface Strain Validation	49
5.3.2	Plate Strain Study Model Predictions Over a Simulated Healing Cascade	51
5.3.3	Bench-Top Plated Femoral Fracture Models' Strain Measurements.....	55

5.3.1	Axial Strain Measurements vs Strain Model Predictions for the Plated Femoral	
	Construct	59
5.4	Fracture Region Micro-Mechanics Predictions	63
6.	Discussion	73
7.	Conclusions	84
	References	86

LIST OF FIGURES

Figure 1: A) An Illustration Of A Human Femur. B) A Radiograph Of A Supracondylar Fracture In A Human Femur.2

Figure 2: A) Grasa Et Al. Reported Axial Loads (Kg) Through The External Fixator In One Sheep Vs Days Post Osteotomy B) Stoffel Et Al. Reported Plate Surface Strain Under Bending For Different Gait Speeds In An Ovine Tibial Osteotomy Model 10

Figure 3: A) Ovine Skelton Illustration Showing Where The Femoral Bone Is Located. B) Transected Femur With An End View Of The Sectioned Distal Epiphysis. C) An Enlarged Image Of The Cross Section Of The Ovine Supracondylar Region..... 15

Figure 4 : (A) A Radiograph Image Of A Human Supracondylar Fracture Of The Femur (B) An Image Of A Vibrating Saw Being Used To Transect The Femur (C) An Image Of An Isolated, Skeletonized Ovine Femur With The Transected Ovine Femur Model 16

Figure 5: A Locking Compression Plate (Lcp) Used For Distal Femurs 16

Figure 6: Rendered 3d Ovine Femur Surface Models Of Cortical And Cancellous Bone 17

Figure 7: Creating The Lofted Spline Plate Model That Was Designed To Conform To The 3d Ovine Femur Model Geometry..... 18

Figure 8: Six Generations Of Plate Design Prototypes..... 19

Figure 9: The Finished Plate Design Front View And Side View Of The Thick Plate 20

Figure 10: The Manufactured Plates..... 22

Figure 11: Steps Taken To Generate An Ovine Femoral Model For Finite Element Analysis..... 23

Figure 12: Anatomy Of The Cross Section Of The Proximal Half Of A Femur..... 24

Figure 13: Image Of The Femoral Fea Model And Its Boundary Conditions..... 26

Figure 14: The BCs Of The Plate Models Utilized For Mesh Convergence.....	28
Figure 15: An Image Of The Plate Bone Fe Model With The Thickest (4.8 MM) Plate, Colored by Material.....	29
Figure 16: FE Model Showing Elements Selected For The Osteotomy.....	31
Figure 17: A Cylinder Fea Model With Ovine Cortial Bone Properties, Simulated Under A 700 N Point Load.....	32
Figure 18: A Single Element Was Emperically Analysed For Strain Vectors.....	32
Figure 19: Femur Potted At The Proximal End, Prior To Plate Attachment.....	33
Figure 20: (A) Digital Image Of An Ovine Femur Fixed Into The Mts Machine Using A Custom Made Fixture (B) Two Views Of The Femur In The Fixture Illustarting Whre The Indenter Is Aligned.....	34
Figure 21: The Femoral Model And The 4 Regions Where Strain Data Were Probed.....	35
Figure 22: Left: Strain Gages Attached To The Surface Of A Prepare Femur Specimen. Right: A Strain Gage Test Specimen Put Into Compression In The Mts.....	36
Figure 23: An Example Figure Of The Extrapolation Method Used For The Plate Strain Gage Measurements.....	37
Figure 24: The Numbering Used For All Plate Strain Analysis And Predictions.....	38
Figure 25: (A) Side View Of A 3.2 Mm Thick Plate With 4 Strain Rosettes Attached. (B) Front View Of A 3.2 Mm Thick Plate With 4 Strain Rosettes Attached. (C) An Intact Ovine Right Femur Plated With A 4.6mm Thick Plate (D) A Radiograph Of The Plated Ovine Femur....	40
Figure 26: Model Healing Cascade Discrete Levels.....	41
Figure 27: Left: A Proximal View Of The Bone With The Callus Hightlighted. Right: The Regions Of The Callus Reported On.....	44

Figure 28: Thick Plate Mesh Convergence.....	45
Figure 29: Middle Plate Mesh Convergence.	46
Figure 30: Thin Plate Mesh Convergence	46
Figure 31: (A) A Cylinder Fea Model With Ovine Cortial Bone Properties Under A 700 N Point Load. (B) An Isolated Section Of The Tube (C) The Same Section With Principal Strain Vectors Graphically Represented	48
Figure 32: The Single Element In The Regions Of Interest Probed For Emperical Analyis.....	49
Figure 33: Strain Magnitudes Predicted By The Model And Found Experientally For The Four Regions Of Interest.	50
Figure 34: Thick (4.6 Mm) Plate Log-X Plot Of Strain Predictions Over An Increasing Callus Modulus	52
Figure 35: Middle (3.8 Mm) Plate Log-X Plot Of Strain Predictions Over An Increasing Callus Modulus	52
Figure 36: Thin (3.2 Mm) Plate Log-X Plot Of Strain Predictions Over An Increasing Callus Modulus	53
Figure 37: Average Strain Measurements (N=7) For The 4.6 Mm Thick Plate Over The Reverse Fracture Model.....	56
Figure 38: Average Strain Measurements (N=7) For The 3.8 Mm Thick Plate Over The Reverse Fracture Model.....	57
Figure 39: Average Strain Measurements (N=8) For The 3.2 Mm Thick Plate Over The Reverse Fracture Model.....	58
Figure 40: Thick Plate Measured Strains And Model Predictions For Intact And Fractured Cases For Each Gage Region	60

Figure 41: Middle Thickness Plate Measured Strains And Model Predictions For Intact And Fractured Cases For Each Gage Region.	60
Figure 42: Thin Plate Measured Strains And Model Predictions For Intact And Fractured Cases For Each Gage Region.	61
Figure 43: 1kPa - Fracture Micro-Mechanics.	66
Figure 44: 10kPa - Fracture Micro-Mechanics.	67
Figure 45: 100kPa - Fracture Micro-Mechanics.	68
Figure 46: An Illustration Of How Plate-Bone Construct Flexion Behaviour Was Expected Under Axial And Bending Dominated Scenarios.	81

1. Background

1.1 Supracondylar Fracture

Condyles are the protuberance in the distal region of both the humerus and femur bones in mammals (Figure 1a). Fractures just proximal to the condylar region, appropriately named supracondylar fractures (Figure 1b), are very common amongst children [1], [2] accounting for 60-75% of elbow fractures, and approximately 7% of all femoral fractures in adolescents [3]–[5]. These fractures generally occur in the developing bone of the growth plate (Figure 1a), a region of cartilage found in the long bones of pre-adolescents. This region contains proliferating chondrocytes that grow layers of bone, separating the secondary ossification center (regions with non-proliferating chondrocyte) and primary spongiosa (i.e., the precursor to trabecular bone), a process that leads to natural bone lengthening/growth [6]. Unfortunately, supracondylar fractures can result in serious nerve damage and impaired circulation [7]. Fractures in growth plates also cause significant disruption to normal bone growth. However, effective fixation can drastically reduce the significance of these disturbances [7]. Therefore, it is imperative to ensure correct fracture fixation methods are used when treating supracondylar fractures.

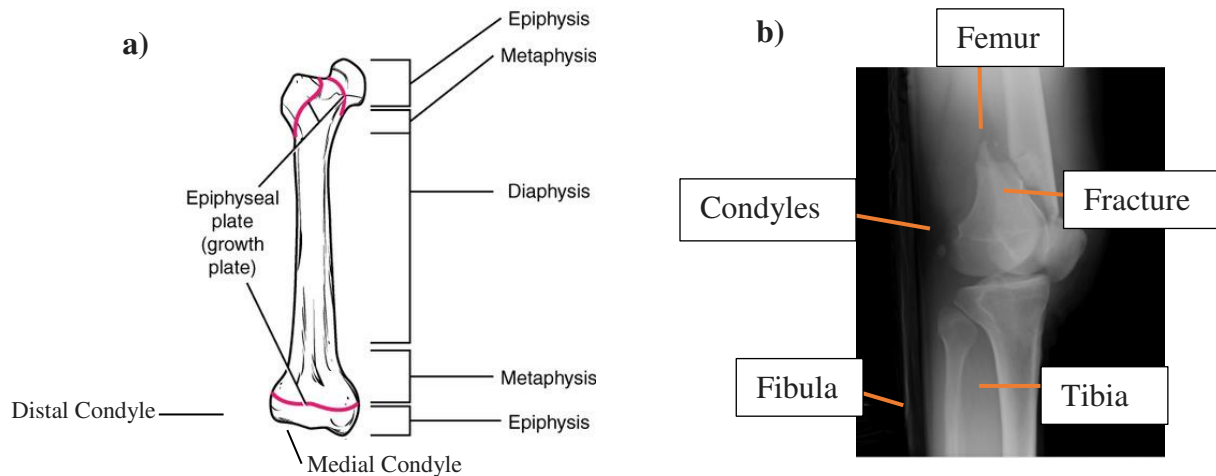


Figure 1: a) An illustration of a human femur indicating the growth plates and different regions of the bone. b) A radiograph of a supracondylar fracture in a human femur.

Long-bone fractures, such as those of the distal femur, are generally fixed with either an intramedullary (IM) nail secured within the marrow canal, a bone plate fixed to the periosteal surface, or a combination of plates & nails, sometimes complimented with lag screws [8]. With each fixation method having their own advantages and disadvantages [9]–[12]. Ideally, fixation prevents further displacement of the bone segments and encourages bony healing in the damaged region by alignment of these segments.

Supracondylar fractures generally propagate through both cortical and cancellous bone and often require surgical intervention in the form of a bone plate, K-wire (smooth rigid wires used for fracture stabilization), or IM rod fixation [2], [13]–[15]. For supracondylar fractures, plates have been reported to be more beneficial than other fixation methods as they have been shown to provide better alignment than an IM rod in some cases [10], [16], [17]. For complicated fractures such as

supracondylar fractures, it is imperative to optimize fixation strength and stiffness to ensure good healing and to reduce the risk of non-unions or delayed healing.

In order for healing (i.e., bony bridging) to occur in cases of fragmented or displaced bone fractures, orthopaedic hardware should align and sufficiently stabilize the fracture region. Alignment of the bones is important as it encourages the woven bone within the callus to bridge the fracture gap. Proper alignment also ensures that the regional vasculature can form at the fracture gap. This is important as the vasculature supplies vital nutrients required by the mesenchymal progenitor cells to differentiate into fibroblasts and chondrocytes, the precursor cells required for bone formation [18]. These bone formation cells create an extra-cellular matrix that eventually replaces the entire hematoma at the callus site with bone [18].

1.2 Orthopaedic Hardware

Approximately 10% of orthopaedic devices used in the United States require a second surgical intervention due to non-union [19]. This number can be as high as 25% in lower extremity diaphyseal and metaphyseal fractures [20], [21]. Cases of non-union cause an approximate average of \$24,500 in additional costs per case, associated with the necessary revisions and added recovery time [22], [23]. It is theorized that a primary cause of these non-unions is undesirable mechanical stability at the fracture site. Succinctly, the formation of woven bone has a tolerable strain magnitude that, if exceeded, will slow or completely prevent bony bridging, leading to delayed union or non-union [24]. Therefore, designing fracture fixation hardware that is optimized for bone growth would have a significant clinical and socio-economic impact.

Fracture fixation devices are also designed to limit deleterious mechanical forces being imparted to the surrounding soft tissues, such as muscle, by reducing excessive motion at the fracture site [25]. Typically, implants are selected by the surgeon based on the bone fractured and the trauma type. Plates are often contoured by the surgeon intra-operatively to allow for patient-specific bone geometric variability [26]–[28].

Fixation devices are often manufactured from stainless steel, cobalt (various Co–Cr–Mo alloys) or titanium alloys (primarily F67, F136, or Commercially Pure Ti) [29], [30]. These materials are strong, with yield strengths ranging from 170 MPa (i.e., stainless steel 316L) to 920 MPa (i.e., Ti6Al7Nb) [29], while also being bioinert [31], a critical property for implanted devices.

Material properties of implants are important as the greater the modulus of the selected metal, the higher the amount of stress shielding that will occur for the bone it contacts. Stress shielding is the process of bone resorption caused by a large reduction in local stress, often due to implant materials having much larger elastic modulus than the adjacent calcified tissue [32]. This is undesirable as it can lead to an increased risk of future fracture due to weakened bone [33]. Novel materials such as polymers, ceramics, and other metals such as magnesium, have been proposed for tailoring the mechanical behavior of implanted devices as a means to improve healing and reduce stress shielding [34]–[37]. Some of these novel materials have had relatively good success in improving therapies via biodegradation [36], or moldable implants [34]. For example, Staiger et al. reported capabilities of magnesium, a metal with a much lower modulus than stainless steel (41-45 MPa for magnesium vs 170-310 MPa for steel), for improving tissue healing compared to typical implant

materials. In addition, this study showed that the implants can degrade safely over time. As early as 1932, Lambotte et al. implanted magnesium IM nails to treat supracondylar fractures in children and showed complete successful healing of the fractures, as well as complete resorption of the implanted devices [38]. Additionally, studies have shown that stress shielding is reduced by using biomaterials that have moduli near that of healthy bone [35]. However, metals (stainless steel, cobalt metals, and titanium alloys, predominantly) remain prevalent in the field and make up the majority of load-bearing implants as they have been proven to be mostly safe for biological applications and sufficiently strong for most fracture types and locations.

The most common stainless steel alloy used for orthopaedics is 316L [12], estimated to make up nearly 60% of all surgical implants in the United States [39]. When compared to titanium and cobalt alternatives, 316L is markedly easier to machine and is a less expensive bulk material [39]. This makes stainless steel a good option for complex machined hardware, allowing purpose-specific designs to be explored for improving fracture care.

It is clear that the design of fracture fixation devices is an important factor for helping to direct the healing cascade. Material selection and geometry are both important factors in eliminating excessive strains across the fracture while minimizing stress shielding. Therefore, understanding the relationship between implant mechanics and fracture healing is critical for developing new implants which may optimize healing on a patient-specific basis.

1.3 Micromechanics of Fracture Gap

As fracture healing progresses through the cascade from inflammatory response, to callus to remodeled bone [40], [41], the mechanical properties of the fracture region change and the relative motion at the fracture gap decreases [42]. In stabilized fractures, as the healing cascade progresses, the callus begins to take more load (as compared to the supporting hardware) in a load-sharing phenomenon characteristic (i.e., the load borne by the hardware decreases as the load borne by the newly formed bone increases) [43]. In situations of poor healing, this transition of load is not observed or is significantly delayed (as compared to natural healing), and, the fracture region does not reach adequate levels of mechanical stability. Reasons for non-union can range [44], [45], however, the primary factor is believed to be the over or under mechanical stimulation of the fracture region and surrounding tissue. This mechanical stimulation is in the form of mechanical strain, which is not adequate or too excessive to accommodate the development of the desired tissues [46]. A theory was developed by Pauwels et al. [47] that the strains, and the stresses attributed to those strains, have a causal effect on tissue differentiation at the callus. Thus, the mechanical loads at the fracture are theorized to directly determine the healing viability of a fracture.

As fractures heal they undergo either primary or secondary bone healing [48]. The type and degree of healing is determined by the type of tissues at the fracture gap. Intramembranous ossification describes the characteristic healing involving direct differentiation of mesenchymal cells into compact bone structures. This leads to immediate secretion of extracellular bone matrix that quickly calcifies into new bone [49]. Endochondral ossification is the process of intermediate cartilage being formed to bridge the fracture gap which is later replaced by bone in a number of

stages (i.e., soft callus to hard callus to bone remodeling). While intramembranous ossification is usually observed in primary (contact) healing, endochondral ossification is more commonly observed in long bone fracture healing wherein the fracture bone termini are not in direct contact [49].

Primary bone healing only occurs when rigid fixation is achieved for bone segments in close proximity. Therefore, in segmented fractures, commonly seen in long bone trauma, the conditions for primary healing does not exist. Secondary bone healing consists of both endochondral and intramembranous ossification [50]. Secondary bone healing takes more time due to the lengthier processes required for the endochondral ossification process.

In line with Pauwels et al.'s theory [47], the loading mechanics in the fracture gap directly influence which type of healing (primary, secondary, or none) is possible. Therefore, an approach to bony fracture fixation should fundamentally include design for the mechanics in the callus region if the desired healing outcome (i.e., bony union) is to be obtained.

It is known that relatively high levels of motion at the fracture site, which generally correlates to high stresses at the fracture site, can cause damage to the healing tissue, essentially preventing effective bony bridging [51]–[54]. But the opposite (low level of motion, correlating to low stresses) is also possible, and can also lead to poor healing outcomes. Motion at the fracture site causes the loading of osteons (i.e., the primary units that comprise cortical bone [55]) in the adjacent healthy bone. Mechanical stimulation of the osteonal matrix cells, namely the mechanosensitive osteocytes, causes the biological regulatory signals that drive bone remodeling

[55], [56]. A low level of motion often results in levels of stimulation of osteonal matrix cells that is too low to encourage cell proliferation and tissue rebuilding [53], [57], [58].

Low magnitude stresses in the callus/bone can also lead to stress shielding in surrounding bone, resulting in unwanted bone resorption as osteoclastic activity is over encouraged. Studies have shown that surface strains of approximately 2-5% across the fracture callus promote intramembranous bone formation [59], while strains above 10% will generally prevent early bone formation [60]. It has been reported that specific hydrostatic pressure and strain envelopes correlate with connecting tissue development. Specifically, Claes and Heigele's work indicated that intramembranous ossification occurs between $\pm 5\%$ strain and hydrostatic pressures smaller than ± 0.15 MPa, while endochondral ossification occurs below -0.15 MPa and strains smaller than $\pm 15\%$ [59]. These data also suggest that connective tissue/fibrocartilage formation, not ideal for satisfactory bony healing, is initiated at values of strain and pressure outside of these envelopes [59].

Therefore, fracture gap mechanics (strain and pressure envelopes), as well as geometric and bioinert considerations, are the fundamental criteria that should be accounted for when designing orthopaedic hardware. Currently, hardware design is relatively generalized for fracture cases. However, selectively designing implant-bone mechanics for case specific purposes has been recognized as an area that could significantly improve bone healing success [5], [61], reducing the rates of non-unions.

1.4 Hardware Strains and Fracture Non-unions

Non-unions that require surgical re-intervention can be difficult to diagnose. Determination of non-unions require radiographic evidence of calcified tissue's failure to bridge the fracture gap and a clinicians' physical examination [62]–[64]. As the fracture heals, and calcified tissue forms, the tissue density at the fracture site increases. Unfortunately, radiographs cannot detect small changes in tissue density in the early stages of healing [65] and thus, diagnoses can only be conducted during later stages of healing. Ebraheim et al. found the average time for a diagnosis for metaphyseal fractures was 36 weeks [66]. This time can be even longer for slow healing bones [67]. Techniques for monitoring the fracture health during these first few weeks of healing, which are crucial for union, would provide valuable information for improving therapies utilized to treat non-union patients. Faster diagnosis of non-unions or delayed unions would allow clinicians to prescribe the appropriate remediation (i.e., device removal, physical therapy, steroids etc.) earlier in the healing period, potentially leading to a shorter recovery time which would translate to a reduced burden on the patient.

It has been demonstrated that it is possible to determine fracture healing viability via measurable or predictable fixation device mechanics. For example, work by McGilvray et al. showed that monitoring the strains experienced by the implanted hardware over a normal healing period (approximately 8 - 16 weeks for long bone fractures to achieve bony bridging [68]), can be indicative of fracture healing success or failure [69]. This observation is based on the correlation between hardware strain and fracture gap strain [70]. Fracture gap tissue strain has been shown to be the primary intermediate causal factor correlating bone loading to remodeling [46], which is key for healing viability (i.e., union vs non-union). By monitoring hardware strain and, therefore,

the resultant strain in the fracture region, researchers would have insight into the types of tissue differentiation that are potentially occurring at the fracture. These data make it possible to predict the healing that is occurring and provide delayed union and non-union diagnoses early in the healing period. However, there is a gap in literature and no current technology exists to easily measure strain on implants in human patients.

Some studies have succeeded in acquiring measurements on animal specimens [71]–[73] including Grasa et al. who managed to monitor *in vivo* loads using an external fixator on ovine specimens [74], while Stoffel et al. measured plate loads with strain gages on ovine specimens [75]. Both studies showed a reduction in mechanical hardware strain as the fracture healed (Figure 2). However, these studies utilized strain monitoring techniques that are not applicable to wide-scale human clinical application. A minimally-invasive method for measuring instrumentation strain *in vivo* would be largely beneficial in clinical applications as it could allow temporal fracture healing monitoring via hardware strain measurements.

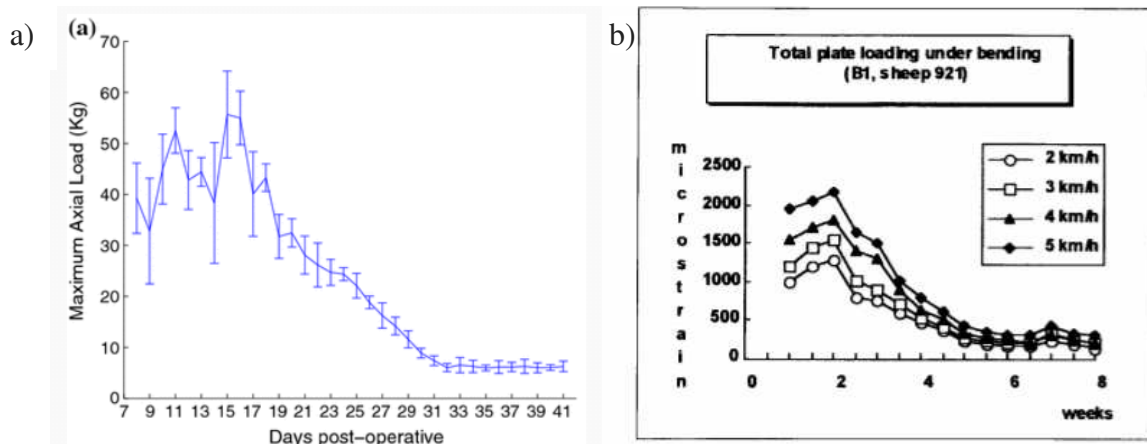


Figure 2: a) Grasa et al. reported the axial load (Kg) measured in an external-fixation on ovine tibial fracture model (surgical osteotomy). The resulting axial loads (Kg) through the external fixator in one sheep (mean and standard deviation) vs days post osteotomy are shown [74]. b) Stoffel et al. tested a similar sheep tibial fracture model but fixed with a bone plate. They recorded hardware strain via wired strain gages as the sheep walked on a treadmill at different gait speeds. An example of total plate surface strain under bending for different gait speeds in the ovine tibial osteotomy model is shown [75].

1.5 Finite Element Analysis

One possible method for investigating the *in vivo* mechanics of a stabilized fracture is the use of *in silico* finite element analysis (FEA). FEA combines a set of powerful analytical tools, including the finite element method [76], that can be utilized for biomedical research [77]. It is often hard to measure the mechanical behavior of soft and complex hard tissues, especially for systems that are intractable to perform analysis *in-vivo*. However, validated FEA models allow investigation of local and global mechanics of complex tissues with relative ease [78], [79].

A number of studies have been conducted on human and animal femoral models [80]–[82] including a previous study that investigated the ovine tibiofemoral contact forces using an *in vivo* ovine hind limb model [83]. For these and all FE analyses, the mechanical properties are important for accurate *in silico* simulations. When modeling supracondylar fractures, cortical bone and cancellous bone properties both contribute significantly to the overall mechanics of the FEM. Geometry and boundary conditions of the model also play an important role. Therefore, it is of critical importance to insure that the dimensions, boundary conditions, and loads applied in the FEA model are close as possible to “real world” conditions.

Fortunately, acquiring accurate geometric representations of biologic hard and soft tissues has become much easier in the modern era using advanced imaging technology such as computerized tomography (CT) scanning or magnetic resonance imaging (MRI). These techniques allow 3-dimensional imaging of objects in a Digital Imaging and Communications in Medicine (DICOM)

format which can be used to generate 3-dimensional surfaces using specialized computer software packages like Amira (6.5.0, Thermo Fisher Scientific, 2018).

FE models that predict plate fixation mechanics and/or fracture gap mechanics would allow fracture healing predictions to be made based on a range of criteria (i.e., plate stiffness, plate geometry, and callus properties). If the FE model is validated, it would be possible to make informed predictions of tissue type proliferation and guide clinicians decisions for device design and selection.

1.6 Problem Statement

Non-union of stabilized fractures is a common problem that could be prevented in many cases. Fixation hardware stiffness has been correlated to the fracture gap mechanics which, in turn, directly drives the types of tissue proliferation that can occur within the callus. Therefore, by changing bone plate stiffness, fracture healing can be driven towards better healing outcomes compared to using bone plates of generic stiffnesses. Therefore, the goal of this thesis project was to investigate callus micromechanics as a function of altering plate fixation stiffness to control the type of tissue differentiation and the resultant quality of healing. An ovine supracondylar fracture finite element model was generated and utilized for the study. Different thickness fixation plates were designed and manufactured to stabilize ovine supracondylar fractures. These plates were used to stabilize an *ex-vivo* ovine supracondylar fracture model and mechanically tested to validate finite element models. Data from these models were used to predict callus micromechanics.

2. Specific Aims

2.1 Objective

The overarching objective of this thesis work was to investigate the effect that fixation plate thickness on supracondylar fracture region mechanics. An ovine supracondylar fracture FE model was created for the purpose of this study. Computational ovine femur supracondylar FE models stabilized with plates of varying thickness were evaluated. These models were validated with *ex-vivo* experimental results and were then used to predict callus mechanics.

2.2 Specific Aim 1

The first aim of this work was to computationally simulate a plated ovine supracondylar fracture model. The model was used to investigate the influence of three different plate thicknesses on the mechanical behavior of the plates and the micro-mechanical environment of the fracture callus over a simulated healing cascade.

2.3 Specific Aim 2

The second aim of this work was to conduct bench-top experiments on simulated supracondylar fractures that were stabilized with plates of 3 different thicknesses in an ovine cadaveric model and compare the results to the computational models for validation.

3. Model Creation and Validation Materials and Methods

3.1 Sheep as a Translational Animal

Representative, biological models of human disease and trauma are necessary for proving the efficacies of novel clinically intended technologies. Sheep have been used in translational medical research for a number of musculoskeletal applications, such as soft tissue trauma, osteoporotic models, and fracture models [84]–[88]. This is because sheep have similar weight and [84] comparable bone size to humans [89]. Sheep also exhibit relatively similar age related changes in bone as compared to human [89]. Another important similarity between skeletally mature sheep and humans is sheep’s large primary bone structure that includes Haversian canals. Haversian canals are microscopic tubes of bone that, once reformed, allow blood vessels to regrow in the fracture region. This allows blood to transport osteoblastic pre-cursors [48] that are crucial for bone healing [90], yielding bone remodeling properties similar to humans [91]. These similar structural, architectural, and healing properties of bone provide support for the translation of research performed with ovine models as a basis for understanding human orthopaedic healing. Therefore, an ovine model of supracondylar fractures was selected as an analog for similar human fracture cases.

3.2 Supracondylar Fracture Model Design

A novel model was generated in order to complete the proposed work. Board certified orthopaedic veterinary surgeons (PSRL, Colorado State University, Fort Collins, CO 80521, USA) were consulted to create an ovine model of a supracondylar fracture in ovine specimens. The goal

was to generate a fracture pattern in the ovine femur that would be representative of human fractures using standard surgical techniques. Standard osteotomy techniques often involve using an oscillating saw to transect the simulated fracture region. Skeletonized ovine femurs were isolated and skeletonized to investigate different regions of transection (Figure 3).

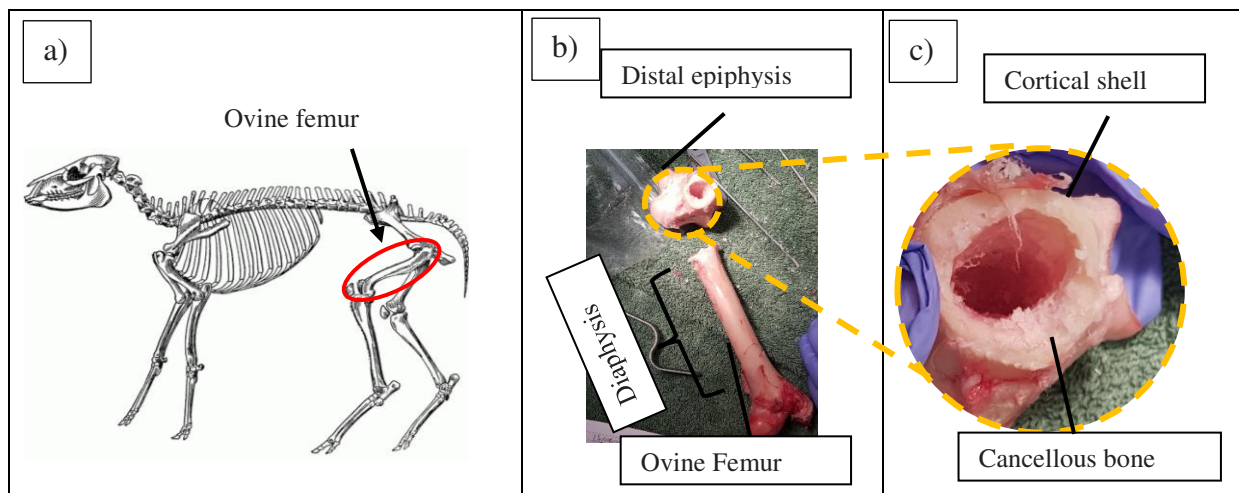


Figure 3: (a) Ovine skeleton illustration showing where the femoral bone is located. (b) Transected femur with an end view of the sectioned distal epiphysis that was checked to confirm cortical and cancellous bone regions to determine the supracondylar fracture model transection location. (c) an enlarged image of the cross section of the ovine supracondylar region illustrating the cancellous and cortical bone

The models' fracture site was selected directly proximal to the femoral condyles (approximately at the inferior aspect of the metaphysis and the anterior aspect of the distal epiphysis), a common region seen clinically in human supracondylar fractures (Figure 4a). This region was selected as both cortical and cancellous bone were directly adjacent to the fractured region (i.e., it cut through both bone constituents), a critical phenomenon observed in clinical cases of supracondylar fractures (Figure 3c) [92]. This novel model involved using a vibrating saw to cut bi-cortically through the identified region creating an approximate 3 mm fracture gap (Figure 5).

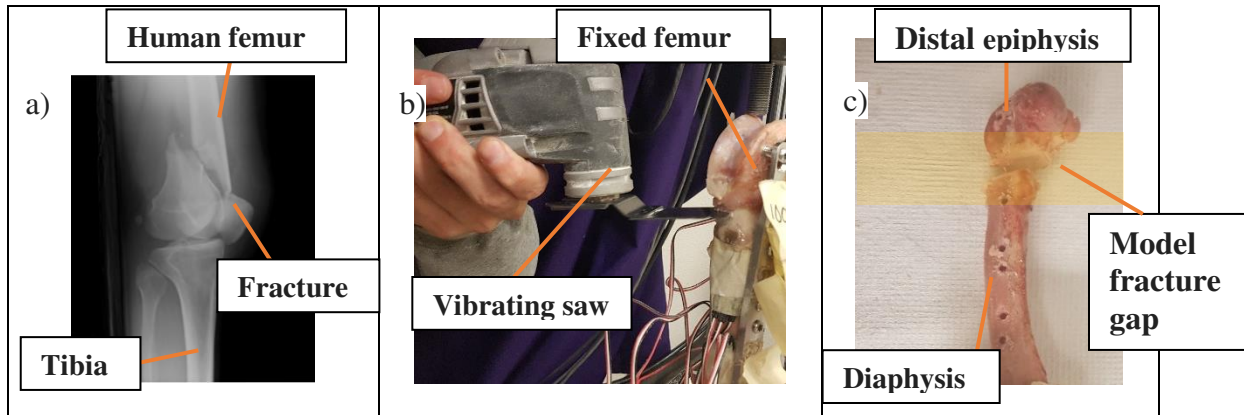


Figure 4 : (a) A radiograph image of a human supracondylar fracture of the femur [86] (b) An image of a vibrating saw being used to transect the femur to create the supracondylar fracture model (c) An image of an isolated, skeletonized ovine femur with the transected ovine femur model applied for this study (note: the holes in the femur are from the screws that fixed the plate to the bone while the osteotomy was made as seen in (b))

The supracondylar fracture model was designed to require plate fixation, however, no sufficient ovine-specific supracondylar fracture plate was found. Thus, new plate designs were required to stabilize the novel fracture model.

3.3 Plate Design

The design and manufacturing of novel plates with different plate thicknesses was required to test this study's aim of investigating the effects of plate stiffness's effect on callus mechanics (i.e., specific aim 1). The plate's initial design was based on a type of contoured bone plate that is commonly used to fix distal and proximal long-bone fractures in humans (Figure 5) [93].



Figure 5: A locking compression plate (LCP) for distal femurs produced by DePuy Synthes (LISS LCP distal femur plate, DePuy Synthes, Raynham, MA) for human use [93].

To ensure the plate would fit the size and shape of an ovine femur, an isolated and skeletonized ovine femur was imaged using a PET-CT-scanner (0.29x0.29x0.8 voxel dimensions, Gemini Big Bore, Philips Healthcare, Amsterdam, Netherlands). To generate a representative *in silico* model, three-dimensional surfaces of both cortical and trabecular bone were segmented from the resulting DICOM data using Amira (6.5.0, Thermo Fisher Scientific, 2018; Figure 6).

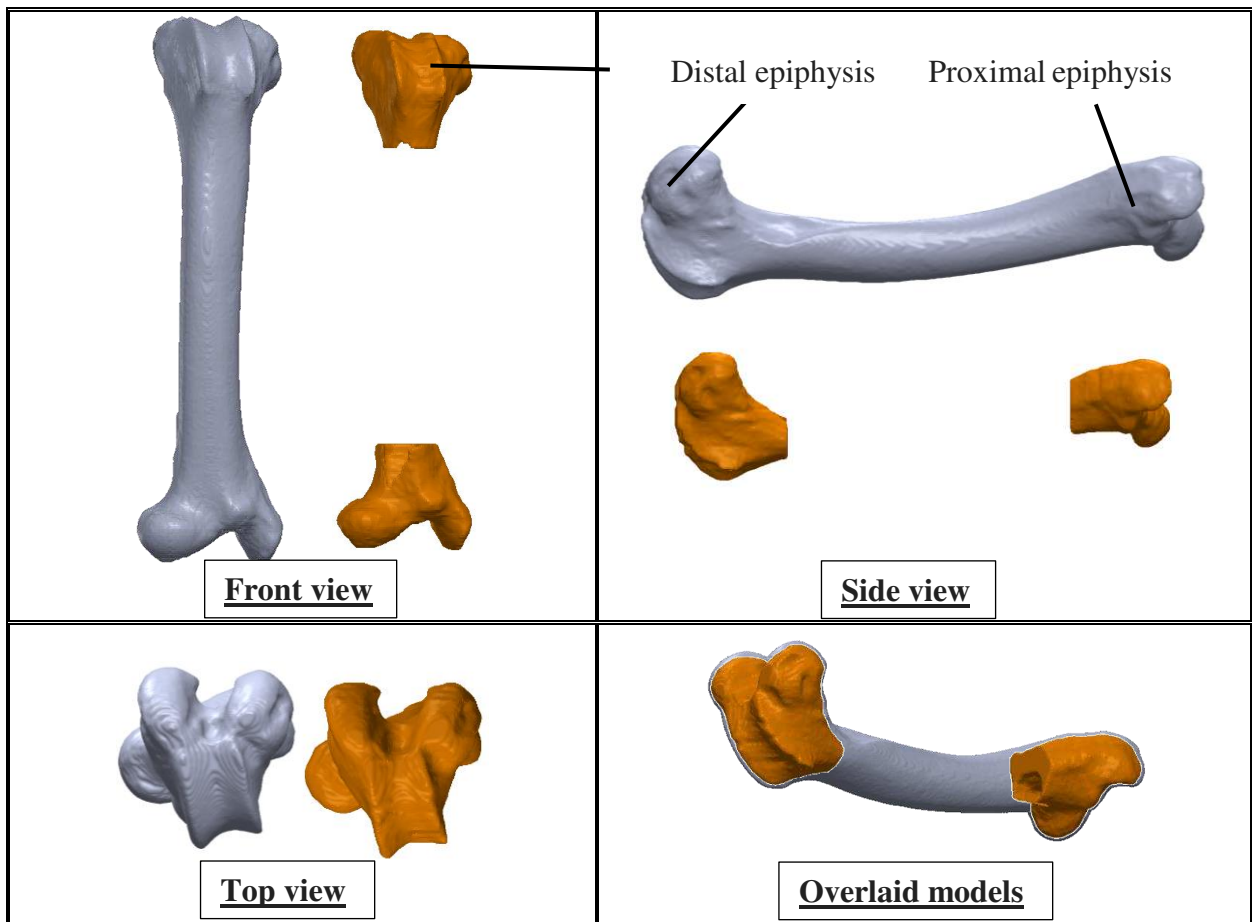


Figure 6: Rendered 3D ovine femur surface models of both cortical (grey) and cancellous bone (orange) created from CT DICOM data using Amira shown in 4 different views. The grey model is the cortical bone surface model and the orange represents the cancellous bone surface model

Using the 3D femoral bone surface model, a 3D spline model of the plate was created in SolidWorks (2016, Concord, Massachusetts: Dassault Systèmes). The 3D spline model was adjusted to match the geometry of the ovine femur's 3D surface (Figure 6). This was done by creating conforming cross-sectional shapes on 20 planes parallel with the bone model's transverse plane and lofting a boss (protruding feature/solid) through all the individual sketches (Figure 7).

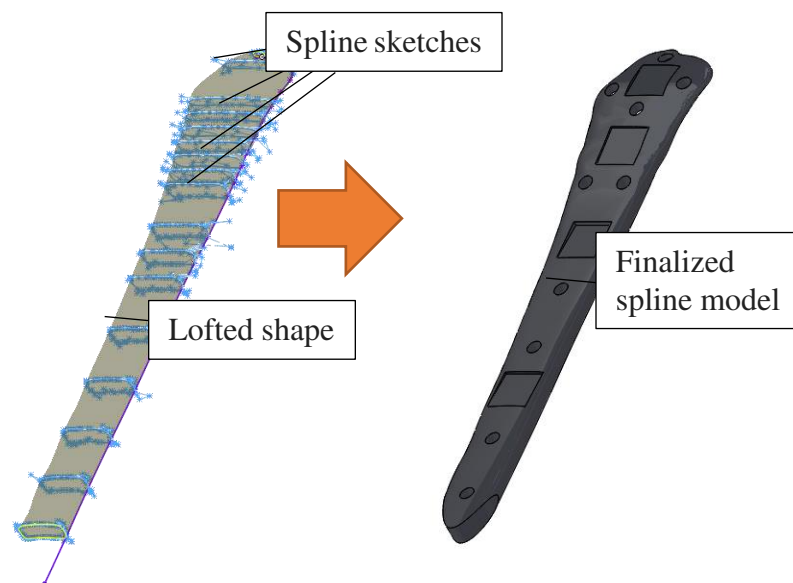


Figure 7: The sketches for creating the lofted spline plate model that was designed to conform to the 3D ovine femur model geometry. On the left is the lofted shape through all 20 sketches, and on the right is the final spline based plate geometry model.

The 3D model was then converted to a geometric model that could be exported for computer numeric control (CNC) fabrication. Stainless steel 316a alloy was selected as the base plate material due to its bioinert properties and ubiquitous previous clinical usage [39], [94]. The plate design was iteratively modified (via 3D prototyping and assessment by the veterinary surgical advisors) to meet the geometrical requirements of conforming to the ovine femur, as well as the mechanical requirements (estimated via simple bending and axial stress analysis of a rectangular

block geometry) for strength required to stabilize an ovine supracondylar fracture in a sheep. Iterative changes, including modifying the number and location of holes, types of holes (combination (combi) vs locking holes), and general plate geometry to best match the ovine femurs were performed. The geometric requirements for the plate were such that the plate needed to match the bow of the ovine femur including the geometry around the epiphysis. Additionally, the screw holes had to have sufficient distance from the edge of the bone such that the risk of unintentional fracturing of the surrounding bone was reduced. Plate prototypes were made with additive manufacturing methods for physical comparison (Figure 8).

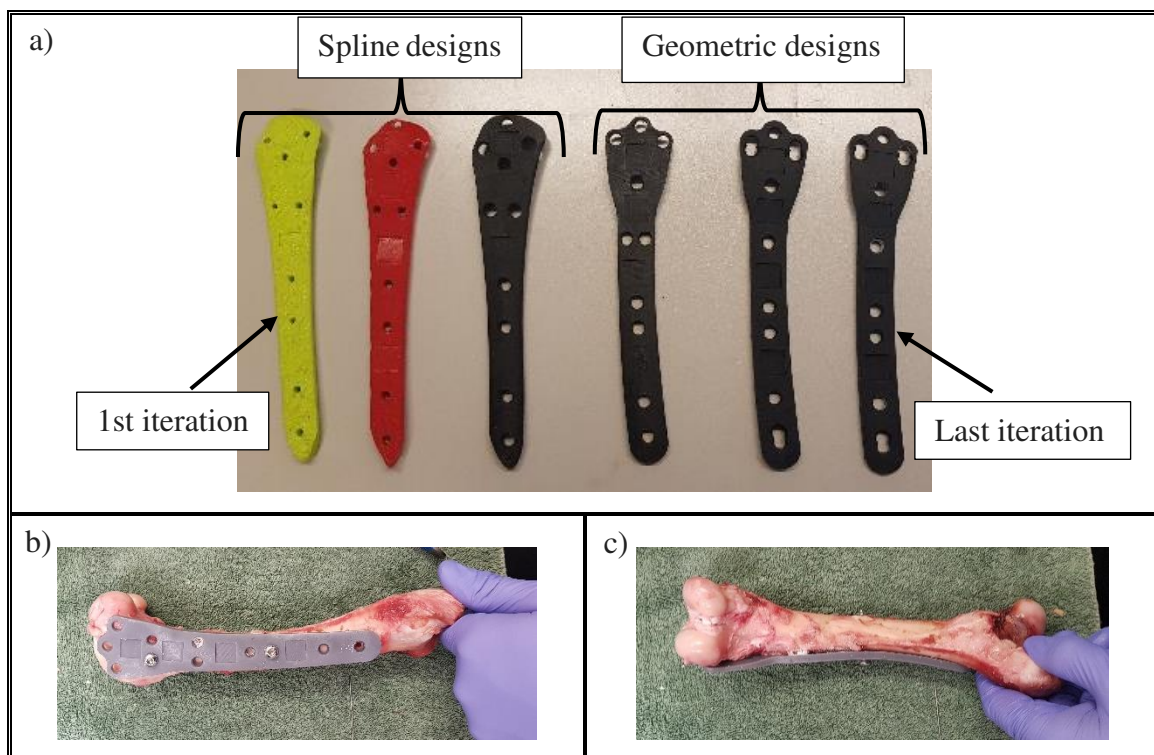


Figure 8: (a) Six generations of plate design from the first print on the left to the final plate design on the right. The prototypes were all printed using varying types of extrusion additive manufacturing (b) and (c) a size comparison on a skeletonized ovine femur using the 4th plate design seen in (a)

The final design of the plate (Figure 9) incorporated nine 5.0 mm, bi-cortical locking screws (Veterinary Orthopaedic Implants, St. Augustine, FL), which included 3 in dynamic locking holes (holes that allow screws to be inserted at angles for improved angular stability; Figure 9). There were also four 5.0 mm screws designed into the epiphyseal region of the plate to secure the condyles and another five 5.0 mm screws were located centrally down the diaphysis (Figure 9). The plates were also designed with 4 depressed, flat square regions to accommodate the strain sensors (Figure 9).

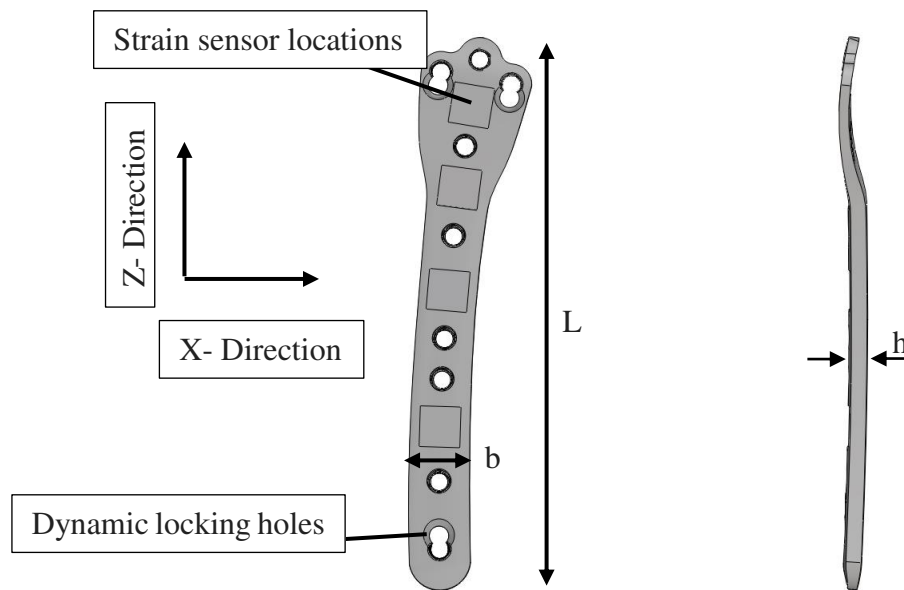


Figure 9: The finished plate design front view and side view of the thick (4.6mm) plate. X and Z direction are indicated here as are basic dimension nomenclature for describing the plates. L is the length of the plates, b is the width of the plates, and h is the thickness of the plates.

Three different plate thicknesses were designed (i.e., $h = 4.6$ mm, 3.8 mm and 3.2 mm thick; Figure 9). By altering the thickness of the plates, the implant's stiffness was increased or decreased with design goals of approximate relative stiffness of 100% (i.e., 4.6 mm), 85% (i.e., 3.8 mm) and 66% (i.e., 3.2 mm). The goals for each stiffness were selected arbitrarily for this pilot study as it was unclear what relative stiffness levels would cause significant changes without previous

investigation. These relative stiffnesses were based on empirical calculations where the stiffness was linearly correlated to thickness. Equations 1 - 3 show the basic equations used to calculate bending stiffness as a function of plate thickness and deformation. ϵ is the bending strain, m_x is the bending moment about the x-axis (Figure 9), E is the elastic modulus, I_{xx} is the second moment of area about the x-axis, b is the width of the plate (Figure 9), h is the plates thickness (Figure 9), F is the axial force, and D is the distance of the moment arm at which the load was applied:

$$\epsilon = \frac{m_x y}{EI_{xx}} \quad (1)$$

$$I_{xx} = \frac{bh^3}{12} \quad (2)$$

$$m_x = FD \quad (3)$$

E, F, and b, were kept constant between all 3 plates as the material, loading type, and planar dimensions of the plates (width and length) were uniform for all plate variants. As D and y were both linearly dependent on thickness (h), Equation 1 (via Equation 2 and 3) was simplified to;

$$\epsilon \propto \frac{h \times h}{h^3} = \frac{1}{h} \quad (4)$$

By varying the plate's design thickness, it was theorized that changes in the plate's mechanics would directly change the fracture's micromechanics which, in principal, would allow a level of control of the biomechanical behavior at the fracture region.

Similar modifications to implant stiffness have been previously studied, however, the general approach in those investigations has been to change the plates base material (as compared to implant geometry) in an effort to change the implant's stiffness [95]–[97]. By keeping the material constant and altering the stiffness via geometric alterations, it was theorized that it would be possible to examine which plate would provide the best chance of bony union for supracondylar fracture scenarios. The final plates were manufactured using 3-axis CNC machines and supplied by Artmedics (Artmedics LLC, Minneapolis).

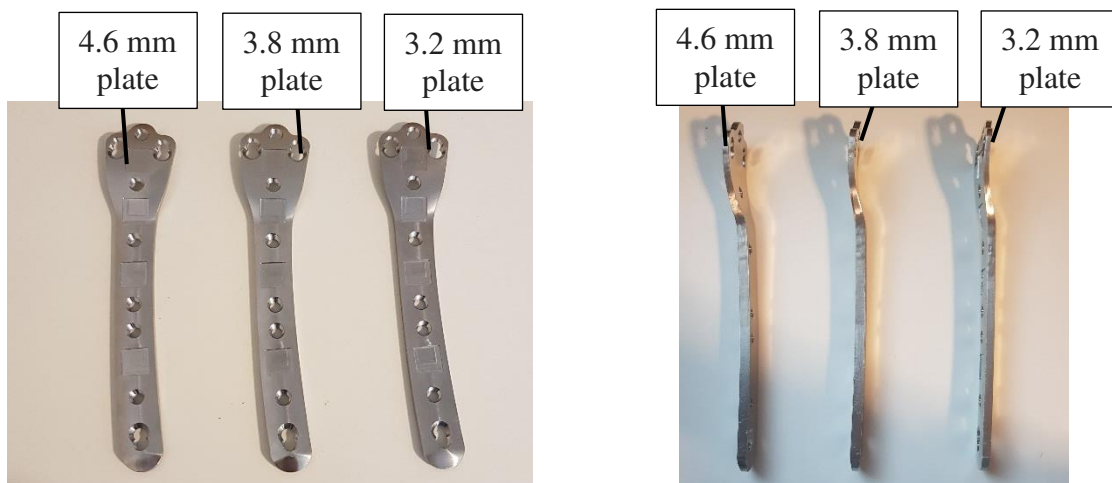


Figure 10: The manufactured plates in decreasing thickness left (4.6 mm) to right (3.2 mm)

3.4 Finite Element Model Generation

3.4.1 Femur Model Development

The femoral surface model used for geometric design of the plates (acquired from CT-scan DICOM data) was also used to generate the FEA model. The surface models of the femoral cortical and cancellous bone were exported and meshed via Bolt (2.0, csimsoft, 2018, American Fork, UT, USA) using hexahedral (hex) elements. Hex elements were selected as they allowed the prediction

of stress/strain gradients within a single element. This property provides better integration over the gauss point as compared to tetrahedral elements, generally resulting in more accurate predictive models for simulations where substantial shear or bending is expected [98]. The final meshed geometry was imported to ABAQUS (2018, Dassault Systemes, Velizy-Villacoublay, France) for finite element analysis. Figure 11 illustrates the steps taken to create the final bone geometry.

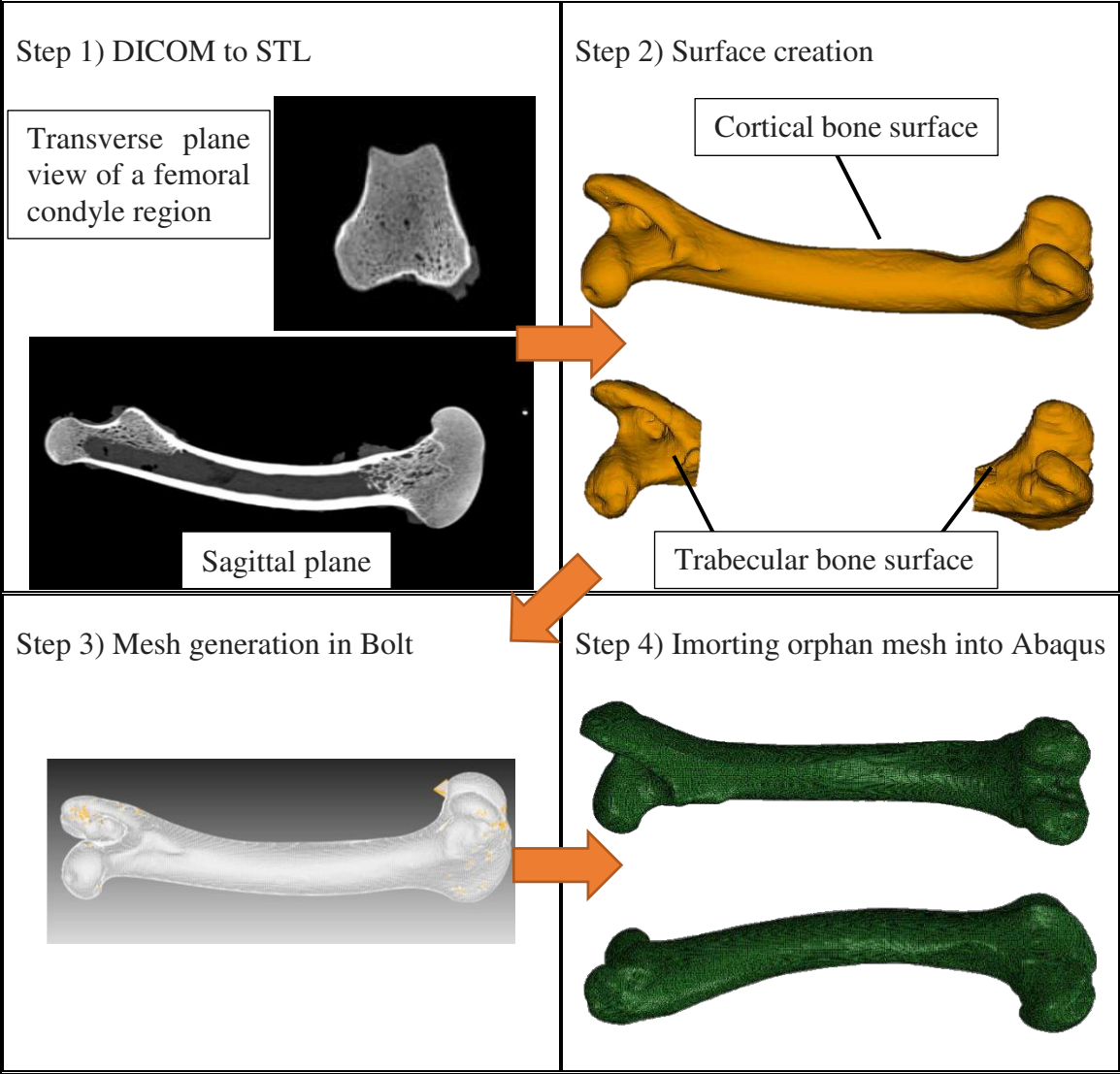


Figure 11: Steps taken to generate an ovine femoral model for finite element analysis.

3.4.2 Material Properties

Material properties are an important consideration for FEA implementation. Bone is generally considered a composite material consisting of two primary constituents: cortical (compact) bone and cancellous (trabecular) bone [99]. In long bones, cortical bone makes up the diaphyseal shaft and the thin layer of bone at the metaphysis and epiphysis [100] (Figure 12). Cortical bone is characterized as dense bone with orthotropic (i.e., directionally-dependent) mechanical properties (with elastic moduli reported to be between 8 - 28 GPa and a Poisson's ratio reported in the range between 0.3 - 0.47 [101], [102]). Cancellous bone is characterized by less dense, porous bone, generally comprising the interior of the regions encased by the metaphysis and epiphysis [100]. Cancellous bone consists of trabecular struts, arranged parallel to the dominant loading history, and have orthotropic properties (i.e., elastic moduli and Poisson's ratio).

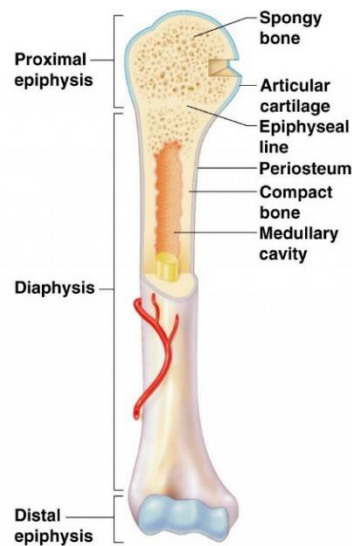


Figure 12: Anatomy of the cross section of the proximal half of a femur indicating the spongy (cancellous) and compact (cortical) bone. [103]

After the bone's FEA mesh was imported into ABAQUS, the material properties of the FE femur model (i.e., cortical and cancellous bone properties) were applied. Both types of bone were

considered orthotropic [104], and linear elastic. The material properties of each FEA bone constituent are given in Table 1.

Table 1: Material properties used in FEA modeling of the femur bone model

Material	Elastic Moduli	Poisson's Ratios	Shear Moduli	References
Cortical Bone	$E_1 = 22 \text{ GPa}$ $E_2 = E_3 = 11.3 \text{ GPa}$	$\nu_1 = 0.482$ $\nu_2 = \nu_3 = 0.397$	$G_1 = 0.482 \text{ GPa}$ $G_2 = G_3 = 0.397 \text{ GPa}$	[101], [102]
Cancellous Bone	$E_1 = 542 \text{ MPa}$ $E_2 = E_3 = 406 \text{ MPa}$	$\nu_1 = 0.381$ $\nu_2 = \nu_3 = 0.104$	$G_1 = 0.482 \text{ GPa}$ $G_2 = G_3 = 0.397 \text{ GPa}$	[105]–[107]

3.4.3 Femur Model Boundary Conditions

To simulate physiological loading vectors, the FEA bone model was axially compressed on the medial side of the right condyle, aligned with the long axis of the bone (Figure 13). To accommodate a supracondylar plate in the bone-plate FEA models and bench-top tests, the proximal epiphysis was selected and assigned an encastred boundary condition (Figure 13). These *in silico* boundary conditions were implemented to simulate the bench-top testing boundary conditions (described in section 3.7.1.1). A single node was coupled to a group of surface nodes (408 nodes) on the medial condyle articular surface and a compressive load was applied in the axial direction (Figure 13). A 700 N (approximately 1.5 times bodyweight for a skeletally mature sheep [83]) was applied to the single node, which was then automatically distributed to the surface of the right medial condyle. These boundary conditions are highlighted in Figure 13.

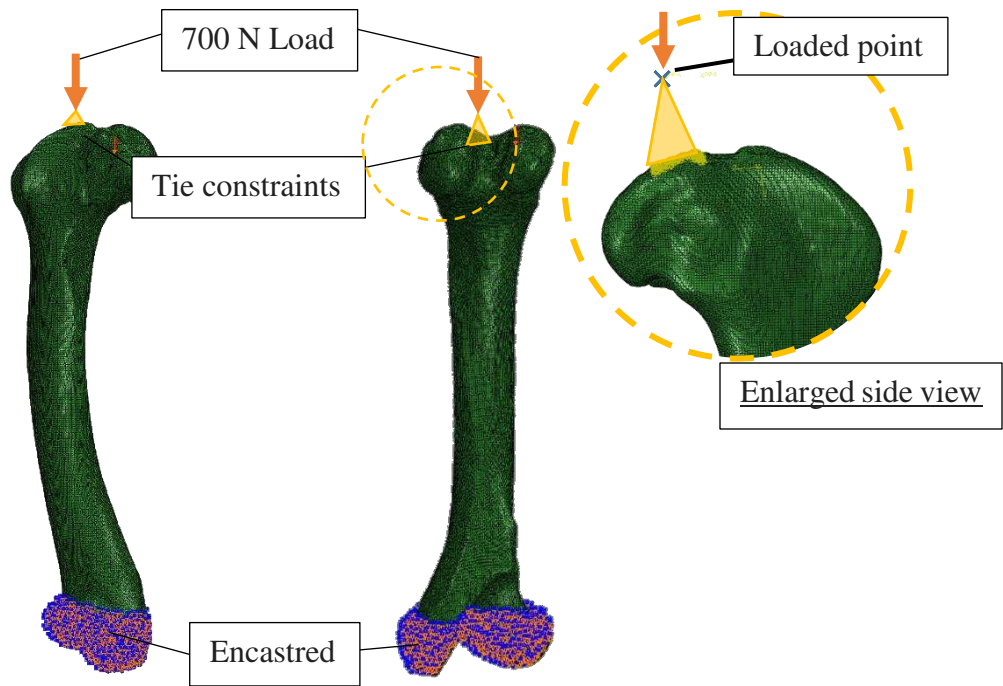


Figure 13: Image of the femoral FEA model and its boundary conditions (encastre and point load). The image on the right shows the nodes that were tied to the point of load

3.4.4 Plate Model Development

The final plate design geometries, taken from the 3D generated models (n=3 thicknesses), were meshed using Bolt (2.0, csimsoft, 2018) with hex elements. The plates' meshes were imported into ABAQUS and given material properties of stainless steel ($E = 193$ GPa and Poisson's ratio of $\nu = 0.34$ [94], [108]). The screws were modeled in ABAQUS as 5 mm cylindrical tubes with the same material properties as the plates ($E = 193$ GPa, $\nu = 0.34$).

3.4.4.1 Plate Mesh Convergence Study

To determine if the FEM predictions were independent of the mesh density, a mesh convergence study was conducted for the plate FE models. As the femur was meshed with a very high number (when compared to similar converged models in literature [109], [110]) of elements (745,150 elements, approximately 0.4 mm voxel size), the femoral mesh was considered converged.

For the plate models, a 700 N load was applied to the most distal hole at an offset that mimicked the moment arms created by the loading on the femoral condyles (Figure 14), as described in section 3.4.3. The plate was given an encastre-type boundary condition at the most proximal hole (Figure 14). The strain energy density predictions [111] of the 4 gage locations (Figure 14) were compared as the number of elements was increased from 132,458 to 985,815 for full thickness plate, 30,579 to 127,263 for 85% thickness plate, and 30,826 to 121,424 for 66% thickness plate. Results were considered mesh independent when the predicted strain energy density changed by less than 5%.

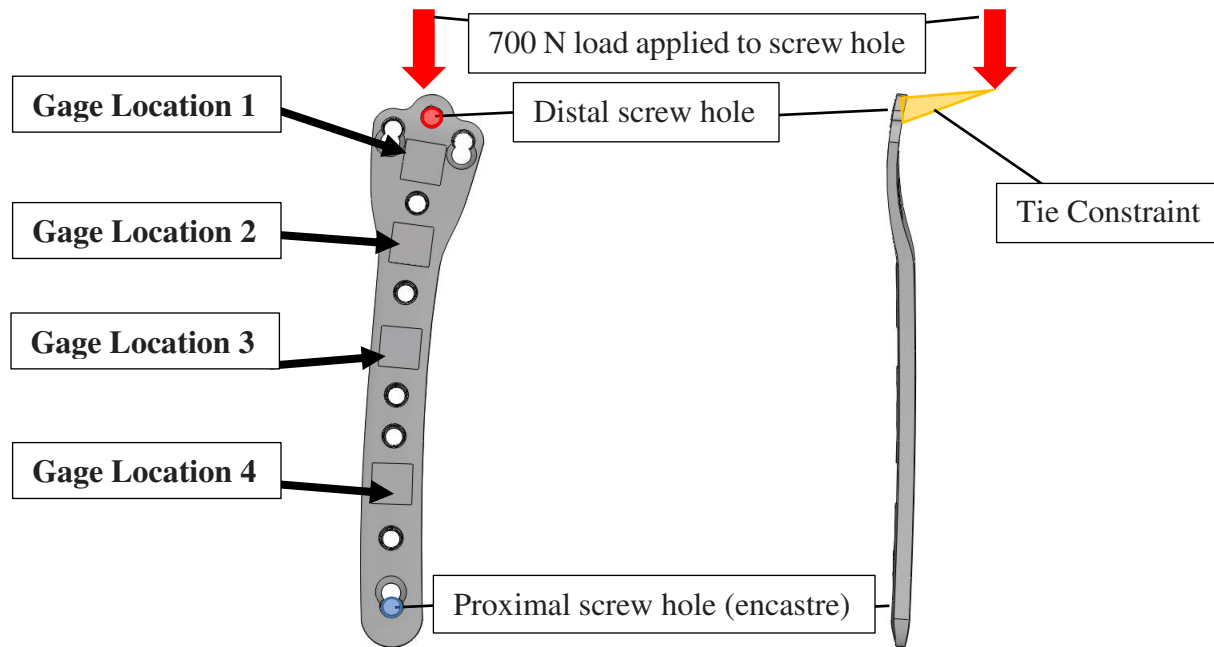


Figure 14: The loading on the plate models utilized for mesh convergence. The Proximal hole was given an encastre boundary condition and the load rigidly tied to the loading point.

3.4.5 Plated Femur Model Assembly

The plates were positioned laterally on the femur model with the widest section of the plate placed distally over the condyles (Figure 15). The plate was in contact at the most proximal point and directly adjacent to the 5th most proximal screw (Figure 15). The location of the plate was kept constant across all thicknesses of plates with the bone-to-plate proximity equivalent across all models. The 5.0 mm screws were inserted through each hole in the plate and extended through the entire thickness of the bone bi-cortically (Figure 15). The screws' surfaces were rigidly constrained to the nodes that were directly adjacent within the model femur. The surfaces of the plates' holes were then attached (i.e., tie constraint) to the screw surfaces directly in contact with them. These tie constraint boundary conditions were implemented to match locking screw behavior, similar to the locking screws' engagement with both cortices and the threaded screw holes in the plates.

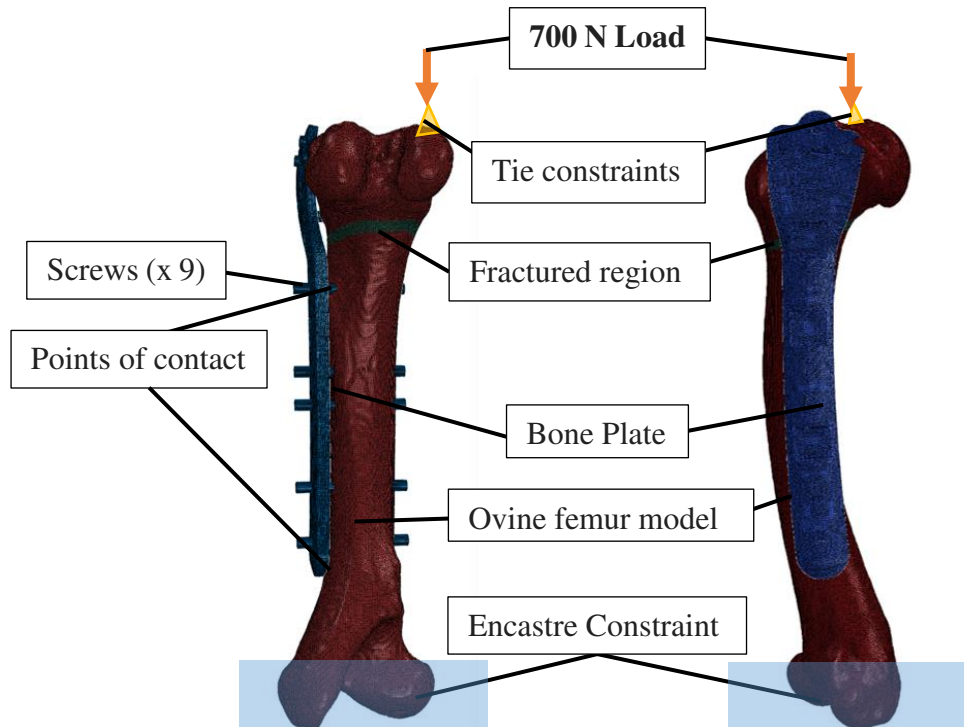


Figure 15: An image of the plate bone FE model with the thickest (4.8 mm) plate, colored by material. (Blue indicates instances with stainless steel material properties, the red regions have cortical bone properties and the green region represents the callus elements with the varying callus properties).

3.4.6 Femur Model Boundary Conditions

The FEA plated bone model was loaded identical to the femur-only model (Figure 13). The proximal epiphysis was selected and assigned an encastred boundary condition. A single node was coupled to a group of surface nodes on the medial condyle articular surface, and a compressive load was applied in the axial direction (Figure 13). A 700 N load (approximately 1.5 times bodyweight for a skeletally mature sheep [83]) was applied to the single node. These boundary conditions are highlighted in Figure 15.

3.4.7 Fracture Healing Modeling

To simulate the healing cascade, in which the callus increases its mechanical robustness over time, a discrete region of elements, approximately 3 mm wide and spanning the entire cross-section of the bone, were selected as the fracture site (Figure 16). This region was representative of the osteotomy that was created in the bench-top experiments, to simulate a supracondylar fracture. It was determined, by our veterinary surgeons, that this location and size would represent a repeatable supracondylar fracture model. The osteotomy region within the plated femur models were assigned isotropic material properties that ranged from 1000 Pa to 10GPa, values that were deemed to represent the expected temporal range of material properties of the healing callus *in vivo* [112]. By discretely varying the osteotomies (i.e., the callus) region's material properties (from 1000 Pa to 10 GPa with 6 discrete values spaced between in consecutive orders of magnitude), it was theorized that the model could simulate the healing cascade in the acute healing time frame, which has been shown to be critically important for tissue differentiation [60], [113], [114].

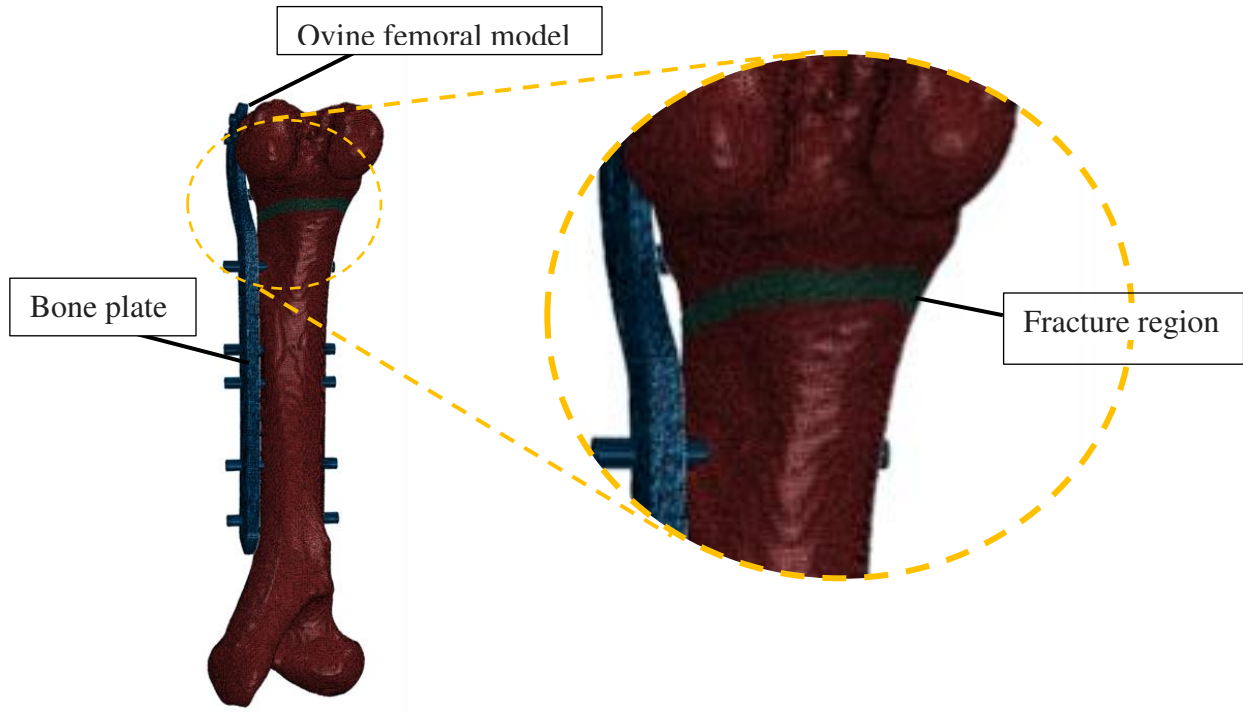


Figure 16: FE model showing elements selected for the osteotomy (a.k.a, callus or fracture) region (in green). These elements were selected for all fractured models

3.5 FEM Principal Strain Vector Investigation

Predictions from the FE bone-plate-osteotomy models showed that the orthotropic properties of the bone, geometry of the femur, and the relatively large moment caused by the offset load to the condyle generated large magnitude out-of-plane principal strains. To investigate this effect, an FEA model of a cylindrical tube with cortical bone properties (Table 1) was created and a point load (700 N), with a similar moment arms to the femur and plated models, was applied (Figure 17). The principal stress and strain vectors were predicted on the surface of this simplified cylindrical tube model to determine if these out of plane strains would be accurately measured using planar strain gages.

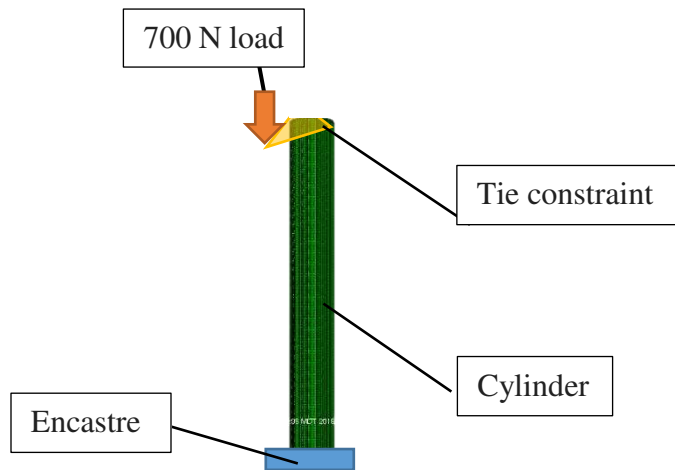


Figure 17: A cylinder FEA model with ovine cortical bone properties, simulated under a 700 N point load, similar to the femoral model.

Additionally, a single element at the surface of the femoral model was examined to determine the principal strain directions expected in a region where strain gages would be attached for the bench-top experiments (Figure 18). The predicted stress tensor at this element was probed and the values and directions of the principal strains were calculated using a stiffness matrix.

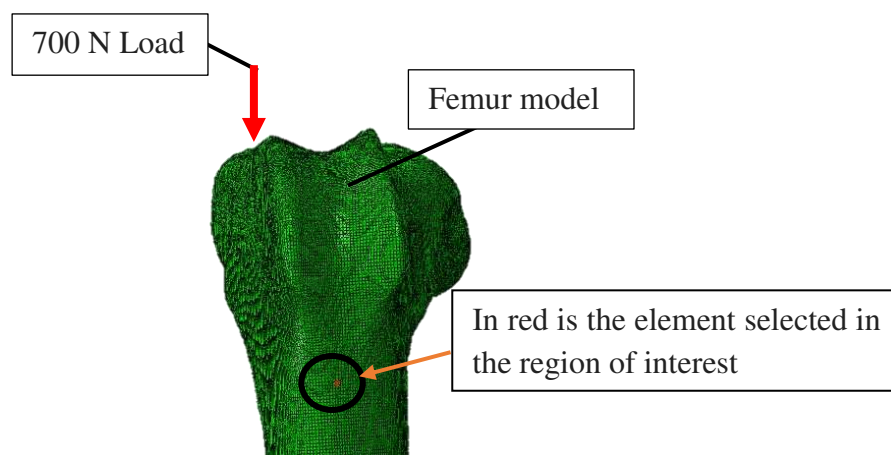


Figure 18: This circled region of femur epiphysis is where a single element was empirically analysed for strain vectors

3.6 Specimen Acquisition and Preparation

For FEA validation purposes, ovine hind limbs were harvested from animals that were euthanized for unrelated studies. The femurs were isolated and skeletonized whilst doused in a phosphate-buffered saline (PBS) solution to maintain physiological moisture content [115]. The skeletonized bones were then wrapped in saline-soaked gauze and stored in a freezer at -30°C [116]. On the day of testing, the bones were removed from the freezer and allowed to thaw at room temperature, spraying occasionally with PBS solution. Once thawed, samples were potted (Smooth Cast, Reynolds advanced materials, Denver, USA) at the proximal epiphysis with the bone being held vertical based on the long axis of the diaphysis. The orientation was chosen as the plates needed to be attached to the condyles, and thus, the condyles had to be free from the potting material for attachment (Figure 19).

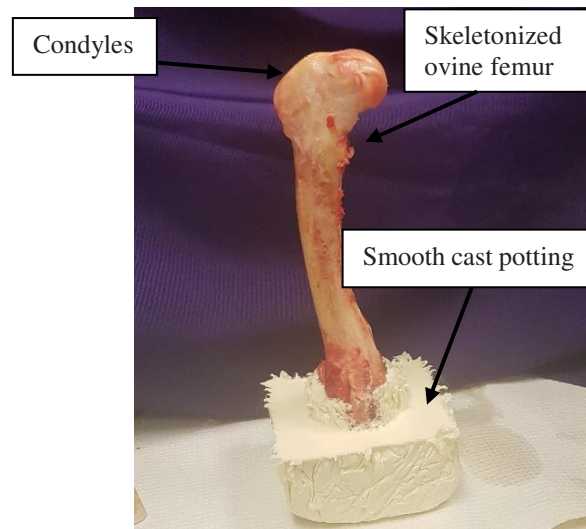


Figure 19: Femur potted at the proximal end, prior to plate attachment

The samples were placed into a servo-hydraulic mechanical testing system (MTS 858 Mini Bionix II, MTS, Eden Prairie, MN) using a custom design fixture (Figure 20a). A 12 mm indenter was

used to load the medial condyle axially on the posterior region (Figure 20b). This load setup created a combined state loading of the femur (axial loading causing bending and compression), similar to the loading of the femur seen in literature for previous cadaveric and FEA studies examining femoral biomechanics [117]–[120]. Load was measured by the MTS and by a 6-degree of freedom (DOF) load cell (MC3A-1K, AMTI, Watertown, MA). The bone was loaded to 400 N in compression, as the screws of the fixture were tightened to reduce compliance within the fixture (Figure 20a). The bones were then cyclically pre-conditioned between 50 N and 1000 N for 15 cycles.

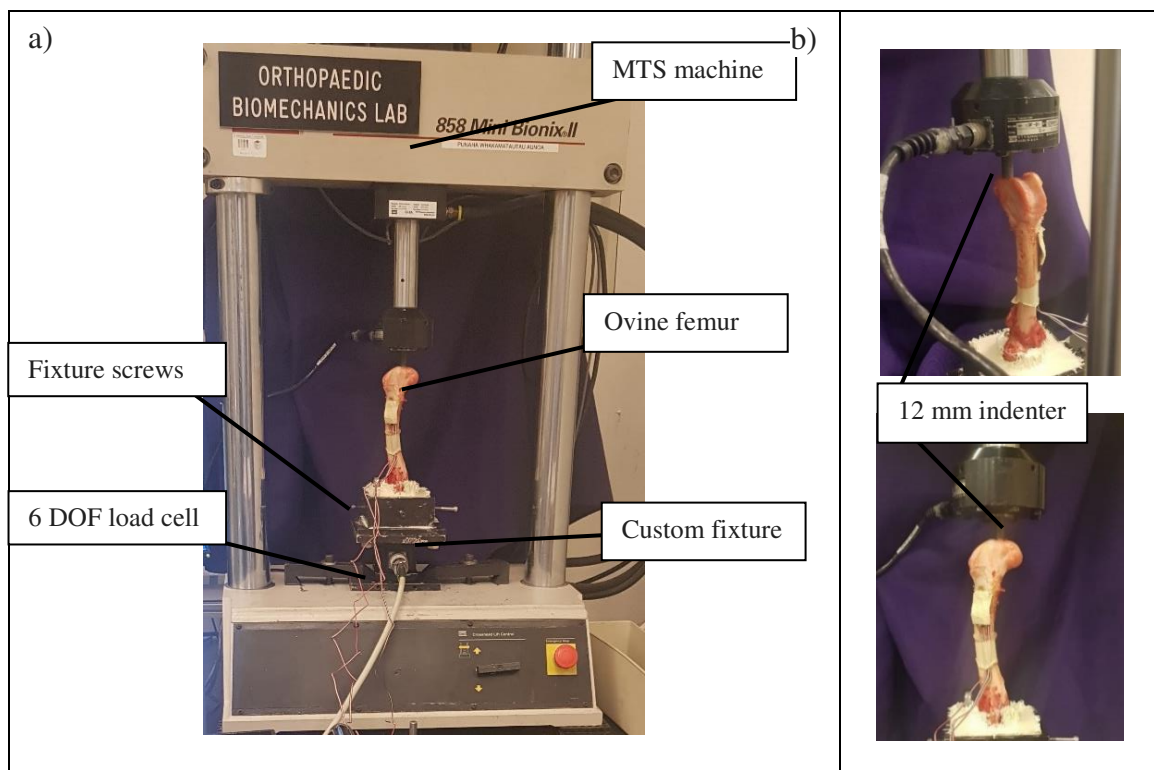


Figure 20: (a) Digital image of an ovine femur fixed into the MTS machine using a custom made fixture (b) two views of the femur in the fixture illustrating where the indenter is aligned.

3.7 Model Validation

3.7.1 Bone Surface Strain Validation

To validate the FEA femur model, comparison between the bench-top and FE model data were performed. The femur only FEA model was simulated with no fracture region (intact), with the same boundary conditions as described in section 3.4.3 (Figure 21). Strain gages were attached to four regions of interest on the ovine cadaveric bones. Gages were placed where strain predictions were also probed from the model, allowing a one-to-one comparison of bone strain between bench-top and FE experiments (Figure 21). Strain from the FE model was determined by selecting a group of surface nodes matching the regions where the strain gages were attached on the surface of the bone in the bench-top experiments (Figure 21). Areas with relatively high strain magnitudes were selected to ensure high sensing fidelity.

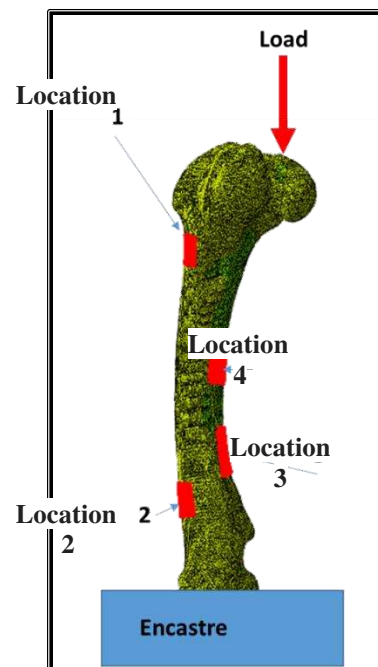


Figure 21: The Femoral model and the 4 regions where strain data were probed to compare and validate with tabletop results.

3.7.1.1 Experimental Setup for Strain Gage Testing on Bone

A set of bench-top cadaveric experiments were conducted and the axial strains were measured for each strain gage for six (n=6) specimens. To measure bone surface strains, 4 strain rosettes (MMF313009, Micro-Measurements, Raleigh, NC) were attached to the ovine femur samples (Figure 22). The gages were applied using standard strain gage application techniques [121]. The gages were then covered in a thermoplastic adhesive (Gorilla HMA, ad-tech, Hampton, NH) to protect the gages and connected to a data acquisition (DAQ) system (NI cDAQ-9178, National Instruments, Austin, Texas). These data were obtained via a custom written LabVIEW code (2016, National Instruments, Austin, Texas). The bones were then tested as described in section 3.6.

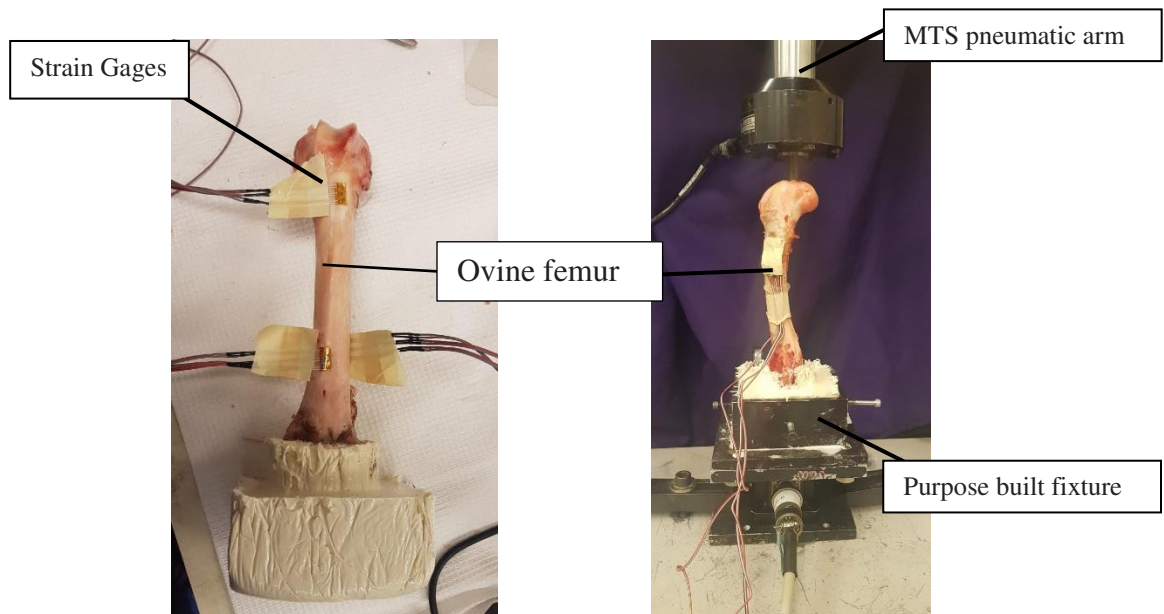


Figure 22: Left: An image showing strain gages attached to the surface of a prepare Femur specimen. Right: A strain gage test specimen put into compression in the mechanical testing machine via a 12mm indenter on the medial condyle

3.7.1.2 Bone Surface Strain Gage Experimental Protocol

Once the strain gaged bone was preconditioned, the sample was unloaded and both load cells and the strain gages were zeroed. Saline was continuously applied to keep the specimen hydrated. The samples were cycled between 50 N and 700 N in compression for 5 cycles (at a loading rate of 50 N/sec in load control with a 10 second pause at max load). Axial strain and axial compression (N) data were collected via a custom-written code in LabVIEW. Some tests on fully fractured samples were observed to fully reduce the osteotomy before the 700 N load was reached. To ensure consistency between all tests, a linear fit of axial strain vs axial load was obtained for each recorded axial strain and the linear fitted equation was used to extrapolate the strain at 700 N in these cases (Figure 23). Extrapolating bench-top data also provided an average strain gradient for the 5 compression cycles. The strains between the bench-top experiments could then be compared to the strain predictions probed from the model in the identified regions of interest (Figure 21).

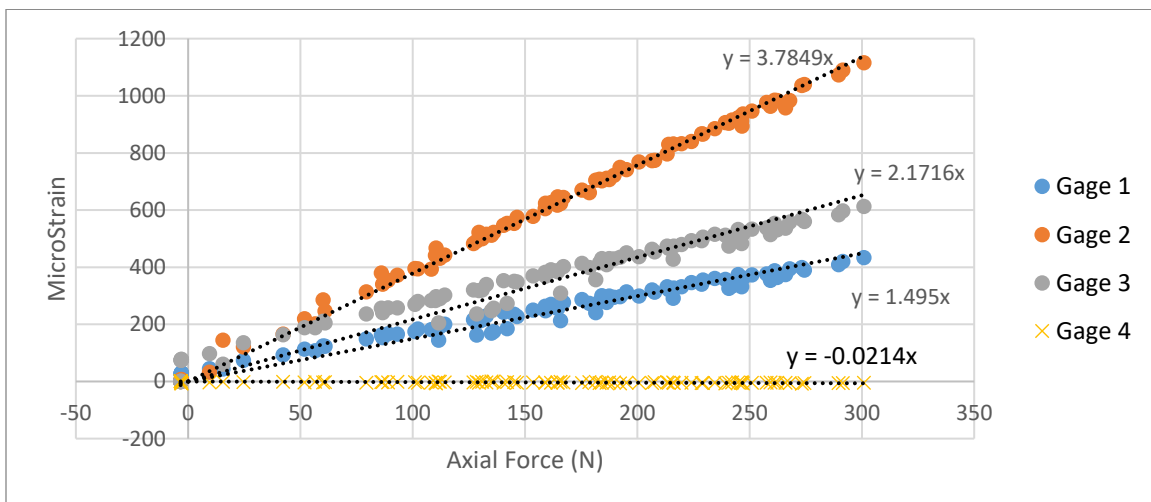


Figure 23: An example figure of the 4 strain gage location measurements of a fully osteotomized femur fixed with the thin plate as the medial condyle is loaded. The loading was stopped at 300N as the fracture gao would completely reduce if the load was taken to 700N and the equations of the linear fits forced through zero were found. These equations were used to extrapolate what the strain would be at 700 N.

3.7.2 Plated Study Validation

To additionally validate that the model was accurately predicting strains, a set of plate strain gage experiments were conducted *ex vivo* using ovine cadaveric femurs. FE models for all three plate thicknesses were simulated with all callus modulus properties (a total of 10 moduli within the range between 100 Pa – 10 GPa) utilizing the boundary conditions described in section 3.4.6. Strain predictions were then probed for all models from the indented gage location regions of the plate indicated in Figure 24.

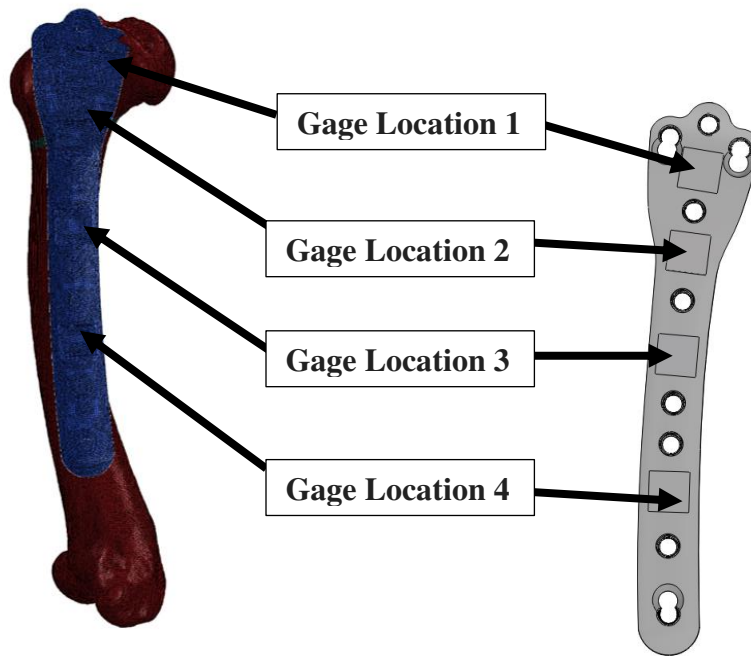


Figure 24: The numbering used for all plate strain analysis and predictions illustrated on a 3d surface model (right) and an FEA plate model (left).

3.7.2.1 Plated Study Experimental Setup

For the bench-top validation experiment of the plated femur model, one plate of each thickness (4.6 mm, 3.8 mm, and 3.2 mm) was fitted with 4 strain gage rosettes (MMF313009,

Micro-Measurements, USA; Figure 25 a & b). The rosettes were attached using standard strain gage application techniques with cyanoacrylate [121] in the regions indicated in Figure 24. Gages were coated in a thermoplastic adhesive to protect them from accidental damage. Only right femurs were used for the plate study as the plates were manufactured unilaterally for the right hind limbs. The bones were potted with the technique described in section 3.6 and attached to the lateral side of the proximal end of the femur using five 5.0mm diameter, 42 mm length screws, and four 5.0 mm diameter, 30 mm length screws (Veterinary Orthopaedic Implants, St. Augustine, FL; Figure 25c). The screw lengths were selected based on the depth required to engage both cortices, which was confirmed via visual inspection and radiographic imaging (Figure 25d). Once the bone plate was securely attached to the femur, the strain gages were attached to the DAQ and the bone-plate construct was placed in the MTS fixture, as described in section 3.6.

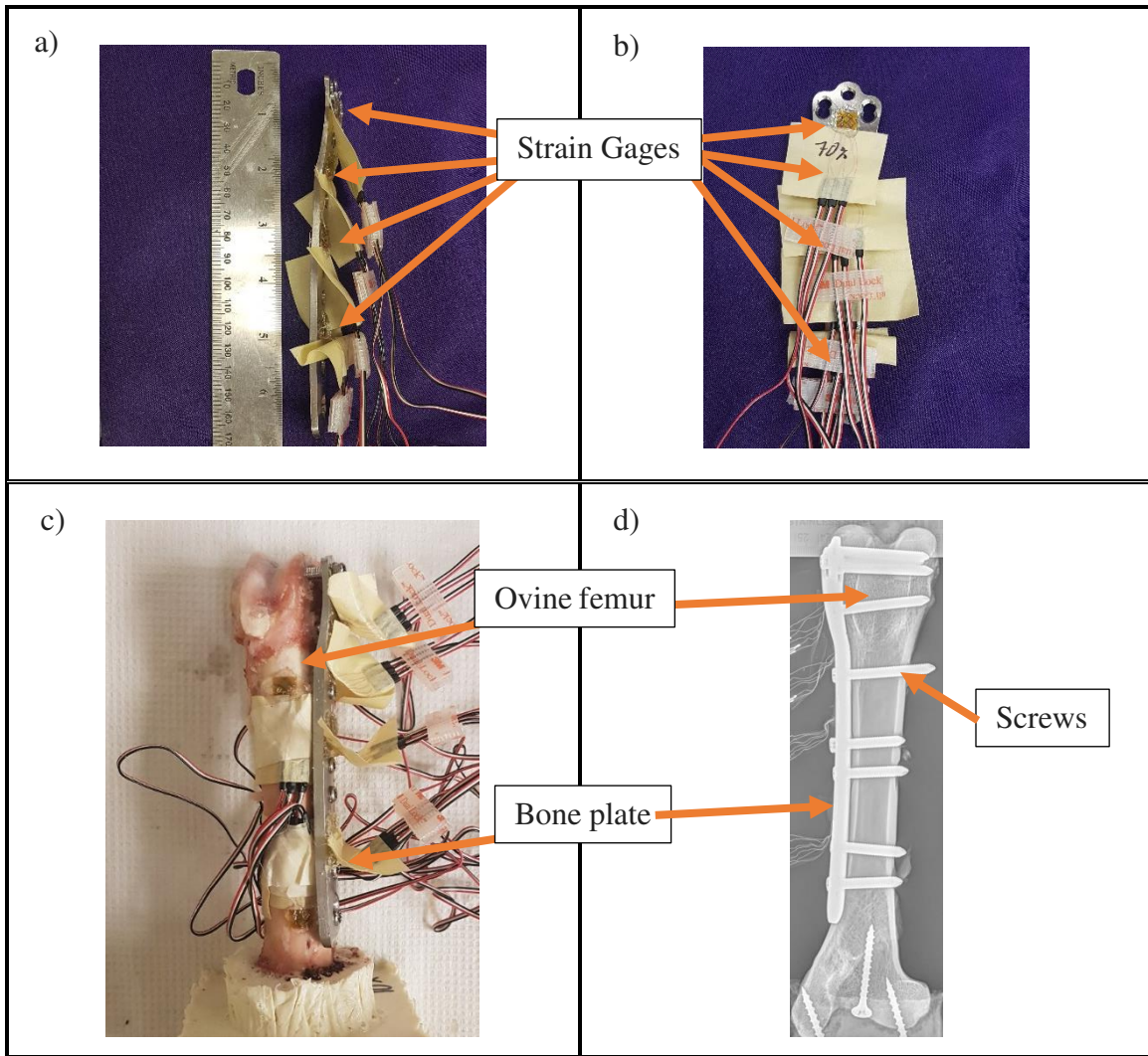


Figure 25: (a) side view of a 3.2 mm thick plate with 4 strain rosettes attached. (b) front view of a 3.2 mm thick plate with 4 strain rosettes attached. (c) An intact ovine right femur plated with a 4.6mm thick plate (d) A radiograph of the plated ovine femur showing the screws bicortical engagement. (Note: The epiphysis screws were checked visually for protrusion through the lateral cortical bone).

3.7.2.2 Bench-Top Fracture Simulation

To simulate the healing cascade of a supracondylar fracture, a reduction osteotomy model was used for the bench-top experiments. In this model, an osteotomy was cut through the bone thickness at varying depths using an oscillating saw. Four distinct levels of the healing cascade

were simulated by cutting from the medial side of the bone towards the lateral cortex in an effort to reduce the mechanical stability at the simulated fracture site. The initial case (i.e., no osteotomy) was considered representative of an intact healthy bone. The first cut was performed through approximately half the thickness of the bone (half osteotomy - HO), the second cut was made approximately through three quarters of the thickness of the bone (three quarters osteotomy - TQO) and the final cut was through the entire thickness (full osteotomy - FO). An example of the bone removal cascade is shown in Figure 26.

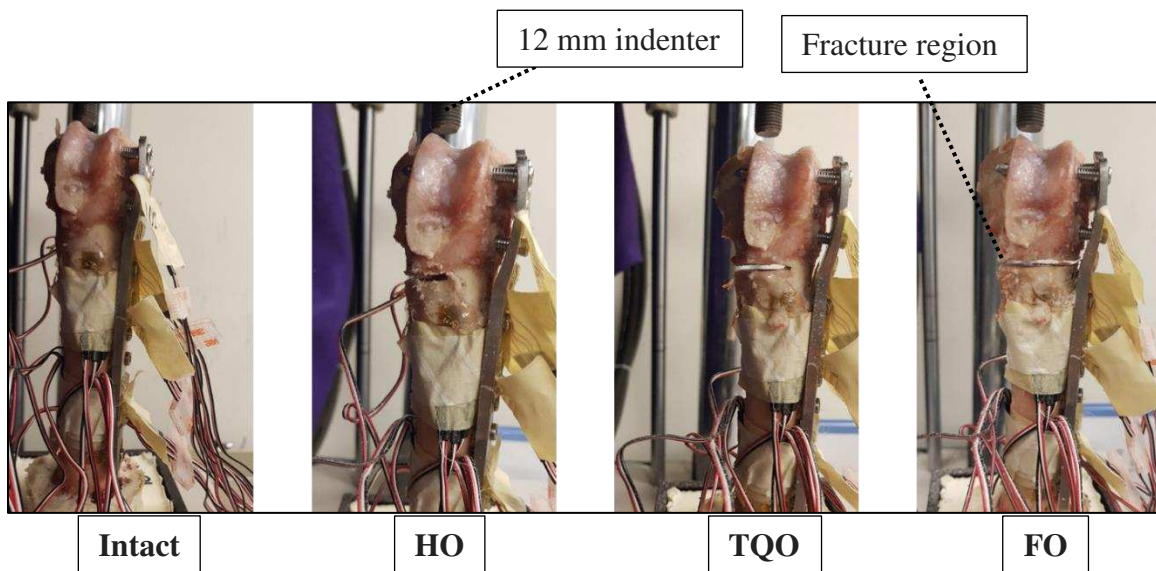


Figure 26: Model healing cascade discrete levels from left to right: Intact, Half osteotomy (HO), three-quarter osteotomy (TQO), full osteotomy (FO).

These osteotomies resulted in a 3 mm transection through the epiphysis-metaphysis region, directly behind the second most distal gage on the plate. This fracture location was chosen in an attempt to mimic the fractured region shown in Figure 16.

3.7.2.3 Plated Study Loading Protocol

At each osteotomy level, the same loading protocol was performed and the axial strain and load measurements were recorded. For the full osteotomy level, the bone was loaded until 700 N was reached or the fracture gap was fully reduced. Samples (i.e., plated femurs) were loaded in compression via a 12 mm indenter on the same region of the medial condyle cyclically between 50 N and 700 N five times (at a loading rate of 50 N/sec in load control with a 10 second dwell period at the maximum load), while axial strain and load measurements were recorded at 2 Hz, giving approximately 60 data points per cycle (180-300 datum points per test). For each plate (n=3) experiment, replicate procedures were carried out on seven to eight (n=7-8) bones to ensure the data were representative of expected supracondylar fracture mechanics. A total of 22 plate experiments were conducted (3 plates, 7-8 samples per plate). A linear fit was made to each recorded axial strain data set for each level of osteotomy, and the line equation was extrapolated to 700 N to correlate to the FE models strains. This extrapolation was done in order to determine the average measurement for exactly 700 N, allowing for comparison for some FO models that completely reduced under loading prior to reaching 700 N.

4. Model Predicted Callus Micro-Mechanics

Once the plated supracondylar fracture FE models were validated, callus mechanical behavior was investigated in an effort to understand callus strain and hydrostatic pressure as a function of plate stiffness. Callus elements were probed for principal strains and hydrostatic pressures in four different regions labelled with respect to their proximity to the plate attachment site. These regions were Anterior-Medial (AM), Posterior-Medial (PM), Posterior-Lateral (PL), and Anterior-Lateral (AL; Figure 27)

Predictions of hydrostatic pressure and maximum and minimum principal strain from the model were recorded from each region, for each plate thickness, at 700 N, 500 N, and 300 N of axial loading, and with callus properties of 1 kPa, 10 kPa, and 100 kPa. To acquire the data, a group of nodes (regions ranged between 190 and 300 nodes) were selected within each region (Figure 27), and probed for hydrostatic pressure and principal strain components. These data were averaged to get a representative measure of strain and pressure within each region.

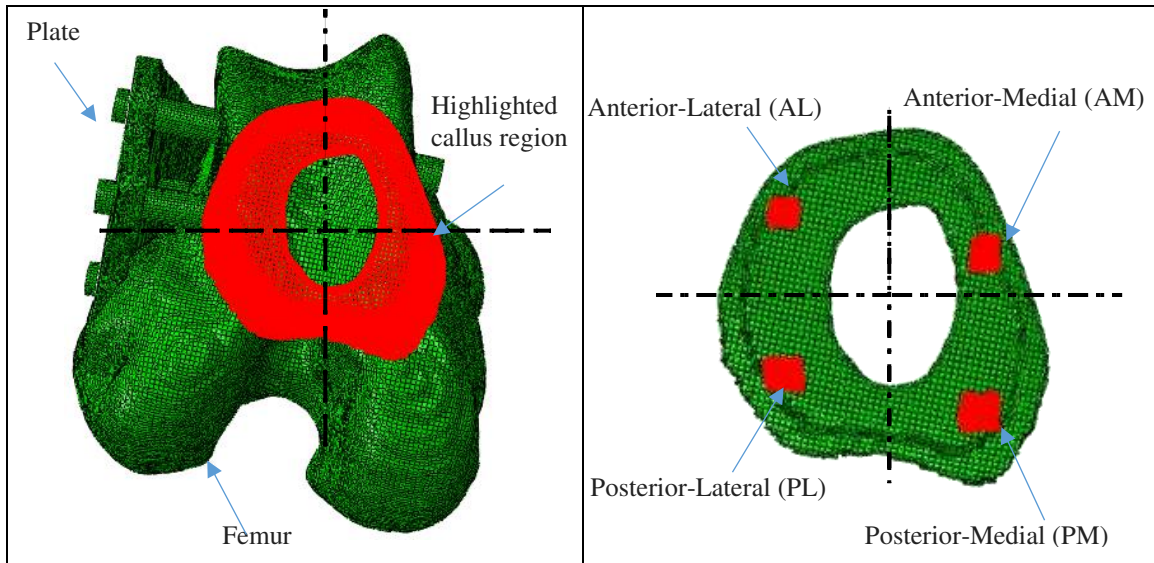


Figure 27: *Left: A proximal view of the bone with the callus highlighted. Right: the Isolated callus elements directly transposed to show the regions that it was separated into.*

By comparing strain and pressure predictions to published envelopes of tissue differentiation, as established by Claes and Heigele [59], it was theorized that it would be possible to predict the relationship between plate stiffness and expected healing outcome. For successful bony union, a mix of intramembranous and endochondral ossification is required. For that reason, the envelopes reported by Claes and Heigele for intramembranous and endochondral ossification [59] were compared to the model predictions. Predictions that fell within the strain/pressure limits of both types of ossification (i.e., intramembranous and endochondral) were theorized to accommodate acceptable fracture healing. Endochondral ossification is the most common type of healing present in secondary healing and so predictions that theoretically accommodated more endochondral ossification were favored. Predictions of strains/pressures outside of the reported envelopes were assumed to not cause bony healing and were theorized to produce unsatisfactory healing.

5. Results

5.1 Mesh Convergence on Plate Models

Results from the mesh convergence study on the plates are shown in Figure 28-Figure 30. In these figures, strain energy density is shown as a function of mesh element number at each gage location, with each strain datum point normalized to the strain magnitude at the highest mesh density. The numbering of strain regions/gages used for the reporting of results are given in Figure 16.

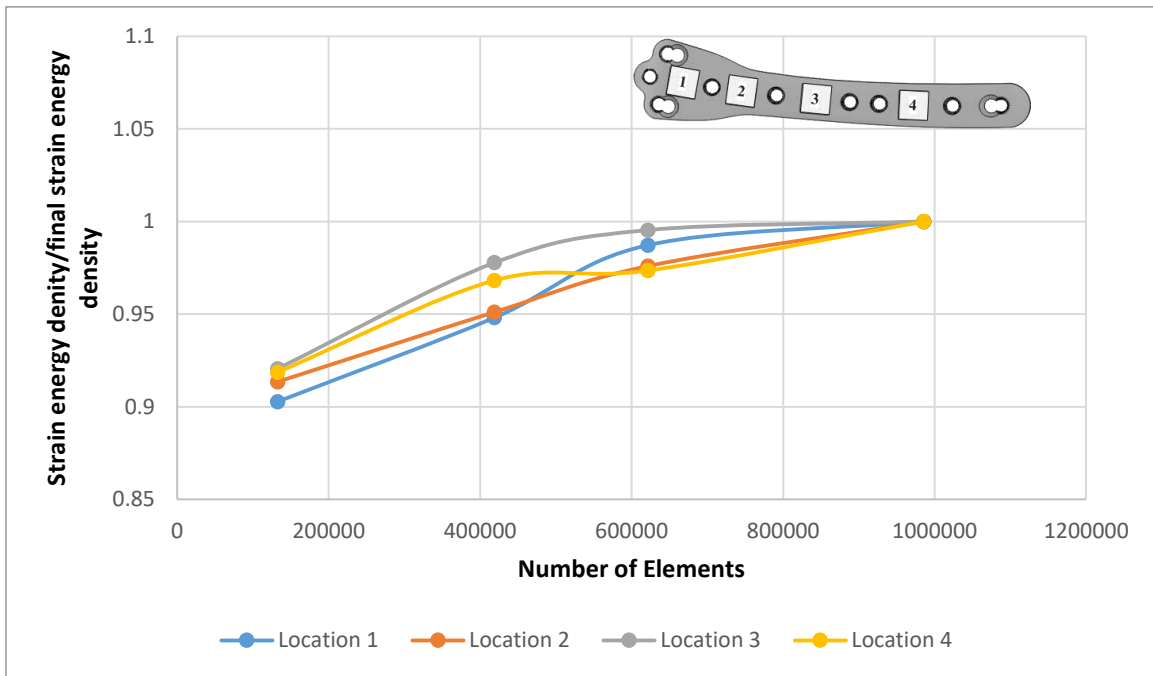


Figure 28: Thick plate convergence of strain energy density as the number of elements is increased for 4 regions indicated in the plate image.

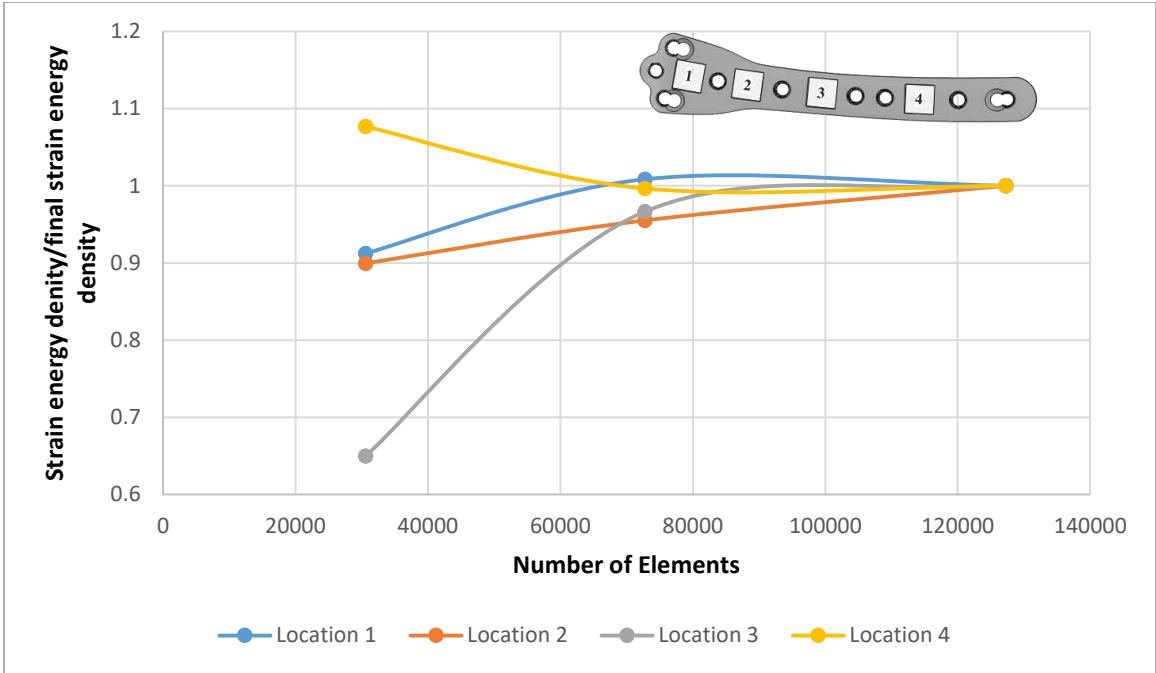


Figure 29: Middle plate convergence of strain energy density as the number of elements is increased for 4 regions indicated in the plate image.

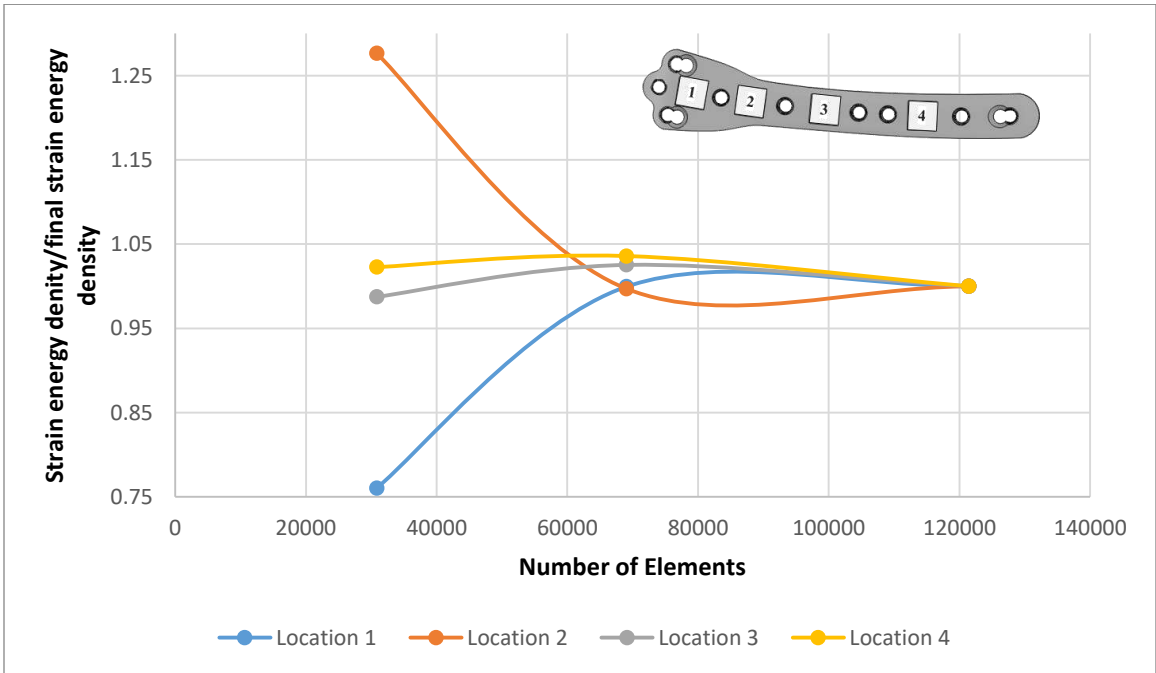


Figure 30: Thin plate convergence of strain energy density as the number of elements is increased for 4 regions indicated in the plate image.

For the thick (4.8 mm) plate, the strain predictions for all probed regions changed by less than 2%, with an increase in elements from 418,871 elements to 621,275 elements (48% increase in element density). For the middle thickness (3.6 mm) plate, the strain predictions for all probed regions changed by less than 4% with an increase in elements from 72,758 elements to 127,263 elements (75% increase in element density). For the thin (3.2 mm) plate, the strain predictions for all probed regions changed by less than 5% with an increase in elements from 69,034 elements to 121,424 (76% increase in element density) elements. The data indicated that very small percent changes in the predicted strains were observed with increased mesh density; thus, the models were considered converged. Specifically, mesh densities of approximately 65.7 elements per cubic mm, 82.2 elements per cubic mm, and 45.6 elements per cubic mm for the thick, middle and thin plates respectively, were used for each respective plate model. These converged plate meshes were used for all subsequent simulations.

5.2 Strain Vector Analyses - Cylindrical Model and Single Element

The stress and strain vector analysis of the simplified cylindrical tube model showed that the maximum principal stresses were aligned longitudinally (with the tensile/compressive loads). The maximum principal strains were aligned orthogonally and obliquely from the surface of the cylinder (Figure 31). These strain predictions, which the FEA software (i.e., ABAQUS) typically provides as the principal strains, cannot be fully quantified by 2-dimensional rosettes, as these out-of-plane strain components are out of the gages' measurement plane.

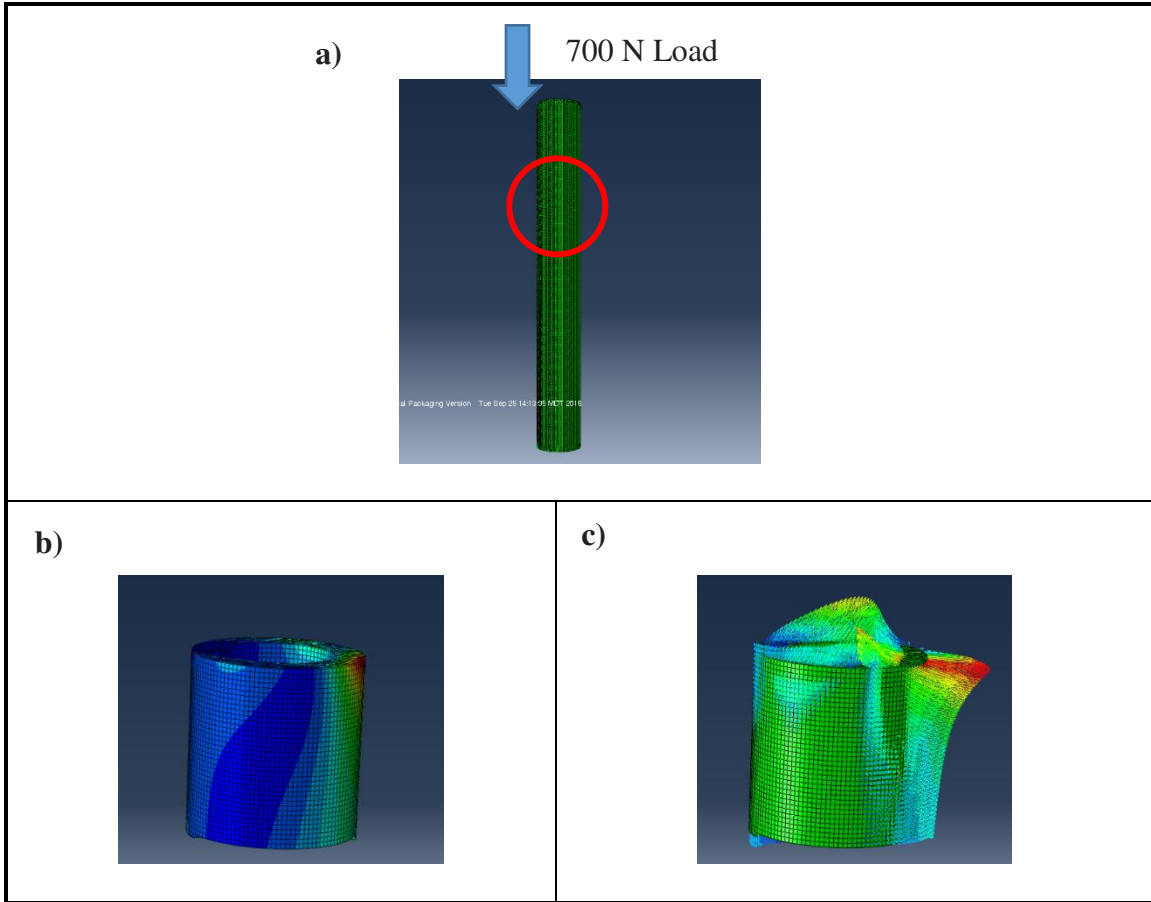


Figure 31: (a) A cylinder FEA model with ovine cortical bone properties under a 700 N point load, similar to the femoral model. Circled in red is the region that results were calculated for. (b) This image shows the stress profile in an isolated section of the tube (c) This image shows the same section with principal strain vectors graphically represented, demonstrating the out-of-plane principal strain vectors.

Additionally, principal strain vectors were found analytically and plotted on a representative 3D element (Figure 32a). Figure 32b shows the principal strain components (maximum, minimum, and middle) found through empirical methods. The empirically calculated principal strain components demonstrated the FEA's out of plane strain predictions were accurate and not modeling error.

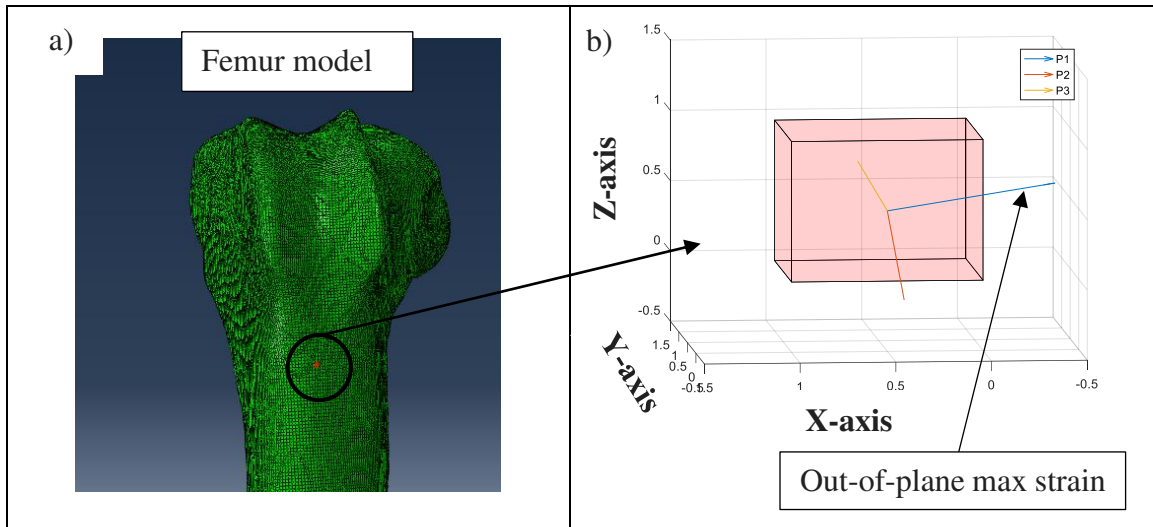


Figure 32: (a) An image of the distal femoral head in the FEA model. Encircled and highlighted in red is the single element in the regions of interest probed for empirical analysis. Right: A single representative element showing the 3 principal strains and their directions. The largest magnitude strain is P1 which is inprotrudig down the y-axis

These results showed that a large component of the principal strains were predicted to be out-of-plane to the bone's surface. These out-of-plane strain components would be immeasurable by 2 dimensional planar strain rosettes, and thus, it was determined that axial strain predictions were more appropriate to compare. Axial strain data (i.e., aligned along the longitudinal axis of the bone) were used for all subsequent modeling and bench-top comparisons.

5.3 FE Model Validation

5.3.1 Bone Surface Strain Validation

Bench-top and FEA predicted axial strain results are shown in Figure 33. Experimental data means (n=6 samples) are shown with standard deviation bars.

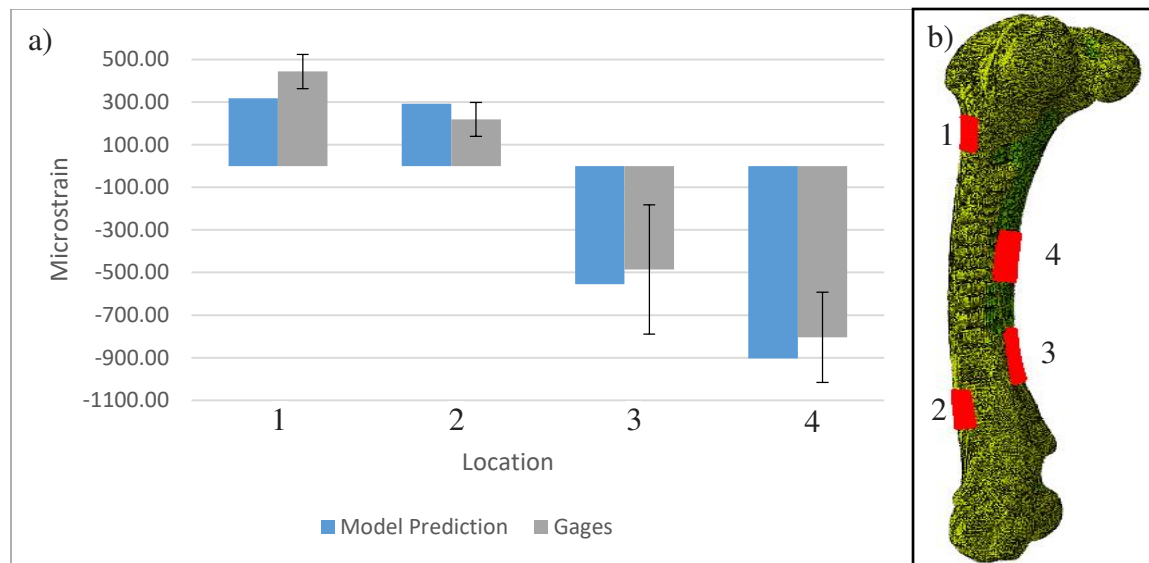


Figure 33: Strain magnitudes predicted by the model (blue) and found experimentally (grey) for the four regions of interest (b) identified in red on the femoral model surface is the regions of interest where gages were attached and where model predictions were probed.

The FEA model of the ovine femur was able to predict the axial surfaces strain at Location 2, Location 3, and Location 4 within one standard deviation of the bench-top data. Location 1 was predicted least accurately, but was still within 1.6 standard deviations of the bench-top data (Figure 33a).

The geometry of the scanned ovine femur used to generate the FE model was considered to be representative of ovine femur bones and within the range of the bones tested *ex vivo*. However, small differences in cortical wall thickness or general geometry could have caused the decreased model prediction accuracy observed in Location 1. Locations 4 and 3 had the largest magnitude strains, both measured and published by the FE models. This was expected as these location were the furthest from the boundary conditions (i.e., the potted end and the loaded condyle), and thus, experienced the largest applied moments. As regional strains captured by the model predictions

generally agreed with bench-top data, it was assumed that the ovine femoral FE model was able to predict surface bone strains accurately.

5.3.2 Plate Strain Study Model Predictions Over a Simulated Healing Cascade

The predictions of axial strain in the four gage locations on the plate, as a function of changing the callus' elastic modulus, are shown in Figure 34 - Figure 36, for the 4.8 mm, 3.8 mm, and, 3.2 mm plate thicknesses, respectively. The region of interest (ROI) location numbering scheme used is illustrated in Figure 24. When the strain was no longer significantly affected by altering callus stiffness at each extreme (i.e., when strain was no longer affected by increasing or decreasing callus stiffness), an association was made to the fully healed or fully fractured equivalent cases. The data indicated that strain magnitude on the plate was no longer significantly changed when callus stiffness was increased over 1 GPa or decreased below 1 kPa. It was determined that these callus elastic moduli (i.e., 1GPa and 1kPa) were analogous to intact healthy bone and an acute hematoma at the fracture site, respectively.

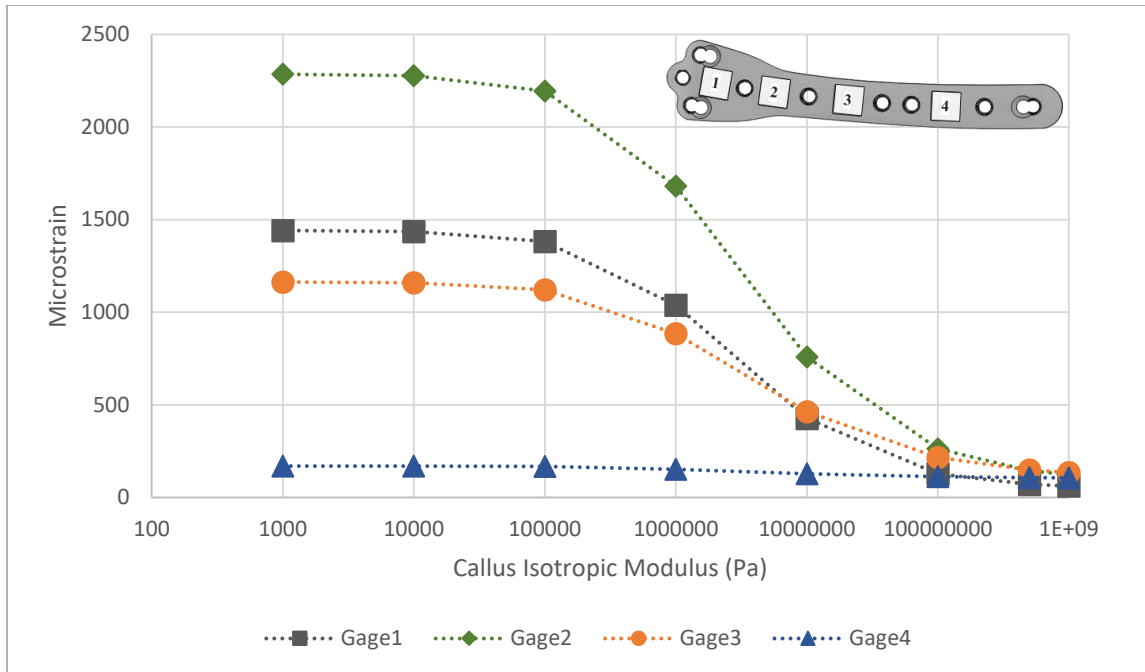


Figure 34: Thick (4.6 mm) plate log-x plot of strain predictions over an increasing callus modulus, simulating a healing cascade. The numbering of each gage corresponds to the numbering on the plate illustration.

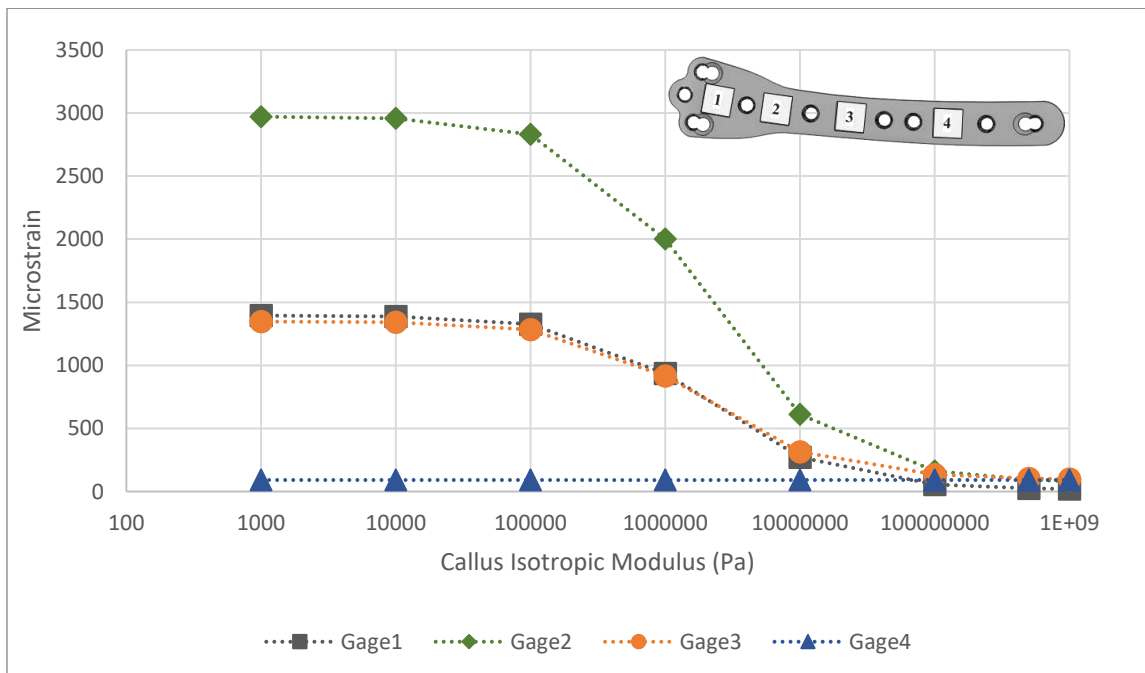


Figure 35: Middle (3.8 mm) plate log-x plot of strain predictions over an increasing callus modulus, simulating a healing cascade. The numbering of each gage corresponds to the numbering on the plate illustration.

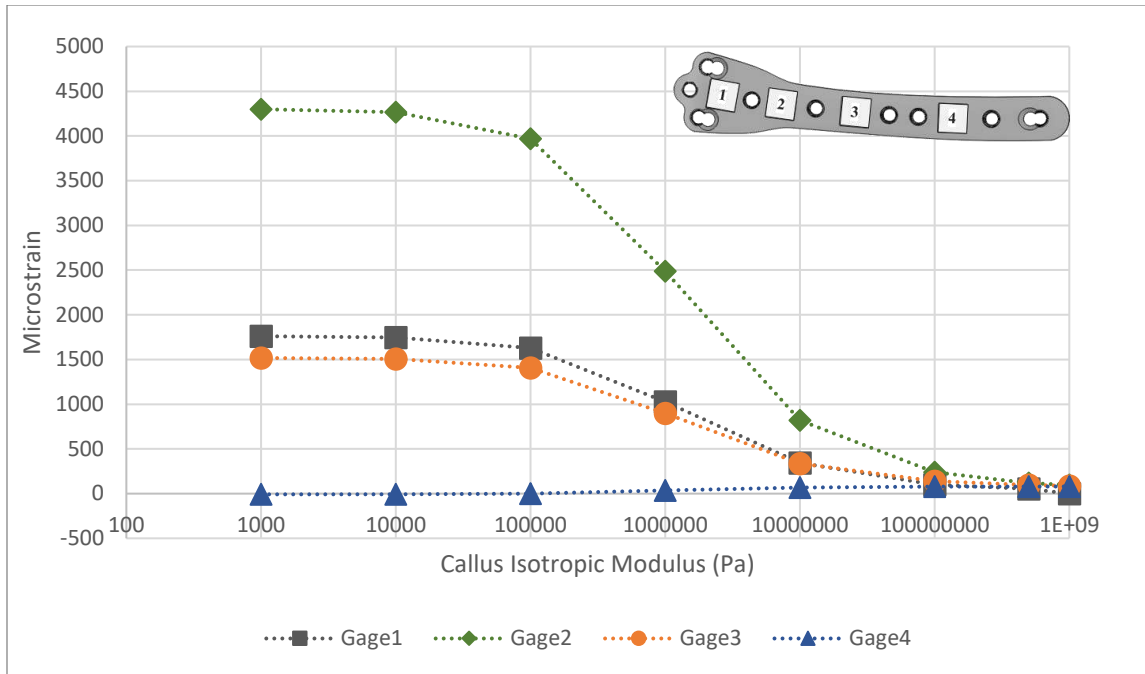


Figure 36: Thin (3.2 mm) plate log-x plot of strain predictions over an increasing callus modulus, simulating a healing cascades. The numbering of each gage corresponds to the numbering on the plate illustration.

For all plate thicknesses, Locations 1, 2 and 3 showed decreases in axial strain as the callus elastic modulus was increased (Figure 34 - Figure 36). This was expected as the applied load was borne more by the bone as the callus became stiffer. Location 2 was predicted to have the highest maximum strain for all 3 plate thicknesses (Figure 34 - Figure 36). The fracture was located approximately perpendicular to Location 2, with Locations 1 and 3 at similar distances distally and proximal to the fracture, respectively. Due to Locations 2's proximity to the fracture (i.e., this location spans the unsupported length of the fracture), these high strain predictions are expected. Also for all plate thicknesses, Locations 1 and 3 were predicted to have similar maximum axial strains (Figure 34 - Figure 36). The biggest difference in strain predictions between Locations 1 and 3 was seen in the thick plate model where Location 3 predicted a 19.3% lower strain magnitude than Location 1 (1441 microstrain for Location 1 vs 1163 microstrain for Location 3; Figure 34).

Location 4 never predicted more than 172 microstrain in magnitude (1kPa for the thick plate) and was relatively unaffected by callus stiffness (maximum strain ranged from 106 to 170 microstrain over the entire range of callus stiffnesses). Location 4 was predicted to have a small, but purely tensile, axial strain for the thick and middle thickness plates. At Location 4, slight compressive (-8.0 microstrain) strains were predicted at very low callus properties for the thin plate. This finding was not unexpected, as this gage location was the furthest ROI from the fracture site, with 4 screws separating it from the fracture site. For the 3.6 mm (middle) and 3.2 mm (thin) plates, strains were predicted to be slightly increased for Location 4 as the callus modulus increased (Figure 35 and Figure 36). For the thin plate, gage 4 was predicted to have negative (compressive) strain for the lowest callus modulus (Figure 36).

When comparing the maximum predicted strains for each plate, gage 4 data were omitted as it was the least affected by the fracture region's material properties. Therefore, the average reduction in predicted strain for Locations 1, 2, and 3 were compared.

From the thick (4.6 mm) plate to middle (3.8 mm) plate, the average reduction in construct stiffness over the 3 ROI locations was calculated to be 11.1%, with a maximum reduction of axial strain of 23.1% for Location 2 (Figure 34 and Figure 35). From the thick (4.6 mm) plate to the thin (3.2 mm) plate, the average reduction in construct stiffness was calculated to be 29.4%, with a maximum reduction of axial strain of 46.9% for Location 2 (Figure 34 and Figure 36). The design goals were a reduction in stiffness of 15% from thick plate to middle plate and 34% for thick plate to thin. The average reduction in predicted relative stiffnesses for both the middle (3.8 mm)

thickness plate and the thin (3.2 mm) plate were within 5% (3.9% and 4.6% differences, respectively) of the design targets.

5.3.3 Bench-Top Plated Femoral Fracture Models' Strain Measurements

Figure 37 - Figure 39 show the mean results of the bench-top measured axial strains for the 4.6 mm, 3.8 mm and 3.2 mm thick plates, respectively. The error bars show the experimental standard deviations. These figures show the axial strain measured as the osteotomy level was increased from intact, to half osteotomy (HO), to three-quarter osteotomy (TQO) and finally to full osteotomy (FO) as illustrated in Figure 26. The gage numbering is shown in Figure 24 and illustrated in the top right of Figure 37 - Figure 39.

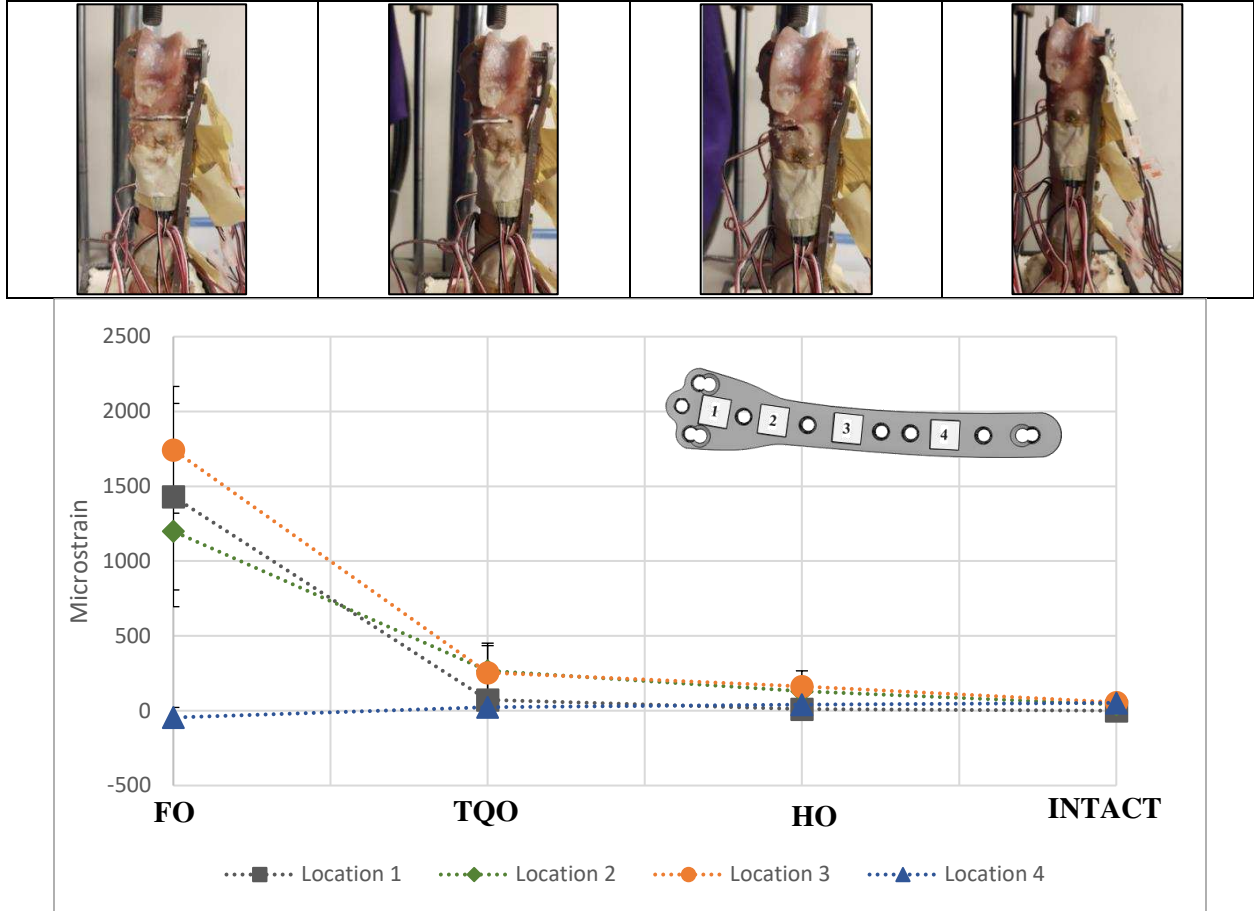


Figure 37: Average strain measurements ($n=7$) for the 4.6 mm thick plate over the reverse fracture model implemented via progressive tabletop transection of the fracture region (Intact, to half osteotomy (HO), to three-quarter osteotomy (TQO) and finally to full osteotomy (FO)). The numbering of each gage location corresponds to the numbering on the plate illustration. Error bars show the experimental standard deviations. The images above the figure shows the progressive fracture model levels (FO – intact).

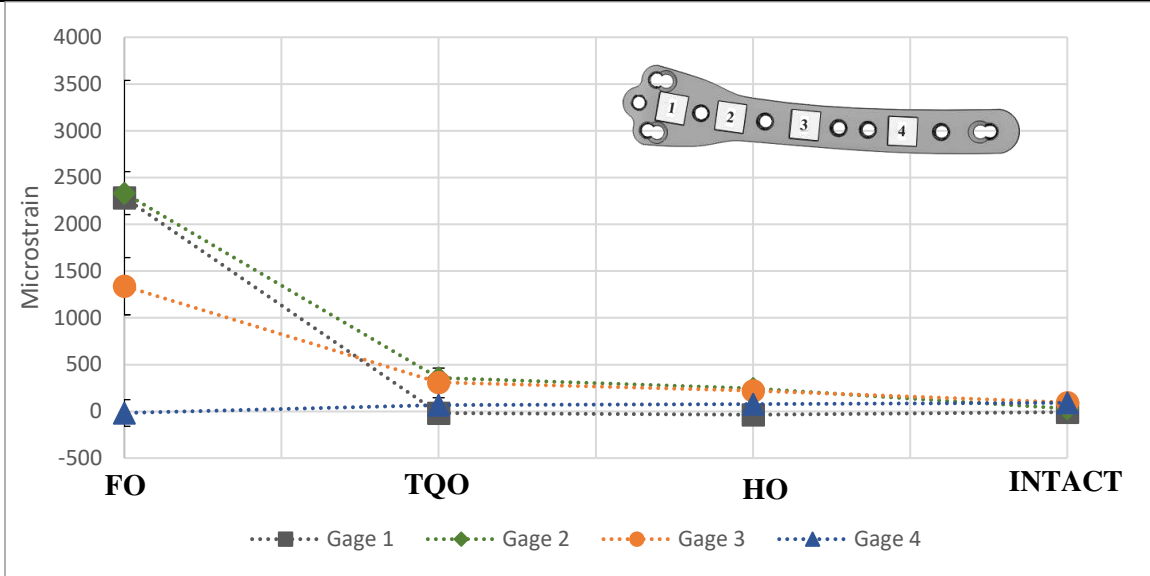
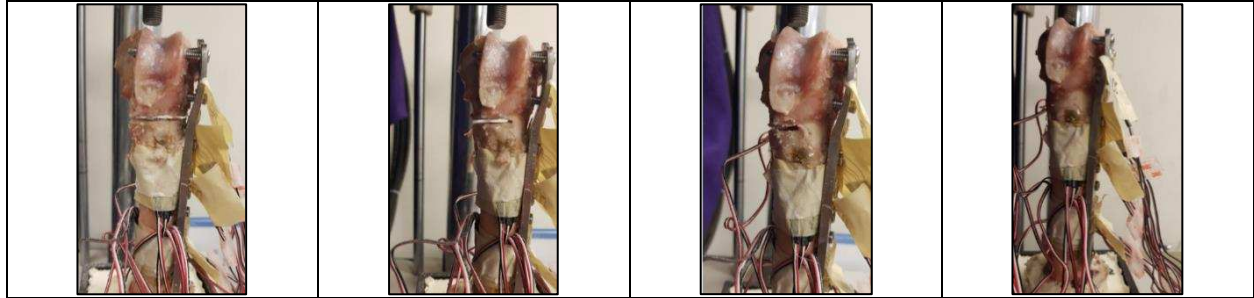


Figure 38: Average strain measurements ($n=7$) for the 3.8 mm thick plate over the reverse fracture model implemented via progressive tabletop transection of the fracture region (Intact, to half osteotomy (HO), to three-quarter osteotomy (TQO) and finally to full osteotomy (FO)). The numbering of each gage location corresponds to the numbering on the plate illustration. Error bars show the experimental standard deviations. The images above the figure shows the progressive fracture model levels (FO – intact).

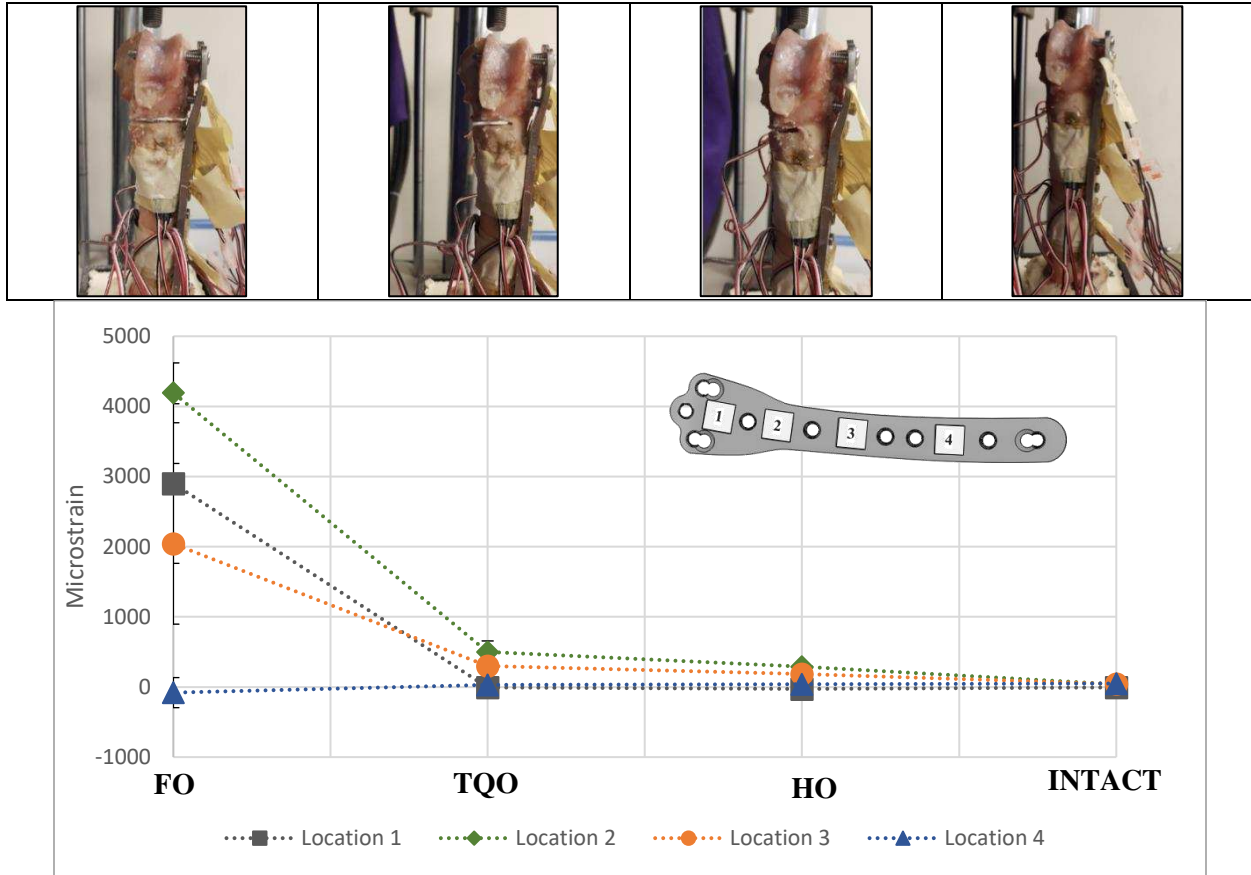


Figure 39: Average strain measurements ($n=8$) for the 3.2 mm thick plate over the reverse fracture model implemented via progressive tabletop transection of the fracture region (Intact, to half osteotomy (HO), to three-quarter osteotomy (TQO) and finally to full osteotomy (FO)). The numbering of each gage locations corresponds to the numbering on the plate illustration. Error bars show the experimental standard deviations. The images above the figure shows the progressive fracture model levels (FO – intact).

The general trend of gages 1, 2 and 3 was a decrease in strain magnitude from lowest apparent callus region stiffness (FO) to highest stiffness (Intact; Figure 37 - Figure 39). The strain at gage Locations 1 - 3 reduced during each progression of the fracture simulation model. For both the middle (3.8 mm) thickness plate and the thin (3.2 mm) plate, gage 2 had the highest measured strains (Figure 38 and Figure 39). For the thick (4.6 mm) plate, gage 2 measured an average strain lower than Locations 1 and 3 (Figure 37). Locations 1 and 3 had similar measured strain magnitudes, with the largest difference in strain being measured for the thin plate as 29.6% (2900 microstrain for Location 1 vs 2041 microstrain for Location 3; Figure 39). Locations 4 exhibited

constant and low strains for all plate thicknesses (Figure 37 - Figure 39). The behavior for the thin (3.2 mm) plate, where Location 4 measured compressive strains for the FO case and gradually transitioned into tension, was similar to what was predicted by the model (Figure 36). All gages showed simultaneous patterns of convergence in measured axial strain from FO to intact (Figure 37 - Figure 39). These general trends were similar to the predictions of the models' axial strains as a function of elastic modulus (Figure 34 - Figure 36).

5.3.1 Axial Strain Measurements vs Strain Model Predictions for the Plated Femoral Construct

The predictions for the FO bench-top model were considered a physical analogy to the FEA model with a callus property of 1 kPa and the intact bench-top model was considered a physical analogy to the FEA model with a callus property of 1 GPa. These were termed "Intact" (Intact/1 GPa) and "Fractured" (FO/1 kPa). Three quarter osteotomy and half osteotomy experimental levels were not compared to the FEA model as they did not have a defined callus stiffness that could easily and accurately be implemented *in silico*. Succintly, it was not possible to ensure the gap and distance transected for each bench-top tested limb was the same, therefore, comparing a measured callus stiffness to the model's prediction was not considered. Regardless, it was theorized that the FO and intact data would bracket the expected response of the HO and TQO fracture model levels. Figure 40 - Figure 42 show the measured strains for the intact and fractured cases.

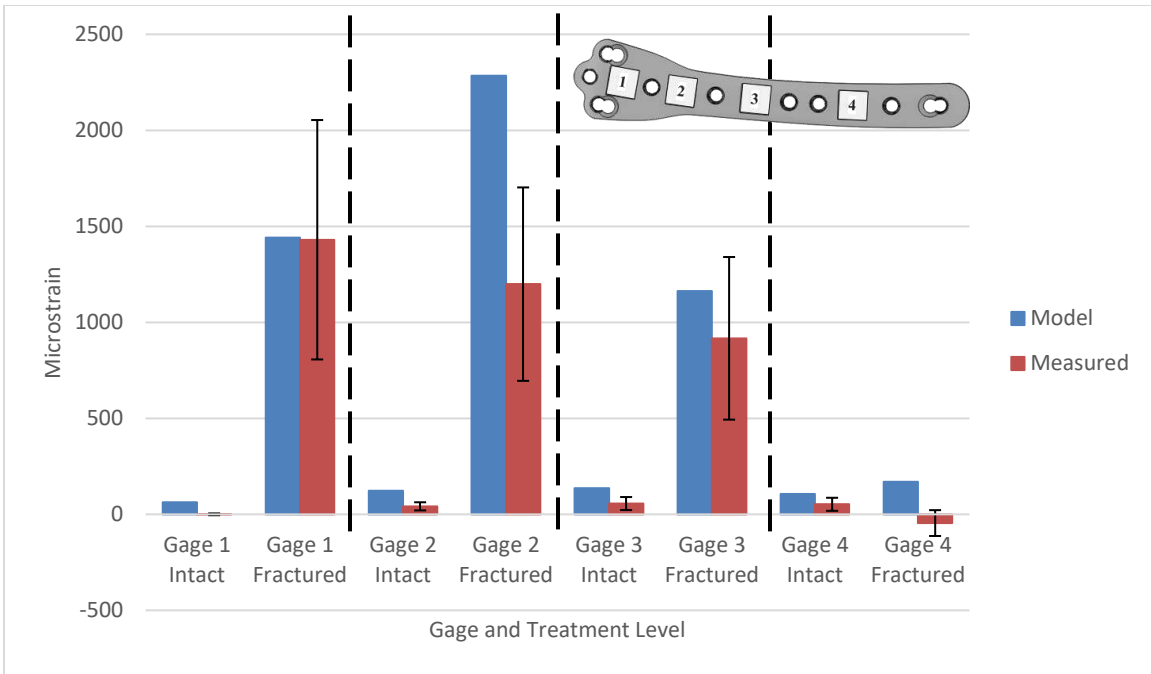


Figure 40: Thick plate measured strains and model predictions for intact and fractured cases for each gage region. The numbering of each gage corresponds to the numbering on the plate illustration. Error bars = experimental standard deviation.

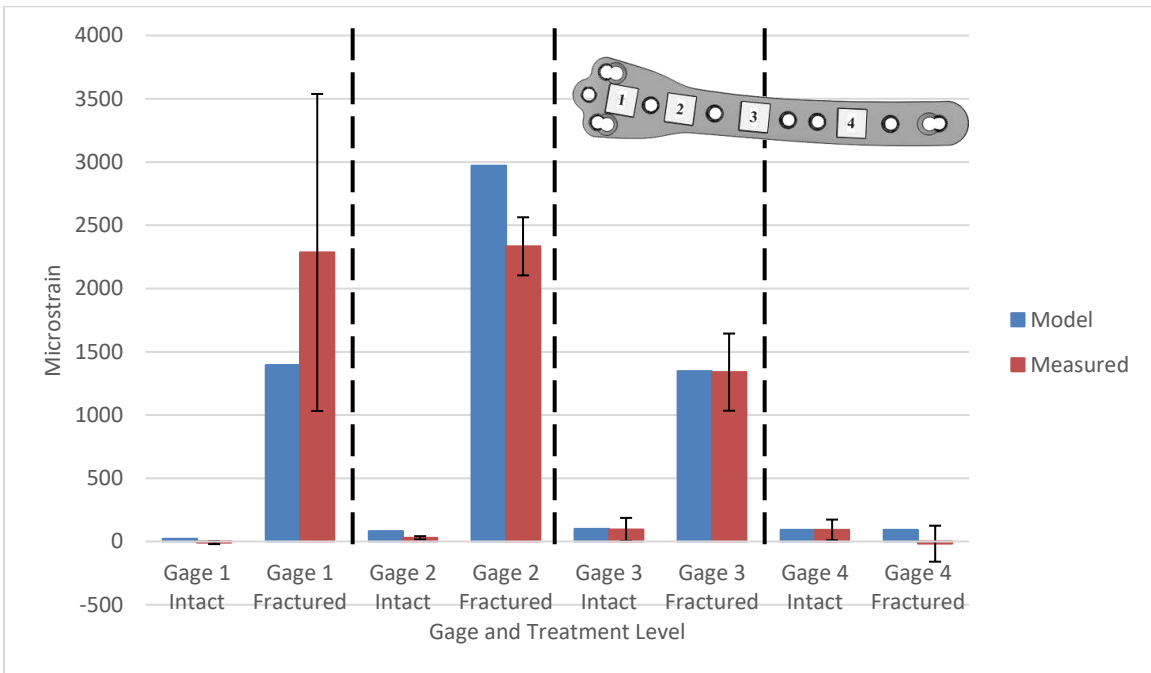


Figure 41: Middle thickness plate measured strains and model predictions for intact and fractured cases for each gage region. The numbering of each gage corresponds to the numbering on the plate illustration. Error bars = experimental standard deviation.

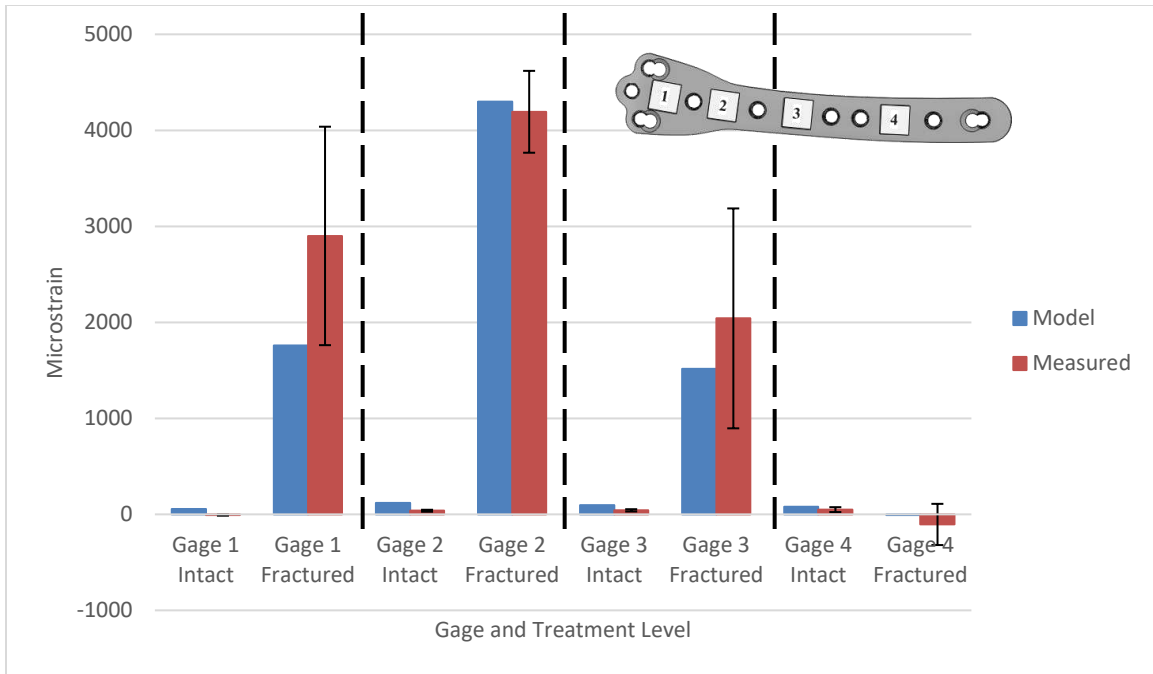


Figure 42: Thin plate measured strains and model predictions for intact and fractured cases for each gage region. The numbering of each gage corresponds to the numbering on the plate illustration. Error bars = experimental standard deviation.

The plated femoral fracture models were able to predict the axial strains for a majority of the gage locations (i.e., fell within a single standard deviation of the measured results). Table 2 shows a comparison of the measured vs. predicted axial strains for plates and locations with the number of standard deviations between the models’ predictions and measured data. The magnitude in any of the strain discrepancies are also highlighted.

Table 2: A comparison of measured vs predicted strains for all plates and all gages. “Yes” indicates the model predicted strain within a standard deviation of the measured strain. For models that did not fall within a standard deviation, the number indicates how many deviations away the prediction was and in the parenthesis is the value of microstrain different to the measured strains for reference

Gage location	Intact				Fractured			
	1	2	3	4	1	2	3	4
Thick plate	2.65 (35.81)	Yes	Yes	Yes	Yes	1.46 (182.91)	Yes	1.86 (6.459)
Middle plate	2.20 (10.51)	2.19 (21.63)	Yes	Yes	Yes	2.0 (202.83)	Yes	Yes
Thin plate	1.89 (26.68)	Yes	Yes	Yes	Yes	Yes	Yes	Yes

For the thick (4.6 mm) plate, the FEA model successfully predicted strains within a single standard deviation of the experimentally measured strains for 3 locations for the intact cases (i.e., Locations 2, 3 and 4) and 2 of the 4 fractured cases (i.e., Locations 1 and 3; Figure 40). The measured strain at Location 4 in the fractured case was slightly tensile when it was predicted to be slightly compressive in the model. The strain at Location 2 was predicted to be 1.5 standard deviations higher than the measured strain for the fractured case (Table 2).

For the middle thickness (3.8 mm) plate, the predicted axial strains fell within a single standard deviation of the experimental measured strains for Locations 3 and 4 for the intact case, and 3 of the Locations (i.e., Locations 1, 3 and 4) for the fractured case (Figure 41). The measured axial strain at Location 2 for the fractured case (FO) was predicted to be 2 standard deviations higher than the measured experimental strain (Table 2).

For the thin (3.2 mm) plate, the predicted axial strains fell within a single standard deviation of the experimental measured strains for almost all locations for both the intact and fractured cases

(Figure 42). The only exception was Location 1 (27 microstrain difference between predicted and measured axial strain) for the intact case, where the actual measured strain was slightly compressive while it was predicted to be slightly tensile (Table 2).

Despite disagreements in some strain regions between the model and bench-top measured values, the model did accurately predict plate strains in most regions. The majority (17 of 24) of the regions measured for strain were successfully predicted within one standard deviation (experimental) by their respective models. The thin plate model was considered the most reliably accurate for predicting strains, as it predicted axial strain within a standard deviation in all fractured scenarios in all measured regions. The middle thickness and thick plate were considered mostly accurate as they predicted almost all strains within a single standard deviation. They both predicted 5 of 8 regions accurately, and all fractured case differences fell below two experimental standard deviations. Thus, the FE models were deemed fully validated for the novel supracondylar fracture model for all simulated healing cascades.

5.4 Fracture Region Micro-Mechanics Predictions

The hydrostatic pressure and principal strain (maximum and minimum) predictions from the fracture region were superimposed on the mechanical requirement envelopes presented by Claes and Heigele for expected tissue differentiation (intramembranous and endochondral ossification) at a fracture site [59]. The data for the each plate thickness and all loads (300 N, 500 N, 700 N) for a callus elastic modulus of 1 kPa are shown in Figure 44, where each subplot represents a specific region of the callus (i.e., posterior-medial (PM), anterior-medial (AM), anterior-lateral (AL), posterior-lateral (PL; Figure 27)). Similar plots are shown for models with a

callus elastic modulus of 10 kPa (Figure 45) and 100 kPa (Figure 46). Figure 43 outlines the parameters (callus modulus, load, and plate thickness) for each simulation run for the fracture region micro-mechanics predictions.

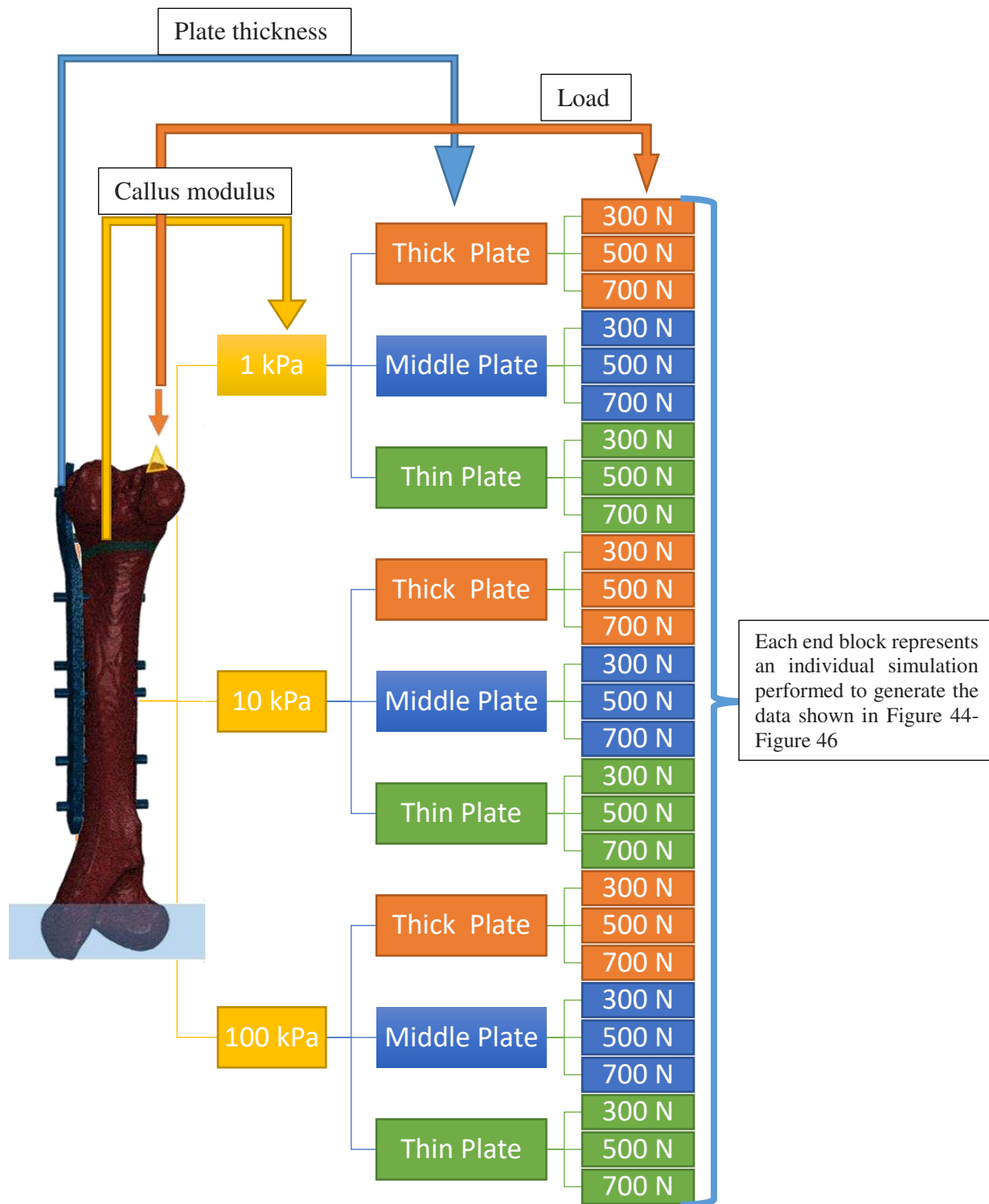


Figure 43: Parameters of each simulation run for analyses of the callus mechanical environment in a flow diagram. Cell colors for loads and plate thicknesses correlate to the plotted color for each plate thickness used in Figure 44- Figure 46.

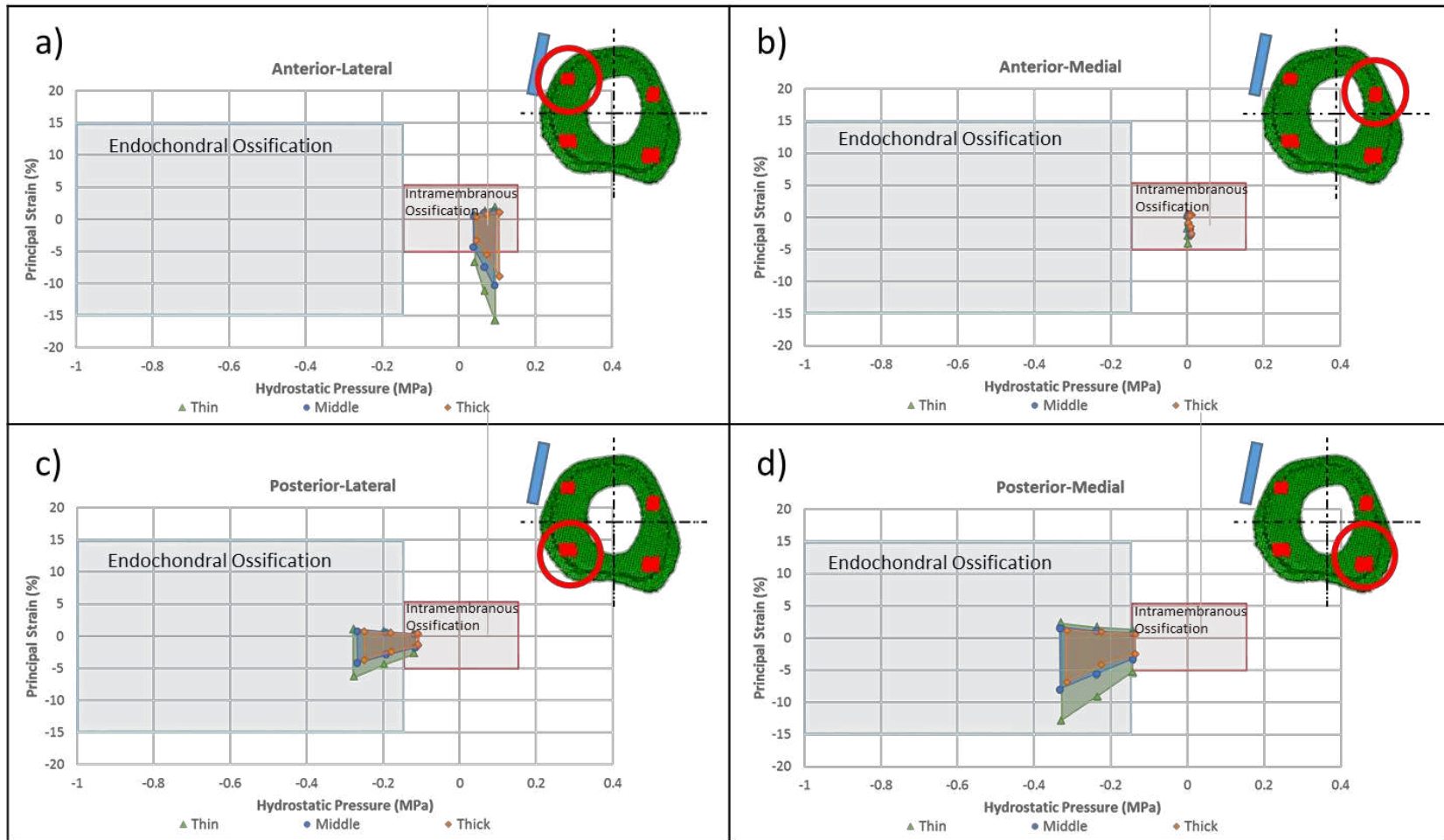


Figure 44: 1kPa - The specific hydrostatic pressures and strains envelopes found from Claes and Heigele [59] are plotted here in the shadowed regions for both endochondral ossification and intramembranous ossification. Over top of these envelopes are the predicted specific hydrostatic pressures plotted against the max and minimum principal strains in each callus region probed (AM, PM, PL, AL) over 3 loading magnitudes (300 N, 500 N, 700 N) for the 1 kPa callus modulus. An illustration of the callus regions is shown in the top right corner of each sub-plot showing the plates approximate location (blue) and the respective cells location of interest.

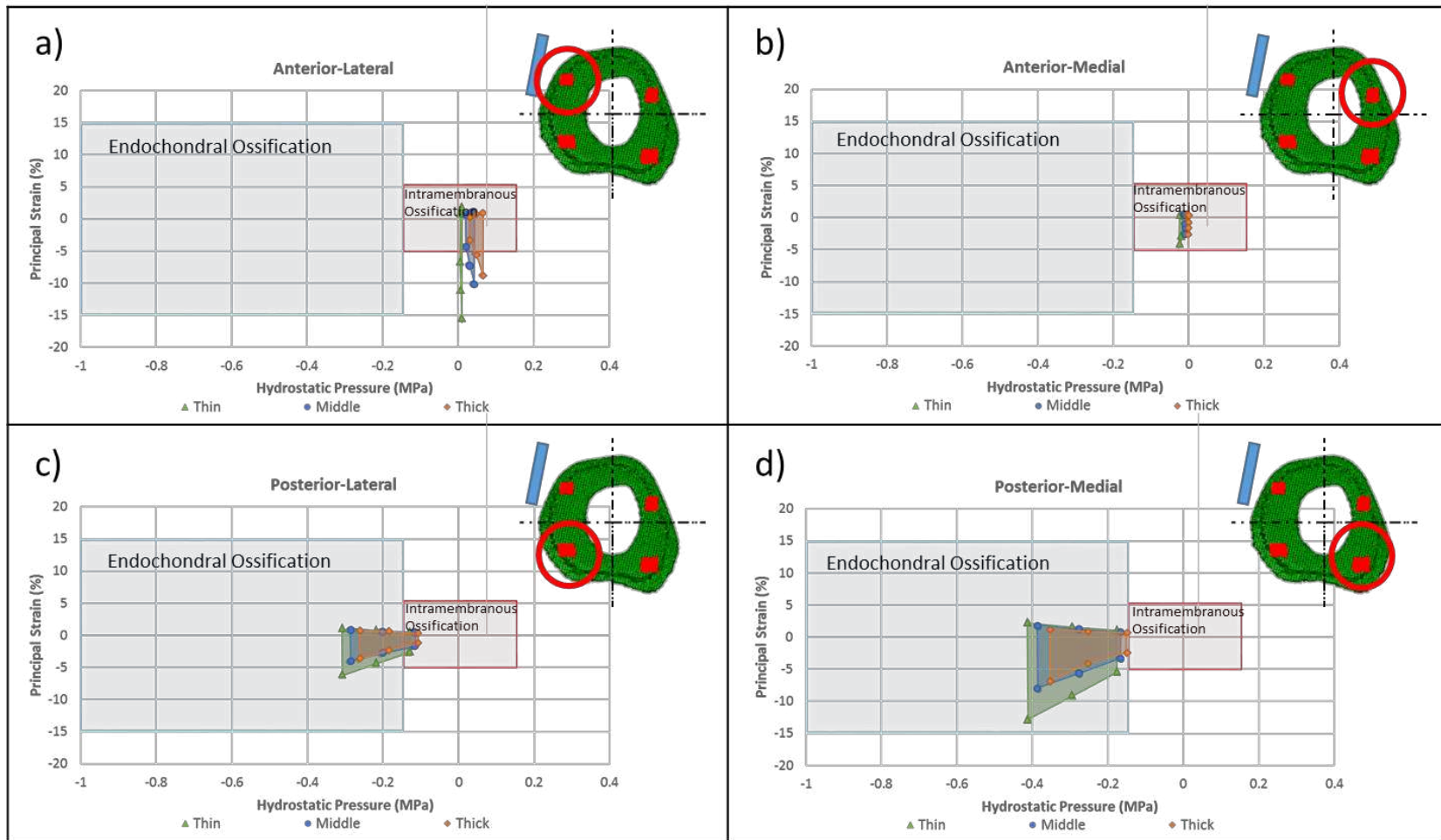


Figure 45: 10kPa -The specific hydrostatic pressures and strains envelopes found from Claes and Heigele [59] are plotted here in the shadowed regions for both endochondral ossification and intramembranous ossification. Over top of these envelopes are the predicted specific hydrostatic pressures plotted against the max and minimum principal strains in each callus region probed (AM, PM, PL, AL) over 3 loading magnitudes (300 N, 500 N, 700 N) for the 10 kPa callus modulus. An illustration of the callus regions is shown in the top right corner of each sub-plot showing the plates approximate location (blue) and the respective cells location of interest.

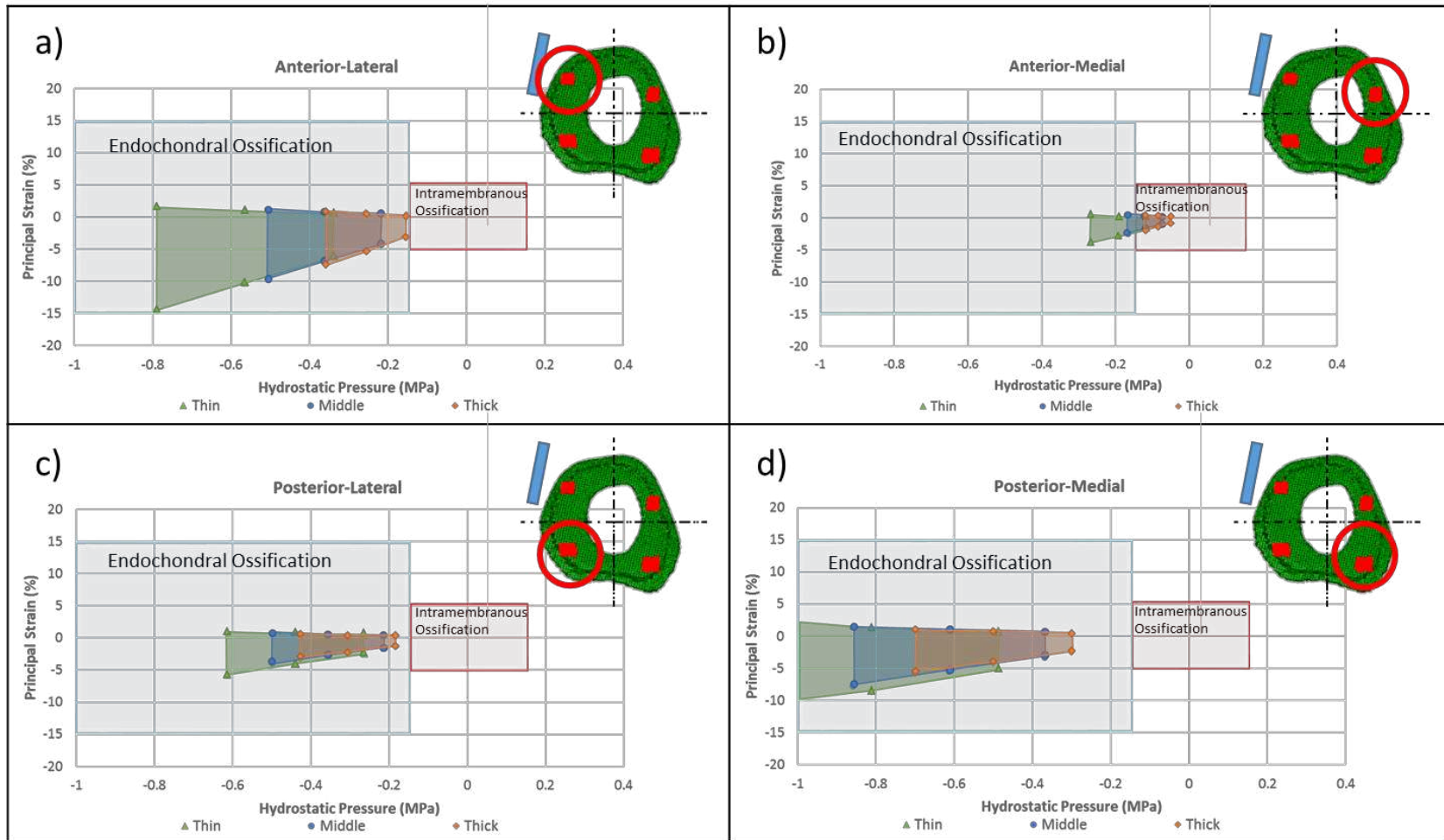


Figure 46: 100kPa - The specific hydrostatic pressures and strains envelopes found from Claes and Heigele [59] are plotted here in the shadowed regions for both endochondral ossification and intramembranous ossification. Over top of these envelopes are the predicted specific hydrostatic pressures plotted against the max and minimum principal strains in each callus region probed (AM, PM, PL, AL) over 3 loading magnitudes (300 N, 500 N, 700 N) for the 100 kPa callus modulus. An illustration of the callus regions is shown in the top right corner of each sub-plot showing the plates approximate location (blue) and the respective cells location of interest.

Mechanical prediction envelopes (regions enveloped by the pressure and strain predictions for a specific plate) that fell outside of the shaded regions (endochondral ossification or intramembranous ossification) were theorized to lead to unsatisfactory healing outcomes [59]. Envelopes that were completely enveloped within the endochondral and intramembranous ossification zones were theorized to lead to desirable healing outcomes [59]. Primary bone healing was not considered likely for this model, as the modeled fracture gap was 3 mm and primary bone healing only occurs at fracture gap distances below 0.01 mm [122]. As secondary healing is dominated by mostly endochondral ossification, predictions for this type of tissue proliferation were considered most favorable.

At 1 kPa callus modulus, the hydrostatic pressure didn't appear to be greatly influenced by the plate stiffness, however, the callus principal strains did change as a function of plate stiffness (Figure 44). The predicted maximum and minimum principal strains were reduced in magnitude as the plates thickness increased. The models' predictions indicated the strain magnitude would be an important consideration for the anterior-lateral region of the callus only. Here, some of the strains were predicted to be too high in magnitude for intramembranous ossification and with only tensile hydrostatic pressures; the conditions for endochondral ossification were not expected (Figure 44a). The anterior-lateral region data indicated that some regions of each envelope (i.e., at least one prediction for all three plate thicknesses) were predicted to not accommodate normal healing and would instead lead to proliferation of connective tissue or fibrocartilage. In this region, the thicker plate has the smallest non-healing predicted region (i.e., the least predicted mechanics region that exceeds the literature mechanical limitations; Figure 44a). Therefore, the thick plate

was theorized to be the least likely to exceed the mechanical limitations during acute stages of healing in the AL region.

When the callus modulus was simulated as 10 kPa, the hydrostatic pressure was more influenced by the plate stiffness as compared to when the callus elastic modulus was set to 1 kPa. The maximum and minimum principal strains were reduced in magnitude in every region as the plate's thickness was increased (Figure 45). The models' predictions indicated this was an important consideration for the anterior-lateral region of the callus. Where, some of the strains were predicted to be too high in magnitude for intramembranous ossification, and with only tensile hydrostatic pressures, the conditions for endochondral ossification were not expected (Figure 45a). The AL region for the 10 kPa callus modulus, similar to the AL region of 1 kPa predictions, was predicted to not accommodate intramembranous ossification for normal loading for the thin plate, and would instead lead to proliferation of connective tissue or fibrocartilage. In this AL region, the thicker plate was predicted to encourage intramembranous ossification under higher loads, as compared to the other two thickness plates (Figure 45a), and would, therefore, be most likely to aid in healing of this region in early stages of healing. The thick plate's strain-pressure envelopes in the AL region were also not predicted to change the type of bone healing as compared to the middle thickness and thin plates for any other region when the callus elastic modulus was set at 10 kPa.

For the stiffest callus micromechanics investigation (100 kPa), all pressures were predicted to be compressive (i.e., negative in sign; Figure 46), indicating that principal strains were the more significant factor effecting tissue differentiation (as compared to hydrostatic pressure) once the callus has reached this level of mechanical robustness. This was because there is no reported

compressive pressure limit for endochondral ossification, only a threshold between intramembranous and endochondral ossification [59]. In the posterior-lateral region, the minimum principal strain magnitude for the thin plate was predicted to approach the upper limit of the threshold of strain for endochondral ossification (-15%) at the highest load (i.e., 700 N; Figure 46c). A thicker plate, therefore, would decrease the chance of exceeding this limit and, consequently, decrease the risk of non-union due to excessive strain.

For all simulated loads, it was predicted that secondary (normal) bone healing would occur in the callus (Figure 46). One possible exception was the thick plate wherein the model predicted intramembranous ossification in the AM region due to relatively low magnitudes of hydrostatic pressure (i.e., between ± 0.16 MPa; Figure 46b). Other regions (i.e., AL, PL, and PM) for the thick plate were predicted to undergo endochondral ossification; this low pressure region (AM) may not prevent union as the other regions are expected to heal around it. The middle (3.8 mm) thickness plate could result in more successful union as it is predicted to encourage endochondral ossification in every region (Figure 46). The plate strain-pressure envelopes did not predict a change in the type of ossification for any other region at 100kPa callus elastic modulus in relation to plate thickness.

As the callus modulus increased (from 1 kPa to 10 kPa to 100 kPa), the hydrostatic pressure predictions were increasingly affected by the plate stiffness. The predicted maximum and minimum principal strains were reduced in magnitude, and the hydrostatic pressures were predicted to increase at every point as the plates thickness increased. The predictions indicated that

after the extremely early stages of healing (1 kPa - 10 kPa), all hydrostatic pressures were expected to be compressive which would be expected to promote endochondral ossification.

6. Discussion

Fracture region mechanics in long bone fracture healing have been shown to correlate directly to tissue differentiation and, therefore, the quality of healing [42], [59], [113], [114], [123]. Pauwels et al. described a model of fracture healing in which deviatoric strains and hydrostatic pressure have a causal effect on tissue differentiation [47]. Claes and Heigele published data supporting this model and postulated specific mechanical strain and hydrostatic pressure envelopes that lead to different types of tissue proliferation [59]. The stiffness of orthopaedic hardware that support fractures have been shown to have a direct effect on fracture region micromechanics [70], and thus the quality of fracture healing. Currently in the United States, approximately 10% of orthopaedic implants lead to delayed non-union [19], many due to inadequate biomechanical stability (via over or under stimulation) at the fracture ROI. It is, therefore, imperative to consider the stiffness of fixation hardware as a means to control fracture region mechanics, and thus, improve healing success.

The goal of the current project was to investigate the effect of altering fixation stiffness via geometric variations had on ovine supracondylar fracture callus micromechanics. Supracondylar fractures account for 60-75% of all elbow fractures and 7% of all femoral fractures in adolescents [3]–[5], which have been shown to have significant disturbances to circulation and growth[7]. Improving therapy for supracondylar fractures is therefore an area of critical clinical relevance. FEA was utilized to predict the changes in fracture region micromechanics as a function of plate stiffness, thus giving insight into the effect on tissue differentiation and quality of healing. Specifically, plates of three thicknesses/stiffnesses were designed and manufactured to support a

supracondylar fracture model in ovine femurs. The plates were used to experimentally validate finite element model strain predictions so that further analysis could be used to predict these callus micromechanics.

A novel ovine supracondylar fracture model was successfully created with the help of veterinary surgical collaborations. The model was comparable to human supracondylar fractures in location [1], [2], [92], and was shown to involve both of the trabecular and cortical bone, a critical phenomenon observed in human clinical settings [92]. However, further *in vivo* studies using this model are needed to prove the level of translational relevance. Regardless, the FEA data indicated that this model can be used for research into supracondylar fracture mechanics.

Three different thickness plates were manufactured to stabilize the novel ovine supracondylar fracture model. The design goals of the middle thickness and thin plates having 85% and 66% respective relative stiffness when compared to the thick plate were met within 5%. These designs support the use of altering plate thickness to tailor plate stiffness. To our knowledge, this was the first instance of comparing different stiffness plates of the same design. However, there have been published studies that have investigated novel materials which have shown the potential benefits of using different stiffness hardware to improve healing. Specifically, Bartinkowski et al. altered construct stiffness during the healing process of an ovine tibiae fracture model [114]. Their results showed that implant stiffness can directly influence the quality of healing at different post-stabilization time points by influencing the micromechanics in the fracture region. This method is only functional for easily accessible hardware (i.e., external-fixator systems), which is not realistic

for wide-scale clinical use in humans. The results of the work do, however, support the significance of the current work of improving fracture fixation success rates via optimizing fixation stiffness.

The results of the bone strain validation (Figure 33) showed that the initial isolated femoral finite element model accurately predicted axial bone surface strains. The values of bone strain reported in this work correlated well with the literature [46], [71], [73], [124]. Specifically, Lanyon et al. measured strain on human femur under physiological loading and reported peak strains of approximately 300 microstrain on the diaphysis surface [71]. This was similar to the measured and predicted surface strain magnitudes in the current study which reported strains between 218 and 805 microstrain (measured) in magnitude (Figure 33). Schilio et al. measured and predicted surface bone strains in human cadaveric femurs under compressive loading and reported values ranging between approximately -1200 to 1000 microstrain [124], which was similar to the measured strain range of -444.42 to 805.08 microstrain (measured) reported for this study (Figure 33). The agreement with values of bone surface strain reported in the literature, along with the agreement between the experimentally measured and FE predicted strains presented within this study, strongly suggests that the femoral FE model, generated for this study, is valid for simulating physiological mechanics.

The presented predictions of the strains on the plates over a simulated fracture healing (Figure 37- Figure 39) followed expected trends. Gages 1, 2 and 3, for all plates, showed a decrease in strain as callus modulus was increased. These trends reflected previously shown trends of a reduction in mechanical hardware strain as the fractures healed [74], [75]. However, one aspect not captured by this studies' model is a phenomenon shown by Stoffel et al., where the microstrain borne by

the hardware actually increases for a short period of time after surgery before decreasing as expected due to increased callus stability [75]. This acute increase in strain could possibly be due to an increase in hydrostatic pressure at the callus site during the initial healing cascade caused by the inflammatory response that has a stiffening effect within the callus. This phenomenon should be further explored for the model to be completely translatable within the acute healing period.

The strain gage that was located over the fracture region (gage 2) consistently predicted the highest strains, which correlates with previous findings reported in the literature. McLaughlin et al. attached strain gages to a bone plate that was fixed to an osteotomized synthetic femur in compression and reported peak strain magnitudes (approximately 400 microstrain) over the simulated fracture region [125]. They also reported a relatively lower magnitude of strains as the distance increased further from the fracture region. These data correlate with the results in the current study as seen in the relatively low strain predictions of gage 4 (Figure 34 - Figure 36). McLaughlin et al.'s work also reported strain values in the range of approximately -150 to 600 microstrain for a load of 500 N in a 6 mm plate. The current study showed a range of strain of approximately 170 to 2280 microstrain for 700 N on 5.6 mm plate. Although the comparison has some mitigating factors (i.e., different bone properties, bone geometry, loading protocol, etc.), the strain predictions of the current study appeared reasonable. The data presented in this study agreed with literature on a number of observations (i.e., strain over healing cascade trends, strain magnitudes, etc.), and thus, the FE models were considered reasonable for bench-top experimental comparisons for validation.

The results of the bench-top measured plate strain showed similar trends to the strains predicted by the plate FEA models. The data indicated gages 1, 2 and 3 increased in measured strain

magnitude as the osteotomy was increased from intact to the full osteotomy case. The measured strain as a function of healing level also agreed with the literature [74], [75]. Specifically, although the comparison to Grasa et al. (Figure 2) is not entirely similar as they utilized ex-fix construct stiffness, they also reported a decrease in the fixture device borne loads as fracture healing progressed [74]. In addition, similar to the current study, Grasa et al. observed minimal load transition to the native tissue at the earliest and latter stages of healing [74]. This minimal load transition was reflected in the current study's FEA predictions and bench-top measurements. In the FE model, strain predictions saw the largest effect on plate mechanics when the callus stiffness was increase from 100 kPa to 10 MPa (100-fold increase in stiffness; Figure 34 - Figure 36). In the lower stiffness models, from 1 kPa to 100 kPa (100-fold increase in stiffness) minimal changes in plate mechanics were seen (Figure 34 - Figure 36). The higher stiffness models, from 10 MPa to 1 GPa (100-fold increase in stiffness) also saw relatively small changes in strain borne by the hardware. For the bench-top measured data, significant increases in strain were seen for all plate thicknesses between three-quarter osteotomy (TQO) and full osteotomy (FO). Small changes were seen from the intact to half osteotomy (HO) to three-quarter osteotomy (TQO) models, even though the majority of the bone cross-sectional area had been transected. This transition in strain as a function of callus stability supports the implementation of the progressive osteotomy fracture model method used in the current work as it captured the loading phenomena and strain trends that are observable in the natural healing process.

The FE models successfully predicted the majority (17 out of 24) of the plate region strains within a single deviation of the bench-top measured values for their respective fracture model levels. The half osteotomy and three quarter osteotomy levels could not be given direct correlations to callus

moduli as they were not considered reliably repetitive, however, the intact and full osteotomy levels were considered comparable to the both fracture gap modulus extremes (1 GPa and 1000 Pa). For both the middle thickness (3.8 mm) and the thick (4.6 mm) plates, gage 2 measured lower strains than were predicted by the FEA model (1.5 and 2.0 standard deviations lower respectively). This is, however, a relatively anomaly as the majority of locations were still accurately predicted.

For the thick (4.6 mm) plate, gage 2 measured an average strain that was lower than gages 1 and 3. One possible reason for this disparity was the thicker plates could have caused the screws to have less engagement length as the screw head was translated away from the bone due to the increased thickness of the plate. Screws were confirmed via radiograph to have dual cortical engagement, however, the quality of that engagement was not quantified. Beaupre et al. reported significant increases in fixation plate strength when using bi-cortical screws as compared to uni-cortical [126]. Thus, imperfect engagement might have produced strain propagation to the surrounding areas.

It was not currently known, with sufficient accuracy, what normal loading would be for an animal that has undergone a surgical fixation with these newly designed plates. Hence, the simulated loading regime (300 N, 500 N, 700 N, or 0.64-1.5 BW) provided an envelope which was thought to be physiological [83]. The simulated callus properties (elastic modulus range; 1-100 kPa) were intended to be representative of the first 3-4 weeks of healing. Gardner and Stoll reported on an FEA study of callus healing wherein they reported the 3-4 week healing period moduli to be between 0 kPa and 190 kPa [112] thus the 3 selected levels of 1 kPa, 10kPa, and 100kPa, should have been accurately representative of callus stiffness in this early time periods.

The values for the predicted strains and hydrostatic pressures within the fracture gap regions compared well to previously reported studies. Gadomski et al. performed a similar FEA effort and reported a clinically relevant decrease in hydrostatic pressure and principal strains as loading of the stabilized fractured limb was decreased [109]. In the current study, decreased loading was akin to increasing plate stiffness (thickness), thus reducing the callus tissue loading. The predictions of the current FE model, therefore, agreed with Gadomski et al.'s findings as it indicated a decrease in both hydrostatic pressure and strain as plate thickness (stiffness) was increased.

Based on the assumption that the predicted values hold clinical relevance, comparisons of the healing quality predictions of different models were obtained. The comparisons were based on the model's mechanics (principal strain and hydrostatic pressure) predictions as compared to literature [59]. At the earliest stages of healing, simulated here with a 1 kPa callus modulus, strains greater than 10% have been shown to prevent any healing [60], and therefore, for this extremely low modulus callus, increasing plate thickness was predicted to help minimize the risk of exceeding this strain limit. Klein et al. showed that the initial phase of healing is the most mechanically sensitive and continues to have an effect throughout healing [113]. Accordingly, the mechanics at this callus stiffness should be considered closely.

It was expected that the largest strains would be seen in the posterior-medial (PM) region as it was furthest from the plate. For the same angle of rotation of the bone segments relative to each other, caused by plate flexion, the displacement would be expected to increase with increasing distance from the plate-bone interface (Figure 47). This is because in bending the highest strains occur at

the furthest points from the neutral axis (expected to be near the plate-bone interface in the FE models). Although the PM region did experience higher strains than the PL and AM regions, for all models the AL region was predicted to have the highest magnitude strains. This implies that the callus mechanics were behaving differently than expected nearest the plate. The model predicted the plate to compress axially more than expected, reducing the significance of the bending strain (i.e., the mechanics were dominated by the axial-stress induced strain). This would explain why the bending strain is not significantly higher furthest from the neutral axis.

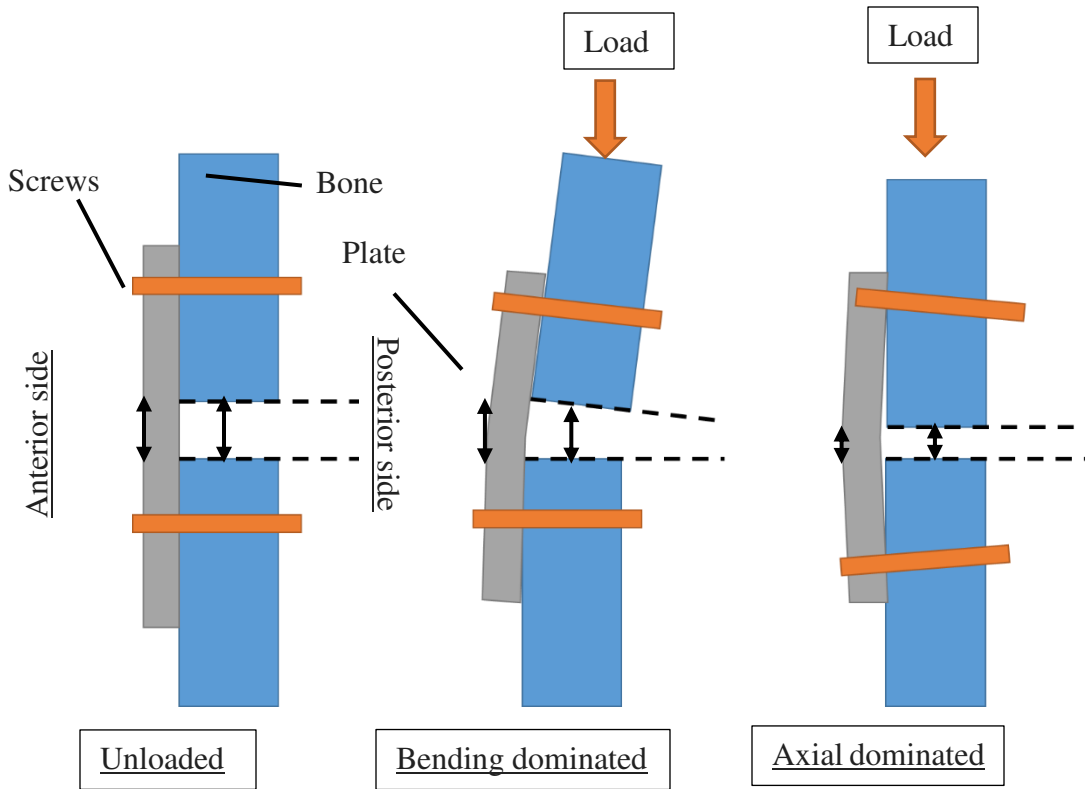


Figure 47: An illustration of how plate-bone construct flexion behaviour was expected under axial and bending dominated scenarios

From the data acquired through the callus micromechanics investigation, it was possible to draw some meaningful conclusions that could be used to guide recommendations for treatment of ovine supracondylar fractures with plates. The effect on hydrostatic pressure of plate thickness was not apparent at very early stages of simulated healing but became more significant as callus stiffness increased. The data indicated that hydrostatic pressure was of less importance than the strain values in tissue ossification type predictions as all values of hydrostatic pressure were within the reported limits of appropriate tissue differentiation for healing.

For the expected physiological loading, the thinnest plate was predicted to have relatively high, and possibly excessive, strains in the callus regions at the earliest stages of healing that would be

detrimental to fracture healing quality. Most non-unions are believed to be due to relatively high levels of inter-fragmentary motion [24], and therefore, the thin plate should be considered high risk. The thickest plate was predicted to accommodate normal healing, however, some predictions indicated intramembranous ossification may not be encouraged in some regions, which may inhibit proper healing. Normal bone healing typically requires mostly endochondral ossification, however, the intermediate callus phases (soft and hard callus) require intramembranous ossification [50], [127], therefore, a prediction for normal healing required both types of healing to be predicted. It was predicted that the middle thickness plate would accommodate stimulation of secondary bone healing, and, under normal loading, should have a low risk of exceeding fracture region tissue strain limits. It has been shown that higher levels of strain (as long as they are tolerable) is positively correlated to callus stiffness [123], which supports recommending the middle thickness plate based on the models predictions. The middle thickness (3.8 mm) plate was, therefore, predicted to accommodate the best healing outcome as the FEA simulations predicted the highest tolerable strains and pressures that encouraged endochondral ossification.

Simply put, all plates were predicted to accommodate secondary fracture healing via intramembranous and endochondral ossification, however, some plate thicknesses would promote healing better than others. The thin plate is considered to provide too high of a risk for exceeding local strain limitations, which may complicate the healing cascade. The thickest plate may provide less optimal stimulation than the middle thickness plate, and, associated slow healing. Increasing plate thickness decreased fracture gap strain predictions and increased hydrostatic pressure predictions for all regions in the callus. These effects are what should be considered when choosing plate thickness for attempting to control fracture healing outcomes.

Some simplifying limitations exist in the modeling work and experimental application of the current study. Modeling assumptions were made to reduce computational complexity and running time. Screw connections were considered fixed in the plate screw holes and the bone. Considering the screws used were bi-cortical locking screws, it was expected that friction between the hardware and bone should have had very little influence on the resultant mechanics and predictions. Additionally, the callus was assumed to have a bone geometry instead of a protruded callus, however, this is a common assumption in fracture FEA [128]–[131] as the true callus geometry is difficult to predict. A major assumption made for this work was that the models' predicted principal strains were not comparable to measured data as they could not be adequately captured using wired planar strain rosettes. This assumption was supported by finite computational and empirical analyses, which were consistent by showing out-of-surface plane principal strains.

The data showed that the model successfully predicted strains for both bone and plate surfaces for all plate thicknesses and for multiple levels of the progressive osteotomy model. With the validated model, callus region principal strains and hydrostatic pressures were successfully correlated to literature values and tissue type proliferation predictions were made. The results showed that the model could successfully predict the effects that changing the thickness of a plate design had on the local fracture mechanics.

7. Conclusions

The first aim of this work was to computationally simulate a plated ovine supracondylar fracture model and investigate the influence of three different plate thicknesses on the mechanical behavior of the plates and the micro-mechanical environment of the fracture callus over a simulated healing cascade. Models for all three plate thicknesses were successfully created and utilized to make tissue type predictions in the callus region. The effects of changing plate thickness on the micromechanics of the fracture region were illustrated and compared to previously reported values for callus pressure and strain.

The second aim of this work was to conduct bench-top experiments on simulated supracondylar fractures that are stabilized with plates of 3 different thicknesses in an ovine cadaveric model and compare to the computational model for validation. A total of 28 (n=28) ovine femur specimens were tested for either surface strains in a femur only experimental design or for plate strains in supracondylar fractures that were stabilized with plates. The strains were compared to the FE model's predictions and successfully validated the accuracy of all respective models (i.e., femur only and the three plate-fixed supracondylar fracture models).

Plate stiffness was effectively controlled via changing the plate thickness in an inverse linear relationship. Increasing plate stiffness decreased both maximum and minimum principal strains and drove predicted pressures to be more negative. For the current study, the middle plate would be recommended as it was predicted to accommodate healing the best via mechanics predictions correlated to reported ossification envelopes.

An *in vivo* study using the plates from the current study on live ovine specimens is needed to confirm the models efficacy for predicting healing effects. If the 3 plates were used to fix surgically transected femurs in live sheep, the healing cascade could be monitored over a normal healing period. Histological analysis would confirm the tissue types and amount of proliferation which could then be directly compared to the predictions presented in this work.

The potential impacts of this research have been identified in both clinical guidance and complimentary to future works. If the model was found to be useful in predicting fracture tissue repair quality, a similar model could be developed for human surgical guidance. This model could aid plate design in being more patient-specific as a clinician could be informed on what stiffness will lead to the most ideal healing outcome. Successfully predicting patient fracture mechanics for different fixation options could dramatically reduce the rate of non-union and increase the quality of care currently offered.

References

- [1] H. Nikolić, N. Bukvić, Z. Tomasić, A. Bosak, and T. Cicvarić, “Bone remodeling after supracondylar humeral fracture in children,” *Coll Antropol*, vol. 38, no. 2, pp. 601–604, Jun. 2014.
- [2] E. Cekanauskas, R. Degliūte, and R. J. Kalesinskas, “[Treatment of supracondylar humerus fractures in children, according to Gartland classification],” *Medicina (Kaunas)*, vol. 39, no. 4, pp. 379–383, 2003.
- [3] E. K. Rodriguez *et al.*, “Predictive factors of distal femoral fracture nonunion after lateral locked plating: a retrospective multicenter case-control study of 283 fractures,” *Injury*, vol. 45, no. 3, pp. 554–559, Mar. 2014.
- [4] M. Zlowodzki, M. Bhandari, D. J. Marek, P. A. Cole, and P. J. Kregor, “Operative treatment of acute distal femur fractures: systematic review of 2 comparative studies and 45 case series (1989 to 2005),” *J Orthop Trauma*, vol. 20, no. 5, pp. 366–371, May 2006.
- [5] M. Ehlinger, G. Ducrot, P. Adam, and F. Bonnomet, “Distal femur fractures. Surgical techniques and a review of the literature,” *Orthop Traumatol Surg Res*, vol. 99, no. 3, pp. 353–360, May 2013.
- [6] H. M. Kronenberg, “Developmental regulation of the growth plate,” *Nature*, vol. 423, pp. 332–336, May 2003.
- [7] C. J. Basener, C. T. Mehlman, and T. G. DiPasquale, “Growth Disturbance After Distal Femoral Growth Plate Fractures in Children: A Meta-Analysis,” *Journal of Orthopaedic Trauma*, vol. 23, no. 9, p. 663, Oct. 2009.

- [8] T. E. Kanakis and J. Cordey, “Is there a mechanical difference between lag screws and double cerclage?,” *Injury*, vol. 22, no. 3, pp. 185–189, May 1991.
- [9] M. Hoenig, F. Gao, J. Kinder, L.-Q. Zhang, C. Collinge, and B. R. Merk, “Extra-Articular Distal Tibia Fractures: A Mechanical Evaluation of 4 Different Treatment Methods:,” *Journal of Orthopaedic Trauma*, vol. 24, no. 1, pp. 30–35, Jan. 2010.
- [10] G.-I. Im and S.-K. Tae, “Distal metaphyseal fractures of tibia: a prospective randomized trial of closed reduction and intramedullary nail versus open reduction and plate and screws fixation,” *J Trauma*, vol. 59, no. 5, pp. 1219–1223; discussion 1223, Nov. 2005.
- [11] K. W. Janssen, J. Biert, and A. van Kampen, “Treatment of distal tibial fractures: plate versus nail,” *Int Orthop*, vol. 31, no. 5, pp. 709–714, Oct. 2007.
- [12] B. L. Ohlson, M. W. Shatby, B. G. Parks, K. L. White, and L. C. Schon, “Periarticular locking plate vs intramedullary nail for tibiototalcaneal arthrodesis: a biomechanical investigation,” *Am J. Orthop.*, vol. 40, no. 2, pp. 78–83, Feb. 2011.
- [13] S. M. David, M. E. Harrow, R. D. Peindl, S. L. Frick, and J. F. Kellam, “Comparative Biomechanical Analysis of Supracondylar Femur Fracture Fixation: Locked Intramedullary Nail Versus 95-Degree Angled Plate,” *Journal of Orthopaedic Trauma*, vol. 11, no. 5, p. 344, Jul. 1997.
- [14] K. J. Koval, J. J. Hoehl, F. J. Kummer, and J. A. Simon, “Distal femoral fixation: a biomechanical comparison of the standard condylar buttress plate, a locked buttress plate, and the 95-degree blade plate,” *J Orthop Trauma*, vol. 11, no. 7, pp. 521–524, Oct. 1997.
- [15] L. P. Hsu, E. G. Schwartz, D. M. Kalainov, F. Chen, and R. L. Makowiec, “Complications of K-Wire Fixation in Procedures Involving the Hand and Wrist,” *The Journal of Hand Surgery*, vol. 36, no. 4, pp. 610–616, Apr. 2011.

- [16] C. S. Kwok, P. T. Crossman, and C. L. Loizou, "Plate Versus Nail for Distal Tibial Fractures: A Systematic Review and Meta-Analysis," *Journal of Orthopaedic Trauma*, vol. 28, no. 9, pp. 542–548, Sep. 2014.
- [17] M. E. C. Gracitelli, E. A. Malavolta, J. H. Assunção, A. A. F. Neto, J. S. Silva, and A. J. Hernandez, "Locking intramedullary nails versus locking plates for the treatment of proximal humerus fractures," *Expert Review of Medical Devices*, vol. 14, no. 9, pp. 733–739, Sep. 2017.
- [18] H. Schell, G. N. Duda, A. Peters, S. Tsitsilonis, K. A. Johnson, and K. Schmidt-Bleek, "The haematoma and its role in bone healing," *Journal of Experimental Orthopaedics*, vol. 4, no. 1, Dec. 2017.
- [19] A. Nauth, T. Miclau, R. Li, and E. H. Schemitsch, "Gene therapy for fracture healing," *J Orthop Trauma*, vol. 24 Suppl 1, pp. S17-24, Mar. 2010.
- [20] W.-H. Tay, R. de Steiger, M. Richardson, R. Gruen, and Z. J. Balogh, "Health outcomes of delayed union and nonunion of femoral and tibial shaft fractures," *Injury*, vol. 45, no. 10, pp. 1653–1658, Oct. 2014.
- [21] E. Lindvall, R. Sanders, T. Dipasquale, D. Herscovici, G. Haidukewych, and C. Sagi, "Intramedullary nailing versus percutaneous locked plating of extra-articular proximal tibial fractures: comparison of 56 cases," *J Orthop Trauma*, vol. 23, no. 7, pp. 485–492, Aug. 2009.
- [22] J. W. Busse, M. Bhandari, S. Sprague, A. P. Johnson-Masotti, and A. Gafni, "An economic analysis of management strategies for closed and open grade I tibial shaft fractures," *Acta Orthop*, vol. 76, no. 5, pp. 705–712, Oct. 2005.
- [23] T. W. Axelrad, S. Kakar, and T. A. Einhorn, "New technologies for the enhancement of skeletal repair," *Injury*, vol. 38 Suppl 1, pp. S49-62, Mar. 2007.

- [24] D. S. Elliott *et al.*, “A unified theory of bone healing and nonunion: BHN theory,” *The Bone & Joint Journal*, vol. 98-B, no. 7, pp. 884–891, Jul. 2016.
- [25] A. A. Patel and S. M. Quinnan, “Skeletal Traction Pin Placement,” in *Case Competencies in Orthopaedic Surgery*, Elsevier, 2017, pp. 239–244.
- [26] Jennifer Dickson, C. A. Gunn, and J. G. Chase, “Humans are Horribly Variable | International Journal of Clinical & Medical Images,” *International Journal of Clinical & Medical Images*, vol. 1, no. 2, 2014.
- [27] F. Johannesdottir and M. L. Bouxsein, “Chapter 12 - Overview of Bone Structure and Strength,” in *Genetics of Bone Biology and Skeletal Disease (Second Edition)*, R. V. Thakker, M. P. Whyte, J. A. Eisman, and T. Igarashi, Eds. Academic Press, 2018, pp. 197–208.
- [28] M. L. Bouxsein and D. Karasik, “Bone geometry and skeletal fragility,” *Current Osteoporosis Reports*, vol. 4, no. 2, pp. 49–56, Jun. 2006.
- [29] M. Navarro, A. Michiardi, O. Castaño, and J. . Planell, “Biomaterials in orthopaedics,” *J R Soc Interface*, vol. 5, no. 27, pp. 1137–1158, Oct. 2008.
- [30] K. Bundy, “3 - Biomaterials and the chemical environment of the body,” in *Joint Replacement Technology*, P. A. Revell, Ed. Woodhead Publishing, 2008, pp. 56–80.
- [31] D. Kuroda, M. Niinomi, M. Morinaga, Y. Kato, and T. Yashiro, “Design and mechanical properties of new β type titanium alloys for implant materials,” *Materials Science and Engineering: A*, vol. 243, no. 1, pp. 244–249, Mar. 1998.
- [32] D. G. Kwon, T. J. Lee, J. S. Kang, and K. H. Moon, “Correlation Between Stress Shielding and Clinical Outcomes After Total Hip Arthroplasty with Extensively Porous Coated Stems,” *The Journal of Arthroplasty*, vol. 28, no. 10, pp. 1728–1730, Dec. 2013.

- [33] “Problem of Stress Shielding and Improvement to the Hip Implant Designs: A Review,” *Science Alert*. [Online]. Available: <https://scialert.net/fulltext/?doi=jms.2007.460.467>. [Accessed: 25-Oct-2018].
- [34] S. T. Lin, S. Conjeevaram, and D. J. Henderson, “Moldable bone-implant material,” US4645503A, 24-Feb-1987.
- [35] T. Kokubo, H.-M. Kim, and M. Kawashita, “Novel bioactive materials with different mechanical properties,” *Biomaterials*, vol. 24, no. 13, pp. 2161–2175, Jun. 2003.
- [36] M. P. Staiger, A. M. Pietak, J. Huadmai, and G. Dias, “Magnesium and its alloys as orthopedic biomaterials: A review,” *Biomaterials*, vol. 27, no. 9, pp. 1728–1734, Mar. 2006.
- [37] R. J. Minns and W. K. Walsh, “Preliminary Design and Experimental Studies of a Novel Soft Implant for Correcting Sagittal Plane Instability in the Lumbar Spine,” *Spine*, vol. 22, no. 16, p. 1819, Aug. 1997.
- [38] A. Lambotte, “L’utilisation du magnesium comme materiel perdu dans l’osteosynthese,” *Bull Mem Soc Nat*, vol. Chir 28, pp. 1325–1334, 1932.
- [39] K. C. Walley, M. Bajraliu, T. Gonzalez, A. Nazarian, and J. A. Goulet, “The Chronicle of a Stainless Steel Orthopaedic Implant,” *The Orthopaedic Journal at Harvard Medical School*, vol. 17, pp. 68–74, 2016.
- [40] T. A. Einhorn and L. C. Gerstenfeld, “Fracture healing: mechanisms and interventions,” *Nat Rev Rheumatol*, vol. 11, no. 1, pp. 45–54, Jan. 2015.
- [41] M. G. Giganti *et al.*, “Fracture healing: from basic science to role of nutrition,” *Front Biosci (Landmark Ed)*, vol. 19, pp. 1162–1175, Jun. 2014.

[42] G. J. Miller, L. C. Gerstenfeld, and E. F. Morgan, “Mechanical microenvironments and protein expression associated with formation of different skeletal tissues during bone healing,” *Biomech Model Mechanobiol*, vol. 14, no. 6, pp. 1239–1253, Nov. 2015.

[43] M. Steiner, L. Claes, A. Ignatius, F. Niemeier, U. Simon, and T. Wehner, “Prediction of fracture healing under axial loading, shear loading and bending is possible using distortional and dilatational strains as determining mechanical stimuli,” *J R Soc Interface*, vol. 10, no. 86, Sep. 2013.

[44] D. J. Hak *et al.*, “Delayed union and nonunions: epidemiology, clinical issues, and financial aspects,” *Injury*, vol. 45 Suppl 2, pp. S3-7, Jun. 2014.

[45] K. D. Hankenson, G. Zimmerman, and R. Marcucio, “Biological perspectives of delayed fracture healing,” *Injury*, vol. 45 Suppl 2, pp. S8–S15, Jun. 2014.

[46] A. D. Martin and R. G. McCulloch, “Bone dynamics: Stress, strain and fracture,” *Journal of Sports Sciences*, vol. 5, no. 2, pp. 155–163, Jun. 1987.

[47] F. Pauwels, “Eine neue Theorie über den Einfluß mechanischer Reize auf die Differenzierung der Stützgewebe,” *Z. Anat. Entwickl. Gesch.*, vol. 121, no. 6, pp. 478–515, Nov. 1960.

[48] R. Marsell and T. A. Einhorn, “THE BIOLOGY OF FRACTURE HEALING,” *Injury*, vol. 42, no. 6, pp. 551–555, Jun. 2011.

[49] S. F. Gilbert, “Osteogenesis: The Development of Bones,” *Developmental Biology*. 6th edition, 2000.

[50] “Three-dimensional reconstruction of fracture callus morphogenesis. - PubMed - NCBI.” [Online]. Available: <https://www.ncbi.nlm.nih.gov/pubmed/16864894>. [Accessed: 28-Nov-2018].

[51] S. M. Perren, “Evolution of the internal fixation of long bone fractures. The scientific basis of biological internal fixation: choosing a new balance between stability and biology,” *J Bone Joint Surg Br*, vol. 84, no. 8, pp. 1093–1110, Nov. 2002.

[52] S. M. Perren, “Backgrounds of the technology of internal fixators,” *Injury*, vol. 34, pp. 1–3, Nov. 2003.

[53] S. M. Perren, A. Fernandez, and P. Regazzoni, “Understanding Fracture Healing Biomechanics Based on the ‘Strain’ Concept and its Clinical Applications.,” *Acta Chir Orthop Traumatol Cech*, vol. 82, no. 4, pp. 253–260, 2015.

[54] “Risk factors, treatment, and outcomes associated with nonunion of the midshaft humerus fracture. - PubMed - NCBI.” [Online]. Available: <https://www.ncbi.nlm.nih.gov/pubmed/16115430/>. [Accessed: 28-Nov-2018].

[55] A.-M. Collignon, J. Lesieur, C. Vacher, C. Chaussain, and G. Y. Rochefort, “Strategies Developed to Induce, Direct, and Potentiate Bone Healing,” *Front Physiol*, vol. 8, Nov. 2017.

[56] R. Bruce Martin and D. B. Burr, “A hypothetical mechanism for the stimulation of osteonal remodelling by fatigue damage,” *Journal of Biomechanics*, vol. 15, no. 3, pp. 137–139, Jan. 1982.

[57] H. M. Frost, “A 2003 Update of Bone Physiology and Wolff’s Law for Clinicians,” *The Angle Orthodontist*, vol. 74, no. 1, pp. 3–15, Feb. 2004.

[58] H. M. Frost, “The skeletal intermediary organization,” *Metabolic Bone Disease and Related Research*, vol. 4, no. 5, pp. 281–290, Jan. 1983.

- [59] L. E. Claes and C. A. Heigele, "Magnitudes of local stress and strain along bony surfaces predict the course and type of fracture healing," *Journal of Biomechanics*, vol. 32, no. 3, pp. 255–266, Mar. 1999.
- [60] K. A. Egol, E. N. Kubiak, E. Fulkerson, F. J. Kummer, and K. J. Koval, "Biomechanics of Locked Plates and Screws," *Journal of Orthopaedic Trauma*, vol. 18, no. 8, p. 488, Sep. 2004.
- [61] M. S. Linn, C. M. McAndrew, B. Prusaczyk, O. Brimmo, W. M. Ricci, and M. J. Gardner, "Dynamic Locked Plating of Distal Femur Fractures," *J Orthop Trauma*, vol. 29, no. 10, pp. 447–450, Oct. 2015.
- [62] T. Schmickal, J. von Recum, and A. Wentzensen, "Stiffness measurement of the neocallus with the Fraktometer FM 100," *Arch Orthop Trauma Surg*, vol. 125, no. 10, pp. 653–659, Dec. 2005.
- [63] J. Webb, G. Herling, T. Gardner, J. Kenwright, and A. H. R. W. Simpson, "Manual assessment of fracture stiffness," *Injury*, vol. 27, no. 5, pp. 319–320, Jun. 1996.
- [64] S. Morshed, "Current Options for Determining Fracture Union," *Advances in Medicine*, 2014. [Online]. Available: <https://www.hindawi.com/journals/amed/2014/708574/>. [Accessed: 03-Dec-2018].
- [65] R. Schmidhammer *et al.*, "Assessment of bone union/nonunion in an experimental model using microcomputed technology," *J Trauma*, vol. 61, no. 1, pp. 199–205, Jul. 2006.
- [66] N. A. Ebraheim, M. C. Skie, B. E. Heck, and W. T. Jackson, "Metaphyseal nonunion: a diagnostic dilemma," *J Trauma*, vol. 38, no. 2, pp. 261–268, Feb. 1995.

- [67] P. K. Inaparthi and J. E. Nicholl, "Treatment of Delayed/Nonunion of Scaphoid Waist with Synthes Cannulated Scaphoid Screw and Bone Graft," *Hand (N Y)*, vol. 3, no. 4, pp. 292–296, Dec. 2008.
- [68] L. Claes *et al.*, "Monitoring and healing analysis of 100 tibial shaft fractures," *Langenbecks Arch Surg*, vol. 387, no. 3–4, pp. 146–152, Jul. 2002.
- [69] K. C. McGilvray *et al.*, "Implantable microelectromechanical sensors for diagnostic monitoring and post-surgical prediction of bone fracture healing: IMPLANTABLE MICROELECTROMECHANICAL SENSORS FOR DIAGNOSTIC MONITORING," *Journal of Orthopaedic Research*, vol. 33, no. 10, pp. 1439–1446, Oct. 2015.
- [70] J. R. Field, H. Törnkvist, T. C. Hearn, G. Sumner-Smith, and T. D. Woodside, "The influence of screw omission on construction stiffness and bone surface strain in the application of bone plates to cadaveric bone," *Injury*, vol. 30, no. 9, pp. 591–598, Nov. 1999.
- [71] L. E. Lanyon, W. G. J. Hampson, A. E. Goodship, and J. S. Shah, "Bone Deformation Recorded in vivo from Strain Gauges Attached to the Human Tibial Shaft," *Acta Orthopaedica Scandinavica*, vol. 46, no. 2, pp. 256–268, Jan. 1975.
- [72] A. S. Turner, E. J. Mills, and A. A. Gabel, "In vivo measurement of bone strain in the horse.," *Am J Vet Res*, vol. 36, no. 11, pp. 1573–1579, Nov. 1975.
- [73] W. L. Hylander, "In vivo bone strain in the mandible of *Galago crassicaudatus*," *Am. J. Phys. Anthropol.*, vol. 46, no. 2, pp. 309–326, Mar. 1977.
- [74] J. Grasa, M. J. Gómez-Benito, L. A. González-Torres, D. Asiaín, F. Quero, and J. M. García-Aznar, "Monitoring in vivo load transmission through an external fixator," *Ann Biomed Eng*, vol. 38, no. 3, pp. 605–612, Mar. 2010.

- [75] K. Stoffel, K. Klaue, and S. M. Perren, "Functional load of plates in fracture fixation in vivo and its correlate in bone healing," *Injury-Int. J. Care Inj.*, vol. 31, pp. 37–50, May 2000.
- [76] T. J. R. Hughes, *The Finite Element Method: Linear Static and Dynamic Finite Element Analysis*. Courier Corporation, 2012.
- [77] P. Pivonka and C. R. Dunstan, "Role of mathematical modeling in bone fracture healing," *Bonekey Rep*, vol. 1, Nov. 2012.
- [78] C. F. Ross, "Finite element analysis in vertebrate biomechanics," *The Anatomical Record Part A: Discoveries in Molecular, Cellular, and Evolutionary Biology*, vol. 283A, no. 2, pp. 253–258, Apr. 2005.
- [79] D. Kluess, "Finite Element Analysis in Orthopaedic Biomechanics," *Finite Element Analysis*, 2010.
- [80] E. S. Orwoll *et al.*, "Finite element analysis of the proximal femur and hip fracture risk in older men," *J. Bone Miner. Res.*, vol. 24, no. 3, pp. 475–483, Mar. 2009.
- [81] J. Zhao, S. Ma, and X. Wei, "Finite Element Analysis of Femur Stress under Bending Moment and Compression Load," in *2009 2nd International Conference on Biomedical Engineering and Informatics*, Tianjin, China, 2009, pp. 1–4.
- [82] F. Mazoochian *et al.*, "Finite element analysis of the ovine hip: development, results and comparison with the human hip," *Vet Comp Orthop Traumatol*, vol. 25, no. 4, pp. 301–306, 2012.
- [83] Z. F. Lerner, B. C. Gadowski, A. K. Ipson, K. K. Haussler, C. M. Puttlitz, and R. C. Browning, "Modulating tibiofemoral contact force in the sheep hind limb via treadmill walking:

Predictions from an opensim musculoskeletal model,” *J. Orthop. Res.*, vol. 33, no. 8, pp. 1128–1133, Aug. 2015.

[84] AO Research Institute, AO Foundation, Clavadelerstrasse 8, Davos, Switzerland, A. Pearce, R. Richards, S. Milz, E. Schneider, and S. Pearce, “Animal models for implant biomaterial research in bone: A review,” *European Cells and Materials*, vol. 13, pp. 1–10, Mar. 2007.

[85] A.-M. Pobloth *et al.*, “Establishment of a preclinical ovine screening model for the investigation of bone tissue engineering strategies in cancellous and cortical bone defects,” *BMC Musculoskelet Disord*, vol. 17, Mar. 2016.

[86] K. A. Thomas *et al.*, “Bioresorbable Polylactide Interbody Implants in an Ovine Anterior Cervical Discectomy and Fusion Model: Three-Year Results,” *Spine*, vol. 33, no. 7, pp. 734–742, Apr. 2008.

[87] A. S. Turner, “The Sheep as a Model for Osteoporosis in Humans,” *The Veterinary Journal*, vol. 163, no. 3, pp. 232–239, May 2002.

[88] A. S. Turner, “Seasonal changes in bone metabolism in sheep: Further characterization of an animal model for human osteoporosis,” *The Veterinary Journal*, vol. 174, no. 3, pp. 460–461, Nov. 2007.

[89] E. Newman, A. S. Turner, and J. D. Wark, “The potential of sheep for the study of osteopenia: current status and comparison with other animal models,” *Bone*, vol. 16, no. 4 Suppl, pp. 277S-284S, Apr. 1995.

[90] S. Mohsin, F. J. O’Brien, and T. C. Lee, “Osteonal crack barriers in ovine compact bone,” *J Anat*, vol. 208, no. 1, pp. 81–89, Jan. 2006.

- [91] F. C. den Boer *et al.*, “New segmental long bone defect model in sheep: quantitative analysis of healing with dual energy x-ray absorptiometry,” *J. Orthop. Res.*, vol. 17, no. 5, pp. 654–660, Sep. 1999.
- [92] M. W. Chapman and C. G. Finkemeier, “Treatment of Supracondylar Nonunions of the Femur with Plate Fixation and Bone Graft*,” *JBJS*, vol. 81, no. 9, p. 1217, Sep. 1999.
- [93] “LISS for Distal Femur | DePuy Synthes Companies.” [Online]. Available: <https://www.depuysynthes.com/hcp/trauma/products/qs/LISS-for-Distal-Femur>. [Accessed: 08-Dec-2018].
- [94] B. Gervais, A. Vadean, M. Raison, and M. Brochu, “Failure analysis of a 316L stainless steel femoral orthopedic implant,” *Case Studies in Engineering Failure Analysis*, vol. 5–6, pp. 30–38, Apr. 2016.
- [95] Z. S. Bagheri, P. Tavakkoli Avval, H. Bougherara, M. S. R. Aziz, E. H. Schemitsch, and R. Zdero, “Biomechanical Analysis of a New Carbon Fiber/Flax/Epoxy Bone Fracture Plate Shows Less Stress Shielding Compared to a Standard Clinical Metal Plate,” *Journal of Biomechanical Engineering*, vol. 136, no. 9, p. 091002, Jun. 2014.
- [96] H. Mehboob and S.-H. Chang, “Effect of structural stiffness of composite bone plate–scaffold assembly on tibial fracture with large fracture gap,” *Composite Structures*, vol. 124, pp. 327–336, Jun. 2015.
- [97] R. Petersen, “Carbon Fiber Biocompatibility for Implants,” *Fibers*, vol. 4, no. 4, p. 1, Jan. 2016.
- [98] S. E. Benzley, E. Perry, K. Merkle, B. Clark, and G. Sjaardama, “A Comparison of All Hexagonal and All Tetrahedral Finite Element Meshes for Elastic and Elasto-plastic Analysis,” p. 13.

- [99] M. L. Hillier and L. S. Bell, "Differentiating Human Bone from Animal Bone: A Review of Histological Methods," *Journal of Forensic Sciences*, vol. 52, no. 2, pp. 249–263, Mar. 2007.
- [100] J. A. Buckwalter, M. J. Glimcher, R. R. Cooper, and R. Recker, "Bone Biology," *JBJS*, vol. 77, no. 8, p. 1256, Aug. 1995.
- [101] S. B. Lang, "Ultrasonic Method for Measuring Elastic Coefficients of Bone and Results on Fresh and Dried Bovine Bones," *IEEE Transactions on Biomedical Engineering*, vol. BME-17, no. 2, pp. 101–105, Apr. 1970.
- [102] S. F. Lipson and J. L. Katz, "The relationship between elastic properties and microstructure of bovine cortical bone," *Journal of Biomechanics*, vol. 17, no. 4, pp. 231–240, Jan. 1984.
- [103] "Long Bone Structure Structure Of Long Bone 3D 3D Diagram Of Long Bone Tag Long Bone," *Human Body Pictures*. .
- [104] D. M. Geraldles and A. T. M. Phillips, "A comparative study of orthotropic and isotropic bone adaptation in the femur," *Int J Numer Method Biomed Eng*, vol. 30, no. 9, pp. 873–889, Sep. 2014.
- [105] A. Nafei, J. Kabel, A. Odgaard, F. Linde, and I. Hvid, "Properties of growing trabecular ovine bone. Part II: architectural and mechanical properties," *J Bone Joint Surg Br*, vol. 82, no. 6, pp. 921–927, Aug. 2000.
- [106] A. Nafei, C. C. Danielsen, F. Linde, and I. Hvid, "Properties of growing trabecular ovine bone. Part I: mechanical and physical properties," *J Bone Joint Surg Br*, vol. 82, no. 6, pp. 910–920, Aug. 2000.

- [107] E. Mittra, C. Rubin, and Y.-X. Qin, “Interrelationship of trabecular mechanical and microstructural properties in sheep trabecular bone,” *Journal of Biomechanics*, vol. 38, no. 6, pp. 1229–1237, Jun. 2005.
- [108] W. W. Says, “Medical Applications of Stainless Steel 304 (UNS S30400),” *AZoM.com*, 30-Aug-2012. [Online]. Available: <https://www.azom.com/article.aspx?ArticleID=6641>. [Accessed: 03-Dec-2018].
- [109] B. C. Gadowski, Z. F. Lerner, R. C. Browning, J. T. Easley, R. H. Palmer, and C. M. Puttlitz, “Computational characterization of fracture healing under reduced gravity loading conditions,” *J. Orthop. Res.*, vol. 34, no. 7, pp. 1206–1215, Jul. 2016.
- [110] C. Zannoni, R. Mantovani, and M. Viceconti, “Material properties assignment to finite element models of bone structures: a new method,” *Medical Engineering & Physics*, vol. 20, no. 10, pp. 735–740, Feb. 1999.
- [111] L. W. Marks and T. N. Gardner, “The use of strain energy as a convergence criterion in the finite element modelling of bone and the effect of model geometry on stress convergence,” *Journal of Biomedical Engineering*, vol. 15, no. 6, pp. 474–476, Nov. 1993.
- [112] T. N. Gardner, T. Stoll, L. Marks, S. Mishra, and M. Knothe Tate, “The influence of mechanical stimulus on the pattern of tissue differentiation in a long bone fracture — an FEM study,” *Journal of Biomechanics*, vol. 33, no. 4, pp. 415–425, Apr. 2000.
- [113] P. Klein *et al.*, “The initial phase of fracture healing is specifically sensitive to mechanical conditions,” *J. Orthop. Res.*, vol. 21, no. 4, pp. 662–669, Jul. 2003.
- [114] N. Bartnikowski and B. Eng, “MODIFYING FIXATION STIFFNESS TO IMPROVE BONE HEALING,” p. 186.

[115] J. S. Nyman, A. Roy, X. Shen, R. L. Acuna, J. H. Tyler, and X. Wang, “The influence of water removal on the strength and toughness of cortical bone,” *J Biomech*, vol. 39, no. 5, pp. 931–938, 2006.

[116] B. Kaye, “The Effects of Freezing on the Mechanical Properties of Bone,” *The Open Bone Journal*, vol. 4, no. 1, pp. 14–19, Jun. 2012.

[117] I. Irubetagoiena, M. Verset, S. Palierne, P. Swider, and A. Autefage, “Ex vivo cyclic mechanical behaviour of 2.4 mm locking plates compared with 2.4 mm limited contact plates in a cadaveric diaphyseal gap model,” *Veterinary and Comparative Orthopaedics and Traumatology*, vol. 26, no. 06, pp. 479–488, 2013.

[118] S. Eberle, C. Wutte, C. Bauer, G. von Oldenburg, S. Panzer, and P. Augat, “Evaluation of Risk for Secondary Fracture After Removal of a New Femoral Neck Plate for Intracapsular Hip Fractures,” *Journal of Orthopaedic Trauma*, vol. 25, no. 12, p. 721, Dec. 2011.

[119] E. Walker, D. P. Mukherjee, A. L. Ogden, K. K. Sadasivan, and J. A. Albright, “A biomechanical study of simulated femoral neck fracture fixation by cannulated screws: effects of placement angle and number of screws,” *Am J. Orthop.*, vol. 36, no. 12, pp. 680–684, Dec. 2007.

[120] A. Freitas, W. F. Lula, J. S. de Oliveira, R. A. Maciel, D. R. de M. Souto, and P. F. Godinho, “Analysis of mechanical strength to fixing the femoral neck fracture in synthetic bone type Asnis,” *Acta Ortopédica Brasileira*, vol. 22, no. 4, pp. 206–209, Jul. 2014.

[121] “(PDF) Effect of Adhesive Type on the Measurement of Modulus of Elasticity Using Electrical Resistance Strain Gauges,” *ResearchGate*. [Online]. Available: https://www.researchgate.net/publication/281559049_Effect_of_Adhesive_Type_on_the_Measurement_of_Modulus_of_Elasticity_Using_Electrical_Resistance_Strain_Gauges. [Accessed: 08-Dec-2018].

[122] F. Shapiro, “Cortical bone repair. The relationship of the lacunar-canalicular system and intercellular gap junctions to the repair process,” *J Bone Joint Surg Am*, vol. 70, no. 7, pp. 1067–1081, Aug. 1988.

[123] D. P. Comiskey, B. J. Macdonald, W. T. McCartney, K. Synnott, and J. O’Byrne, “The role of interfragmentary strain on the rate of bone healing—a new interpretation and mathematical model,” *J Biomech*, vol. 43, no. 14, pp. 2830–2834, Oct. 2010.

[124] E. Schileo, F. Taddei, A. Malandrino, L. Cristofolini, and M. Viceconti, “Subject-specific finite element models can accurately predict strain levels in long bones,” *Journal of Biomechanics*, vol. 40, no. 13, pp. 2982–2989, Jan. 2007.

[125] S. McLachlin, H. Kreder, M. Ng, R. Jenkinson, C. Whyne, and J. Larouche, “Proximal Screw Configuration Alters Peak Plate Strain Without Changing Construct Stiffness in Comminuted Supracondylar Femur Fractures:,” *Journal of Orthopaedic Trauma*, vol. 31, no. 12, pp. e418–e424, Dec. 2017.

[126] G. S. Beaupré, N. J. Giori, W. E. Caler, and J. Csongradi, “A Comparison of Unicortical and Bicortical End Screw Attachment of Fracture Fixation Plates:,” *Journal of Orthopaedic Trauma*, vol. 6, no. 3, pp. 294–300, Sep. 1992.

[127] C. Sfeir, L. Ho, B. A. Doll, K. Azari, and J. O. Hollinger, “Fracture Repair,” in *Bone Regeneration and Repair*, J. R. Lieberman and G. E. Friedlaender, Eds. Totowa, NJ: Humana Press, 2005, pp. 21–44.

[128] H. Pelham, “Computational Modelling in the Development of Novel Passive Strain Sensors for Orthopedic Implants,” p. 97.

[129] S. J. Shefelbine *et al.*, “Prediction of fracture callus mechanical properties using micro-CT images and voxel-based finite element analysis,” *Bone*, vol. 36, no. 3, pp. 480–488, Mar. 2005.

[130] H. Pelham *et al.*, “Implantable strain sensor to monitor fracture healing with standard radiography,” *Scientific Reports*, vol. 7, no. 1, p. 1489, May 2017.

[131] S.-H. Kim, S.-H. Chang, and H.-J. Jung, “The finite element analysis of a fractured tibia applied by composite bone plates considering contact conditions and time-varying properties of curing tissues,” *Composite Structures*, vol. 92, no. 9, pp. 2109–2118, Aug. 2010.